# Bump Bonded Pixel Detectors on CVD Diamond from RD42

W. Adam[1], C. Bauer[2], E. Berdermann[3], P. Bergonzo[4], F. Bogani[5], E. Borchi[6], A. Brambilla[4], M. Bruzzi[6], C. Colledani[7], J. Conway[8], W. Dabrowski[9], P. Delpierre[10], A. Deneuville[11], W. Dulinski[7], B. van Eijk[12], A. Fallou[10], F. Fizzotti[13], F. Foulon[4], M. Friedl[1], K.K. Gan[14], E. Gheeraert[11], E. Grigoriev[9], G. Hallewell[10], R. Hall-Wilton[15], S. Han[14], F. Hartjes[12], J. Hrubec[1], D. Husson[7], H. Kagan[14], D. Kania[14], J. Kaplon[9], C. Karl[16], R. Kass[14], K.T. Knöpfle[2], M. Krammer[1], A. Logiudice[13], R. Lu[13], P.F. Manfredi[17], C. Manfredotti[13], R.D. Marshall[4], D. Meier[9], M. Mishina[18], F. LeNormand[7], A. Oh[16], L.S. Pan[14], V.G. Palmieri[19], H. Pernegger[1], M. Pernicka[1], A. Peitz[8], S. Pirollo[6], P. Polesello[13], K. Pretzl[19], V. Re[17], J.L. Riester[7], S. Roe[9], D. Roff[15], A. Rudge[9], S. Schnetzer[8], S. Sciortino[6], V. Speziali[17], H. Stelzer[3], J. Steuerer[16], R. Stone[8], R.J. Tapper[15], R. Tesarek[8], G.B. Thomson[8], M. Trawick[14], W. Trischuk[20], R. Turchetta[7], E. Vittone[13], A. Wagner[16], A.M. Walsh[8], R. Wedenig[9], P. Weilhammer[9], W. Zeuner[16], H. Ziock[21], M. Zoeller[14]

**The RD42 Collaboration**

E. Charles, A. Ciocio, K. Dao, K. Einsweiler, D. Fasching, A. Joshi, S. Kleinfelder, O. Milgrome, J. Richardson, P. Sinervo

**LBL/Wisconsin Pixel electronics team**

[1] *Institut für Hochenergiephysik der Österr. Akademie d. Wissenschaften, A-1050 Vienna, Austria*
[2] *MPI für Kernphysik, D-69029 Heidelberg, Germany*
[3] *GSI, Darmstadt, Germany*
[4] *LETI (CEA-Technologies Avancees) DEIN/SPE - CEA Saclay, 91191 Gif-Sur-Yvette, France*
[5] *LENS, Florence, Italy*
[6] *University of Florence, Florence, Italy*
[7] *LEPSI, CRN, Strasbourg 67037, France*
[8] *Rutgers University, Piscataway, NJ 08855, U.S.A.*
[9] *CERN, CH-1211, Geneva 23, Switzerland*
[10] *CPPM, Marseille 13288, France*
[11] *LEPES, Grenoble, France*
[12] *NIKHEF, Amsterdam, Netherlands*
[13] *University of Torino, Italy*
[14] *The Ohio State University, Columbus, OH 43210, U.S.A.*
[15] *Bristol University, Bristol BS8 1TL, U.K.*
[16] *DESY, Hamburg, Germany*
[17] *Universita di Pavia, Dipartimento di Eletronica, 27100 Pavia, Italy*
[18] *FNAL, Batavia, U.S.A.*
[19] *Lab. für Hochenergiephysik, 3012 Bern, Switzerland*
[20] *University of Toronto, Toronto, ON M5S 1A7, Canada*
[21] *Los Alamos National Laboratory, Research Division, Los Alamos, NM 87545, U.S.A.*

**Abstract**

Diamond is a nearly ideal material for detecting ionizing radiation. Its outstanding radiation hardness, fast charge collection and low leakage current allow it to be used in high radiation environments. These characteristics make diamond sensors particularly appealing for use in the next generation of pixel detectors planned for experiments at Fermilab and the LHC. Over the last year we have worked with several groups who have developed pixel readout electronics in order to optimise sensor preparation on diamond substrates for bump-bonding. We describe the four different approaches that are being actively pursued and the results of one fully bonded sensor tested in a beam. This device shows good hit efficiency as well as clear spatial correlations to tracks measured in the reference telescope. The position resolution observed is that expected given the detector pitch. Preparations for the next generation of CVD diamond pixel detectors will also be described.

# 1 Introduction

At present both the ATLAS and CMS detectors at the Large Hadron Collider (LHC) plan to install pixel devices as the innermost layers of their tracking detector. Pixel detectors facilitate pattern recognition and vertexing in locations where the track occupancy on strip detectors would be too high or the bulk damage too great. Substituting CVD diamond sensors for Silicon would solve the radiation damage problem [1] while preserving other features of solid-state tracking such as precision and stability. Each pixel cell will be readout by an individual charge amplifier followed by a fast shaper. The shaped signals will then be evaluated by sparsification logic and eventually delivered to the back end. The pixel detector readout chip must geometrically match the pixel pattern on the detector substrate since a single active cell on the detector substrate will be connected to its readout cell via a bump bond. Bump bonding is a difficult process on the 50 $\mu$m scale such as is required for both experiments. Though pixel readout electronics are still in the development phase, tests have been undertaken with existing designs in order to study the bump bonding process including preparation of the contact surface.

# 2 Sensor Prototypes

The first diamond pixel detector was tested in August 1996 in a particle beam at CERN. This detector was readout.via a pixel fanout structure metallized on a glass substrate. The purpose of this test was to investigate the feasibility of pixel geometries on a diamond substrate and the charge collection performance. This device had a mean signal-to-noise ratio of 27:1 and a position resolution consistent with digital resolution for a device with 150 $\times$ 150 $\mu m^2$ pitch. Based on the success of this test, we produced pixel sensors to the specifications of ATLAS and CMS. The contact geometry on the diamond surface has been fabricated to match the requirements of the existing readout chips for ATLAS and CMS. Table 1 gives an overview of diamond sensor samples with substrate size and pixel cell size. The metalisation contact and proposed bump bonding material are also listed.

| | pixel cell size [$\mu m^2$] | diamond substrate size [$\mu m^2$] | metallisation [elements] | passivation [yes/no] | bumb bonding metal |
|---|---|---|---|---|---|
| CMS/1 | 100 $\times$ 100 | 3725 $\times$ 4725 | Cr/Au | yes | In |
| ATLAS/1 | 50 $\times$ 414.4 | 3800 $\times$ 5800 | Cr/Ni/Au | yes | In |
| ATLAS/2 | 50 $\times$ 414.4 | 3800 $\times$ 5800 | Ti/W | no | Sn/Pb |
| ATLAS/3 | 50 $\times$ 536 | 4000 $\times$ 8000 | Ti/W | no | In |

Table 1: Overview on diamond pixel detectors for pixel chips in CMS and ATLAS, The dimensions of the sensors, their metallisation and passivation layers are listed.

The first bump bonding tests were performed in collaboration with the CMS group. Other devices were bump bonded with the ATLAS group and tested with a source for its charge collection and efficiency. Figure 1 and Figure 2 show the first diamond pixel sensors with a pixel metallization pattern for CMS and ATLAS. An ATLAS/3 pixel detector has been produced and successfully bonded to the pixel readout chip at Boeing. The choice of Ti/W for the readout pads was natural as Ti creates the best ohmic contact with the diamond surface, facilitating the extraction of the signal, while $W$ is an inert over-metal that is commonly used in integrated circuit processing.

Tungsten also resists oxidation a feature necessary as the diamond sensors were prepared in a different location than the final bump-bonding. Silicon sensors previously bonded by Boeing have exhibited less than $10^{-4}$ failed bonds. A visual inspection of the bump bonds on our diamond device showed a yield of 100%.

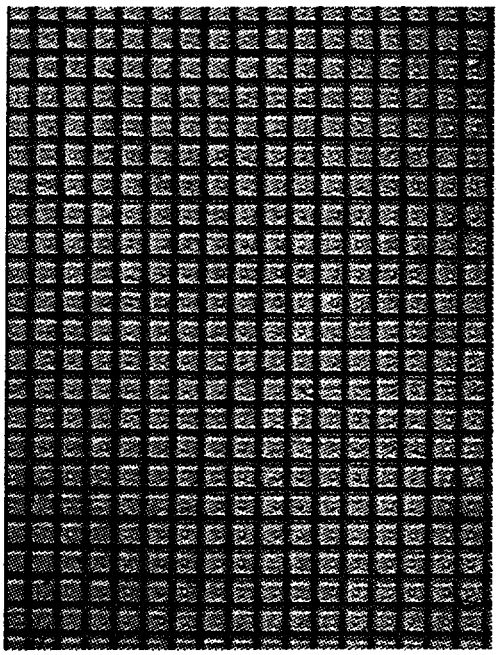

Figure 1: Top view of a CMS diamond pixel sensor showing the overall pixel pattern. The pixel metallization is Cr/Au for this device. The pixels are covered with a passivation layer. The passivation has a hole offset from the pixel center for the Indium bond.

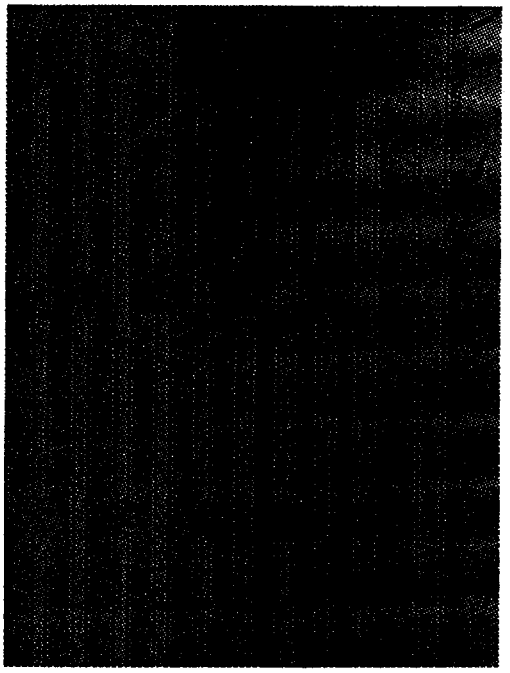

Figure 2: Corner view of the ATLAS/3 pixel sensor showing the overall pixel pattern. The metallization is Ti/W. The pixels are not covered with a passivation layer.

## 3 Source Test Results

The first test of the ATLAS/3 pixel tracker was performed using a $^{107}$Ru source at CERN in late 1997. The relatively low electron end point energy of 3.54 MeV meant that it was not possible to include a silicon reference plane between the pixel prototype and the trigger. Thus no external spatial information was available from this initial test. The source was mounted 5 cm from the surface of the pixel detector. A $7 \times 7$ mm$^2$ scintillator trigger counter was mounted 3 cm behind the pixel detector. In order to quantify the trigger acceptance and efficiency a silicon pixel detector (readout with the same readout chip) was tested in parallel. We took about 15,000 triggers in the silicon test run. We observed 5,100 hits in the silicon pixel detector which roughly corresponds to the 35% geometric acceptance expected from the active area of the pixel detector (17.3 mm$^2$) relative to the area of the trigger counter (49 mm$^2$).

The signal size of a diamond detector can be increased by about a factor of 1.6 by exposing the diamond to $< 1$ krad of ionizing radiation. In this first test, we decided not to pump up the

diamond pixel since the readout chip was not implemented in a radiation-hard technology and could have been damaged. Furthermore, since the readout chip might be damaged by over voltage, we did not operate the diamond pixel detector at full voltage. The net result was that the signal from the diamond was about a factor of two lower than had been observed in previous tests of this device. Also, during this test the threshold of the readout chip was about a factor of two higher than the minimum value. However a run of 39,000 triggers yielded hits in 75 % of the pixels. Given the reduced signal and high sparsification threshold only about 2 hits per pixel were seen. Thus Poisson fluctuations can account for the absence of hits in a further 15 % of the pixels. This result was sufficiently encouraging to re-mount the tracker in the testbeam described in the next section.

# 4 Testbeam Results

The ATLAS/3 pixel tracker was tested in a 50 GeV pion beam at CERN in April of 1998. The standard RD42 silicon reference telescope [2] was used to provide four $x$ and $y$ measurements of the track, each with 2 $\mu$m precision. The resulting track extrapolations onto the plane of the diamond were better than 2 $\mu$m in each dimension, significantly better than the resolution expected from our pixel tracker. We collected 200 k tracks at normal incidence to the diamond surface and have studied the pixel hit distribution, charge deposition and spatial correlations between the pixel tracker and the external reference telescope.

## 4.1 Bonding Efficiency

Figure 3a) shows the number of hits found per pixel during this test. The size of the boxes is proportional to the number of tracks above threshold in each pixel cell. Further study of the charge distribution in columns 4 and 6 indicates that many of these hits resulted from false triggers. We exclude these columns from further study. In addition there is an apparent reduction in the number of hits seen on the "right" half of the tracker when compared to the "left" half. This effect is still under study. It may indicate a variation in the readout threshold across the chip or a non-uniformity in the efficiency of the external (scintillator) trigger system.

The most striking feature of fig. 3a) is that charged particle hits have been recorded in almost all of the pixel cells. This is further evidence that a high bump-bonding yield has been achieved. Figure 3b) shows a projection of the number of hits seen in each pixel. In the top plot we see that there are 26 pixels that failed to record a single hit. In the lower plot we restrict our attention to the four columns on the "left" side of the tracker. There only 6 of the 256 pixels failed to record a hit. From the lower plot it is clear that there is very little chance that many of these six were a fluctuation, as there is only one additional pixel which saw only a single hit. From this data we conclude that at least 98% (250/256) of the channels were successfully bonded and capable of recording hits. A similar conclusion can be drawn from the top distribution. There a background subtraction, based on the number of cells with only a few hits recorded, of about 15 channels is estimated. This leaves 11 channels (26-15) that appear truly lacking hits leading us, again, to conclude that 98 % (501/512) of the channels are bonded.

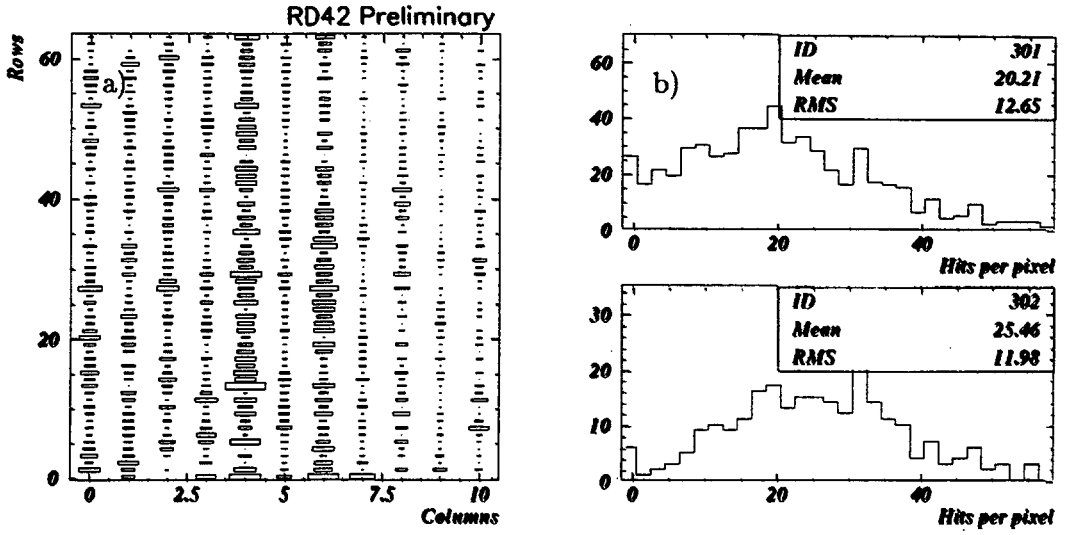


Figure 3:
a) The number of hits per pixel seen in April 1998 testbeam run. b) The distribution of number of hits per pixel cell. The top plot shows the distribution over the whole tracker (512 cells) while the bottom plot shows the number of hits per cell only on the "left" side of the detector where a significantly higher number of hits per cell have been recorded.

## 4.2 Charge Distribution

Of the 200 k testbeam tracks recorded the trigger acceptance calculation predicts 66 k of them should have passed through the diamond tracker. Excluding the two noisy columns we should have seen 49 k hits. Figure 4a) shows the time-over-threshold (charge) distribution for all the tracks recorded in this run. We see only 12 k hits. We attribute this 25% efficiency to a combination of reduced charge in the un-pumped diamond as well as a sparsification threshold of about 4000 electrons. In this testbeam we were able to operate the diamond sensor at full bias voltage (550 V for the 550 $\mu$m thick detector) but were still hesitant to expose the tracker to sufficient ionising radiation to fully pump the detector. While we were able to lower the threshold slightly, compared to the source test performed earlier, we still had a threshold that was almost a factor of two higher than optimal.

One of the features of using diamond as a sensor material is that it can be recycled. In this case, the diamond material that we are now using as a pixel tracker was previously tested as a strip tracker. As such we have data on the charge distribution we expect from the pixel detector. Figure 4b) summarises our understanding of the situation. The solid gray histogram is the single-strip charge observed in this diamond material when it was a strip tracker with 50 $\mu$m pitch. This charge corresponds to a 200 $\mu$m collection distance, consistent with that seen in source characterisations of this material. The single strip charge is all that is relevant to our pixel tracker

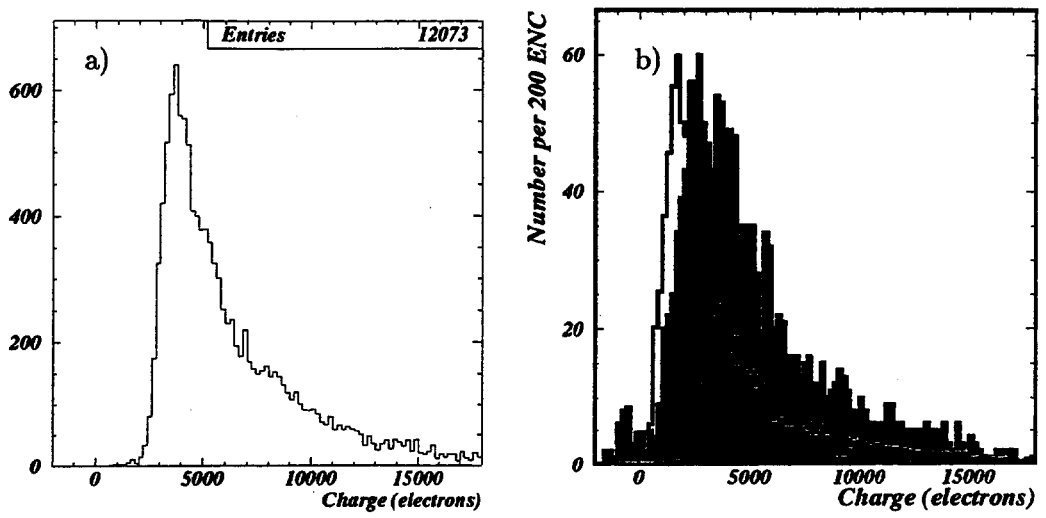


Figure 4:
a) Distribution of time over threshold (charge) measurements for triggered pixels in April 1998 testbeam. b) Comparison of the charge observed in the pixel tracker (dark grey) in the April 1998 testbeam with that seen in the same diamond when it was instrumented as a strip tracker in May 1997 (light gray histogram). The open histogram is a prediction, based on the observed (light gray) charge and the fact that the diamond was not pumped in the 1998 test, for the charge we should expect to see in the pixel tracker. From the turn-on of the charge seen in the pixel tracker (dark grey) we conclude that the pixel electronics was operating with a 4000 $e^-$ threshold.

as we expect, and see, no significant sharing of cluster charge between neighbouring pixels. This data was taken with the tracker fully pumped (exposed to about 10 kRad of ionising radiation). Extensive study of this effect lead us to conclude that trackers not prepared in this way produce 40 % less charge. Thus, the open histogram is the single strip data scaled down by 40 %. Overlaid (in black) is the actual charge observed in the pixel detector. We conclude that the high threshold (4000 e) with which we were operating explains the missing hits.

In future tests we plan to pump the detector up (returning to the charge distribution shown in gray in fig. 4b). If we can also lower the threshold to 2000 e then we would expect this pixel tracker to achieve an efficiency of 80 %. To move much beyond this will require a slightly lower threshold and/or higher quality diamond. We expect that in the next 12 months we will have both.

### 4.3 Spatial Resolution

The correlation between reference telescope track positions and the position of hits recorded in the pixel tracker is shown in figs. 5a) and 5b). Only 20 % of the total sample has been tracked at this stage. A clear correlation between the two measurements is seen. At very low "Pixel x position"

we see a degradation in the position resolution consistent with known defects in the patterning, near one edge of the diamond sensor.

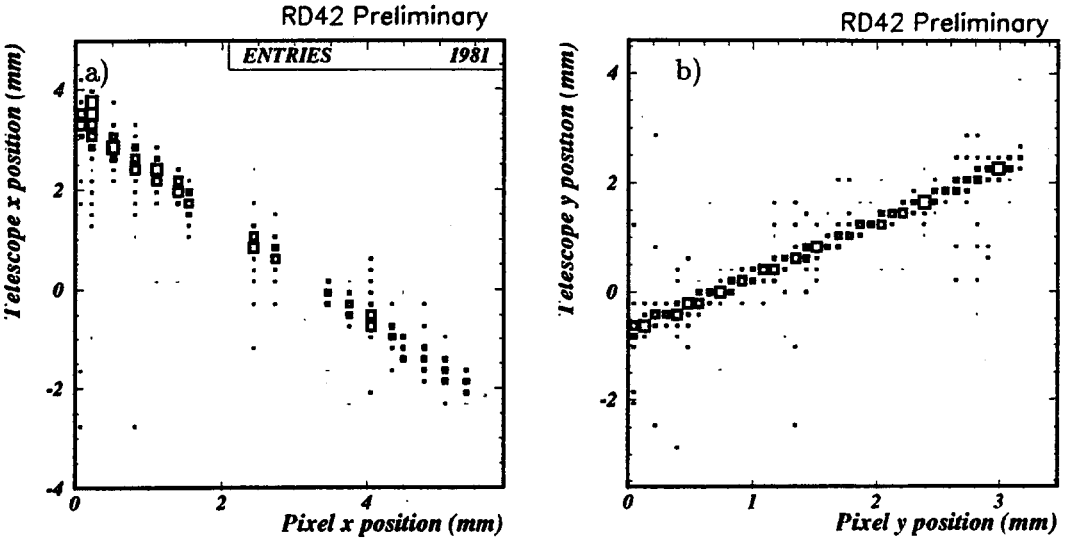


Figure 5:
The spatial correlation between the pixel detector hits and the reference telescope tracks in a) the $x$ (long pixel) view and b) the $y$ (short pixel) view.

Projections of these two plots along the diagonal yield the results shown in figs. 6a) and 6b). The resolution along the direction of the large pixel dimension (536 $\mu$m in length) is, as expected, a top-hat distribution with a full width at half maximum of about 500 $\mu$m. In the direction measured by the small pixel dimension we see a position resolution, 14.8 $\mu$m, consistent with the strip pitch divided by the square root of twelve. In both cases there are minimal tails beyond the main peak indicating that very few of the hits recorded by the pixel tracker are unrelated to the charged tracks measured in the telescope. The beam intensities recorded in our telescope are such that fewer than 1 % of the triggers contain more than one charged track thus the potential for confusion in the reconstruction of the reference telescope, while minimal, is not completely negligible. However, it should be clear that the vast majority (over 99 %) of the hits that trigger the pixel readout chip result from the passage of charged particles also reconstructed in the reference telescope.

## 5 Conclusions

The RD42 collaboration has undertaken an aggressive effort to produce working diamond pixel prototypes. This is a natural progression of the work that has been undertaken by the collaboration up to now. As diamond is a sufficiently radiation hard material to survive, for the lifetime of the LHC, at small radii, it is now natural that diamond be adapted to the readout geometries best suited to these detection regions.

Work with one prototype tracker system (the ATLAS/3) has yielded a fully functional proto-

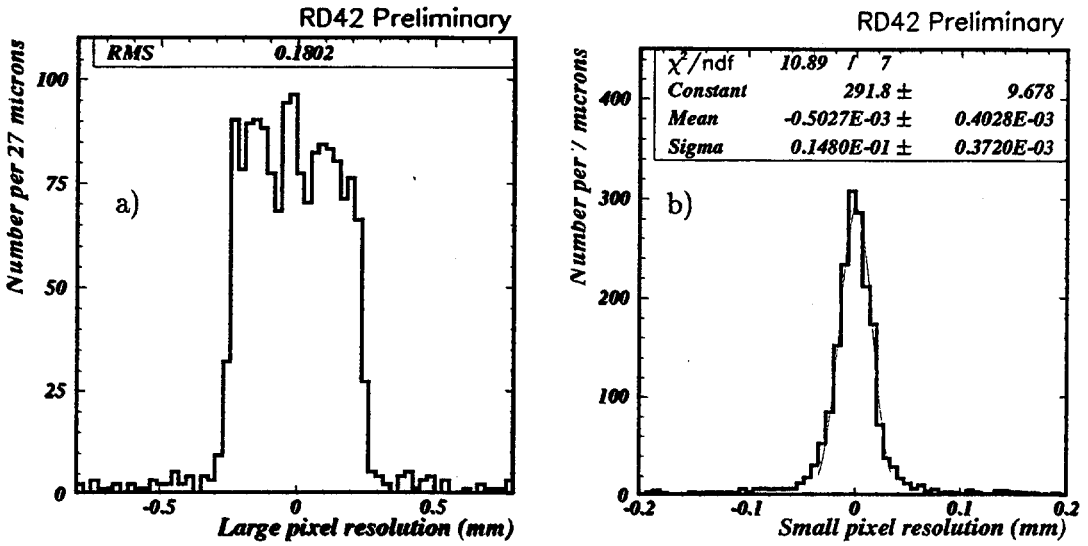


Figure 6:
The position resolution of the pixel detector prototype in a) the $x$ (long pixel) view and b) the $y$ (short pixel) view.

type that has proven high bump-bonding yields are possible. Testbeam studies of this diamond sample have served to further emphasize that the material currently available, though promising, is not entirely adequate to produce fully functional pixel detector systems. However, with modest improvements in detector material quality and the reduction of readout thresholds – similar to those that will be needed to readout thinned silicon sensors – the goal of producing a CVD diamond based pixel tracker system appears to be achievable in the near future.

## References

[1] W. Adam *et al.*, RD42 renewal (1997), LHCC-97/3.

[2] F. Borchelt *et al.*, Nucl. Instrum. and Meth. **A354**, (1991), 506.

# 3D--A New Solid-State Detector Architecture

Progress Report -- May 1998

Christopher Kenney and Sherwood Parker
U. of Hawaii

Julie Segal* and Christopher Storment
Stanford University

## A. Introduction

Until now, planar technology, in which all fabricated elements are on or within a few microns of the surface, has been the only technology used for the fabrication of integrated circuits as well as for silicon strip and pixel detectors [1].

The coming generation of high intensity machines such as the Large Hadron Collider (LHC) will place severe demands on both speed and radiation hardness of the inner tracking detectors. The speed of both strip and pixel detectors is adequate, but only marginally so, since typical pulse rise times of 5-10 ns are a significant fraction of the 25 ns beam crossing interval, and typical pulse lengths of 30-40 ns are longer.

There will, however, be nothing marginal about their response to radiation at the LHC [2] or HERA-B [3] at DESY. Without some change, they will not survive the damage to the bulk silicon. The radiation induced increase in the p-type dopant density and the corresponding increase in depletion voltage, will cause voltage breakdown long before the desired duration of the experiment.

While the Atlas and CMS groups are working on possible solutions to this problem, the only known one at this time consists of keeping the detector cooled to below 0° C before the radiation damage becomes too severe. This prevents the reverse annealing which causes a further large increase in effective dopant density. In addition, it will probably be necessary to use either thinner than normal, or partially depleted detectors. If cooling is lost for more than a few days per year, part or all of the silicon inner layers may be lost.

## B. 3D--A possible solution

3D is a proposed technology in which + and - electrodes penetrate from the surface through most or all of the detector bulk. The maximum drift and depletion distances are then set by the electrode spacings rather than the detector thickness. Both depletion voltages and collection times can then be kept small. Simulations of 3D detector designs indicate the initial depletion voltages will be in the range of 1-2 volts, and remain under 10 volts for the lifetime of the experiment. Peak fields, located where the depletion region borders the highly doped electrodes, are an order-of-magnitude below breakdown levels, and decrease under radiation as a larger

fraction of the voltage appears across the increasingly highly doped bulk.

The predicted behavior of such detectors are given in "3D--A proposed new architecture for solid-state radiation detectors" in [4]. Here we will only show a sample three-dimensional view (Fig. 1), typical electric fields before and after radiation (Fig. 2), depletion voltage comparisons between a 3D detector and a planar diode with simple 2D electrodes (which will deplete at lower voltages than normal strip detectors--Fig. 3), typical pulses expected on the electrodes of a 3D detector (Fig. 4), and a comparison with pulses on a strip detector (Fig. 5) [5].

C. The first attempts

During our initial tests, we learned of earlier attempts, in the period 1975 - 1982, to develop 3D electrodes for detectors and chip-to-chip connectors for computers [6] using thermomigration to fabricate aluminum doped p type columns in an n type silicon substrate.

In this process, a silicon wafer has a temperature gradient imposed, with the entire wafer maintained above the lowest melting point of an aluminum-silicon mixture. Aluminum, placed on the low temperature surface, diffuses into the silicon, reducing the melting point and forming a molten zone. Aluminum then diffuses from the cooler, high concentration region to the warmer, low concentration region, extending the molten zone there, and causing freezing at the cooler end which now has less aluminum. This process thus produces a column of dissolved aluminum in the silicon.

A paper by T. Anthony and H. Cline of General Electric [7] described an array of deep diodes formed by thermomigration. Among other applications, x-ray detection was mentioned. Fig. 6, reproduced from their paper shows square columns with a 0.5 mm pitch on the top and the distorted columns as they emerge on the bottom of a 3 mm thick silicon wafer. Since electrodes of only one type were mentioned and made, the field between them must have had a long vertical component to either face, and charge made in that region, a long collection distance. No mention was made of ever actually using the device as a detector, and no data were shown.

Another paper was published by G. Alcorn et al. of NASA in the 1982 International Electron Devices Meeting [8]. Their detector used a column in the center of a box-like cell. Both were formed from p-type aluminum doped silicon. Their electric fields would also have been primarily vertical, with the same long collection distances. During thermomigration their columns were sometimes deflected by crystal imperfections. The p box - n substrate - p column also formed a pnp transistor which led to high leakage currents. Actual use as a radiation detector was mentioned, but no data was shown.

A final paper, by T. Anthony [9], showed how diodes can be formed by diffusion from holes formed by laser drilling. Again, only one type of electrode was made, and no actual use as a radiation detector was mentioned.

A patent by Alcorn mentioned n doped columns from laser driven holes with the thermomigrated p-type boxes. No papers were ever published showing either fabricated devices or results from beam tests or experiments.

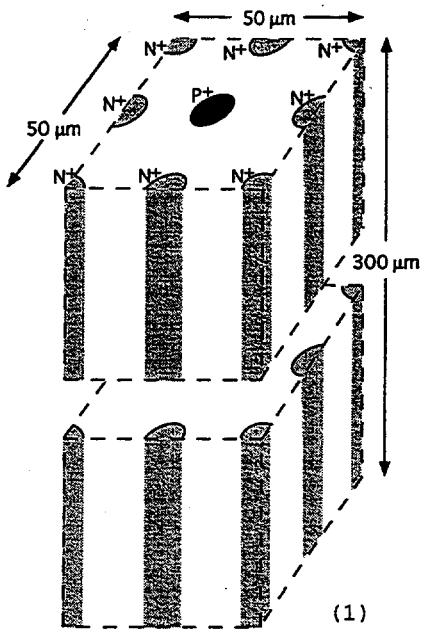


Fig. 1. Three-dimensional view of a typical cell.

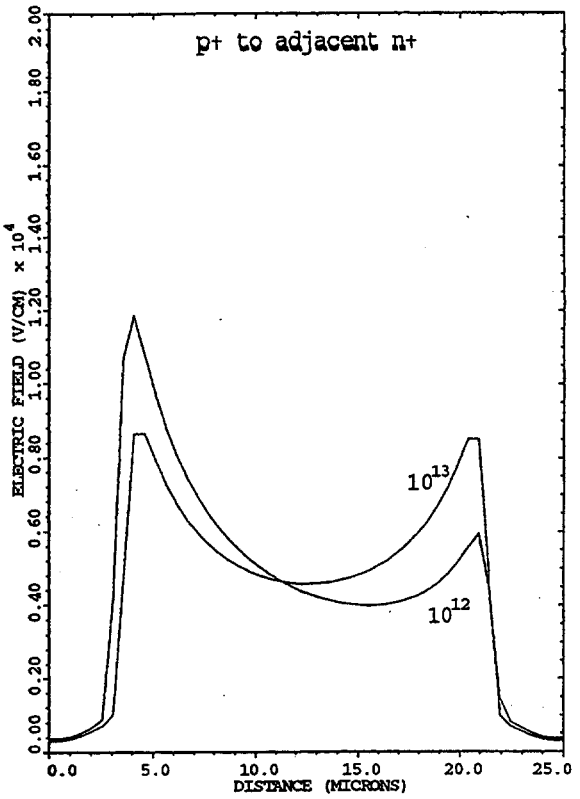


Fig. 2. Comparison of electric field magnitudes for the quarter cell of Fig. 1. 10 V applied voltage, along the line from the $p^+$- to the adjacent $n^+$-electrode for substrate dopings of $10^{12}$/cc and $10^{13}$/cc. With higher substrate dopant levels, as can occur with radiation damage, the peak fields, located where the depletion volume meets the electrodes, actually decrease due to the increase in voltage dropped across the lightly doped (compared to the electrodes) substrate. The small, but non-zero values of the electric fields at the ends of the plot (corresponding to the electrode centers) are due to approximations in the finite-element calculations.

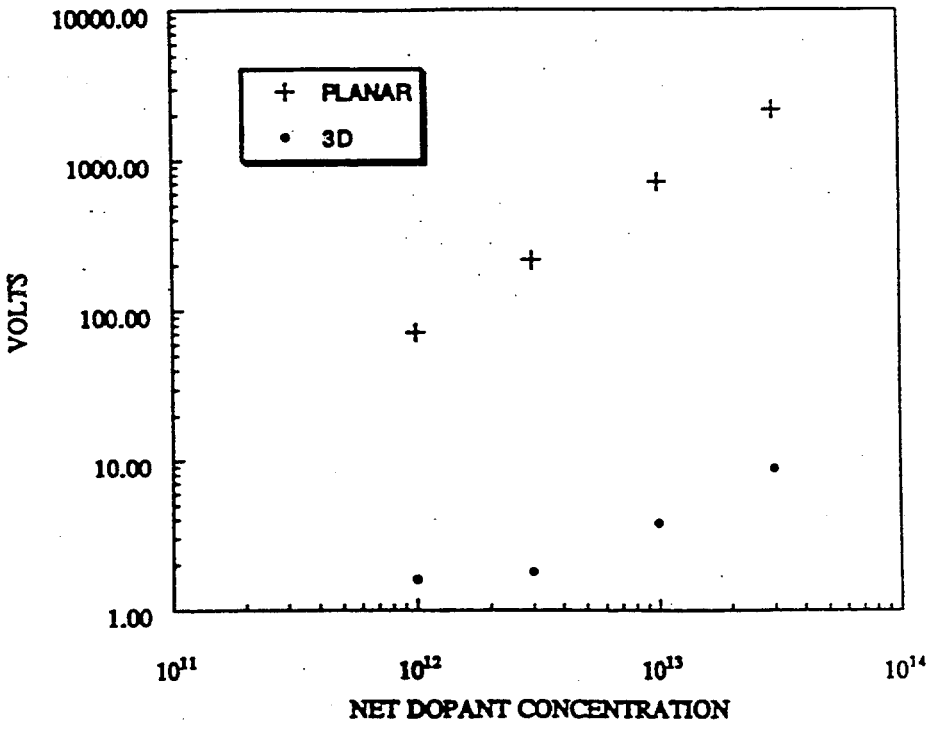


Fig. 3. Depletion voltage for a planar diode on 300 $\mu$m thick silicon, and a 3D detector with 50 $\mu$m pitch electrodes.

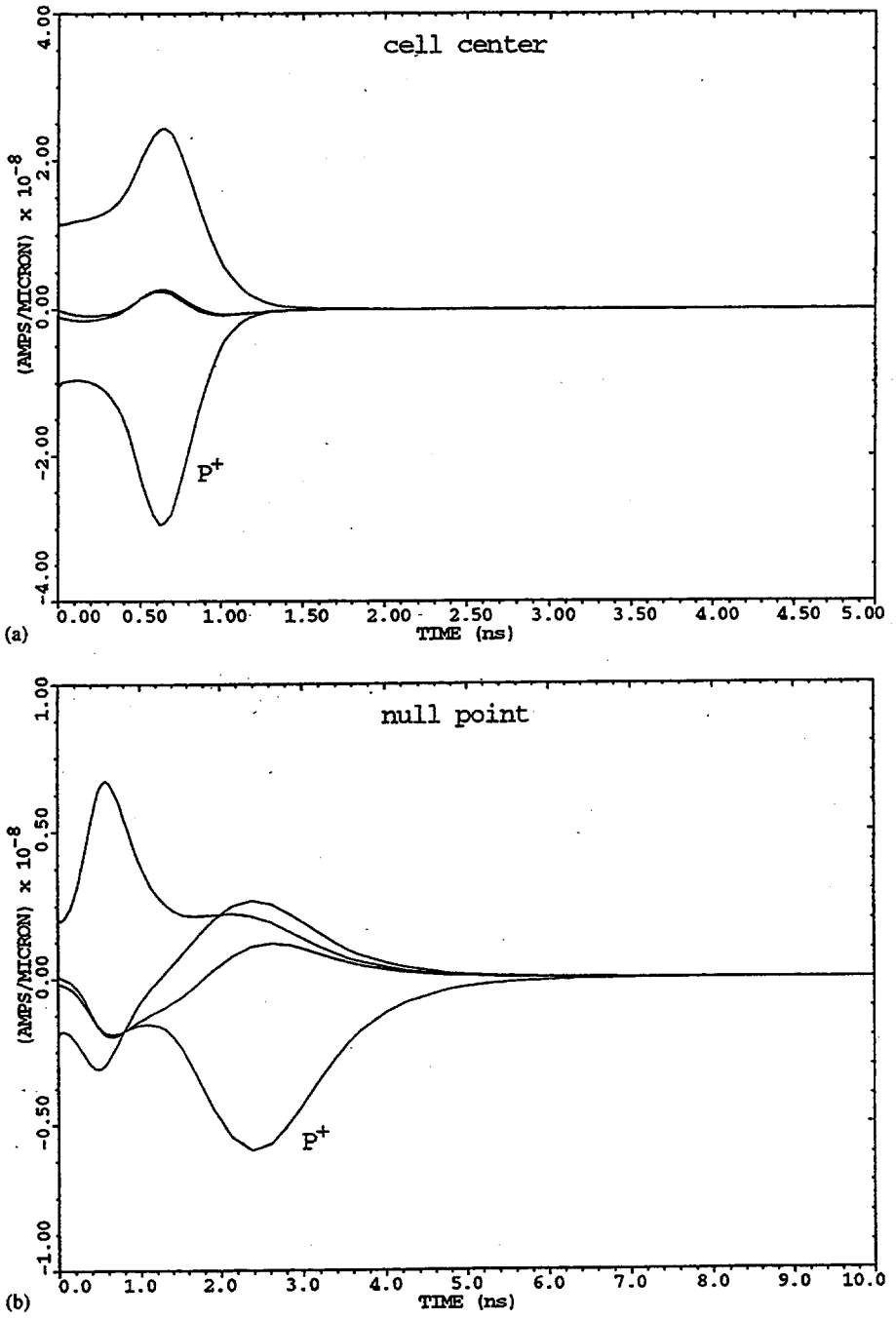


Fig. 4. Current pulses on the electrodes from a track parallel to the electrodes, (a) through the cell center, and (b) through the null point between two $n^+$ electrodes. The fields are those of Figure 2c, $10^{12}$ per cc, 10V. Effects of induced pulses from moving charges and diffusion are included, but not Landau fluctuations.

Nuclear Instruments and Methods in Physics Research A310 (1991) 189–191
North-Holland

# Electrostatic simulations for the design of silicon strip detectors and front-end electronics

R. Sonnenblick, N. Cartiglia, B. Hubbard, J. Leslie, H.F.-W. Sadrozinski and T. Schalk
*Santa Cruz Institute for Particle Physics, University of California, Santa Cruz, CA 95064, USA*




Fig. 3. Pulse shape at the junction side from a minimum ionizing particle. The three curves are the simulated current (with initial diffusion), the simulated current convoluted with the preamplifier response, and a typical observed pulse, respectively.

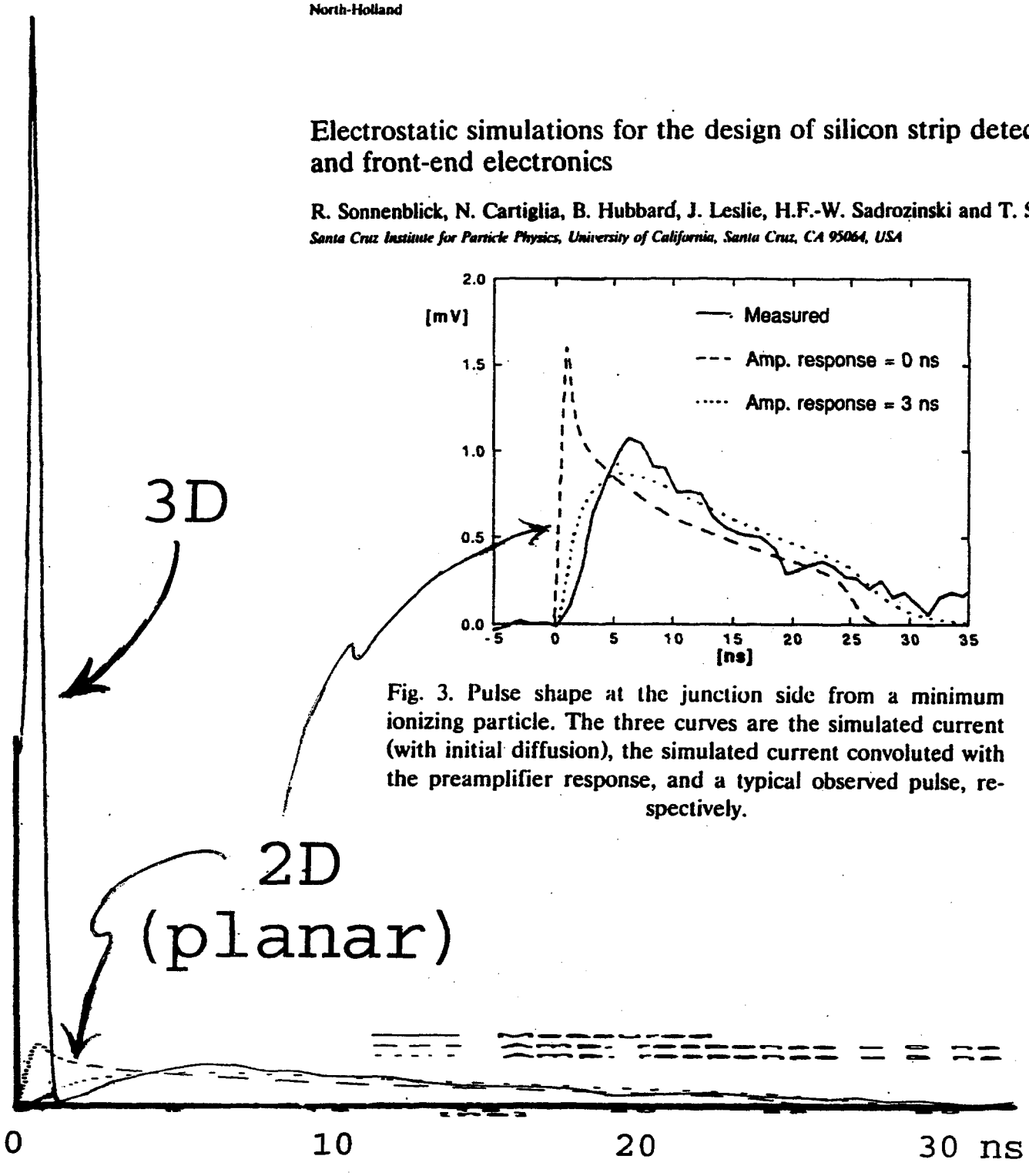


Fig. 5. Calculated pulses on a 3D $p^+$ electrode (from Fig. 4a) and on a standard 2D, planar electrode strip detector normalized to the same total area. The 2D arrows point to the 0 ns amplifier response curve, which has been xeroxed with the horizontal scale magnified to give the same time axis, and the vertical scale reduced so the area is the same as that of the 3D curve.

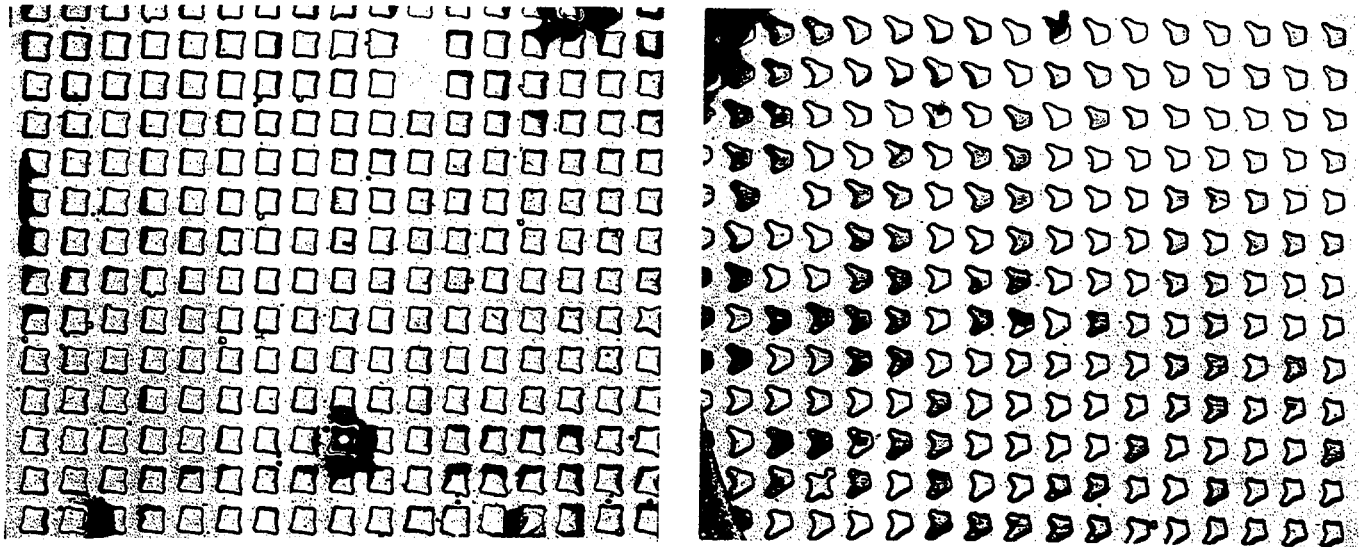


FIG. 6. Cross sections of the $p$-type array in the $n$-type silicon cooler. (a) The cooler side of the wafer where the droplets were introduced (15×); (b) the hot side of the wafer where the droplets exited after thermomigration (15×). A slight off-axis thermal gradient used to preserve the registry of the array (Ref. 62) has modified the shape of the droplet trails.



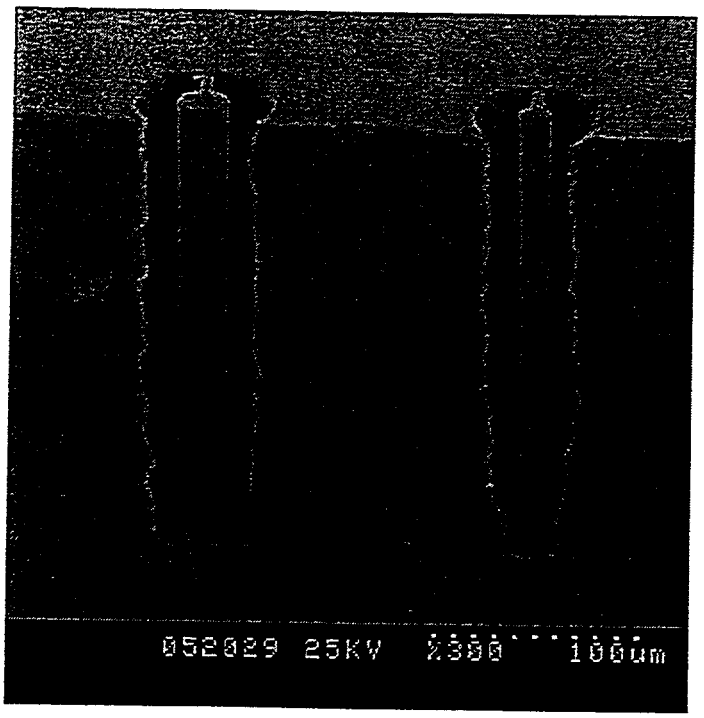


Fig. 7. Scanning electron microscope view of etched, poly-coated, 290 micron-high test structures. The scale at the lower right only applies to horizontal dimensions. Vertical ones are compressed by a factor of about 0.7.

D. The key fabrication tool

In the silicon industry, other than the now standard use of vertically oriented storage capacitors in RAM memories, only tentative steps have been taken since then in the development of 3D structures for integrated circuits [10]. However, intensive development work is underway in the use of VLSI techniques for the fabrication of 3D micro-mechanical structures. Many of these will be not only mechanical parts, but also sensors and actuators, and may also include integrated electronics [11].

Key to much of this work is a plasma etcher made by Surface Technology Systems (STS) [12] that can make vertical cuts at the high rate (for the VLSI world) of over 1 micron/minute. It uses an inductive coil to create the plasma, and a 13.56 MHz phase locked bias voltage to accelerate the ions toward the wafer. A fluorine based chemistry is used for etching. The operating conditions are cycled so etching alternates with the deposition of a protective coating on the sidewalls. STS has installed a machine at the Integrated Circuits Lab at Stanford University.

The method we plan to use to make 3D electrodes, is to etch holes, fill them with doped polysilicon, and diffuse the dopant out into the surrounding single-crystal silicon where the diode junctions will be formed. In an alternate method, the silicon surfaces would be doped first, then followed by poly filling.

E. Initial tests--etching the holes

Since the STS etcher was new, the first task was to characterize it. To do this--to measure its capabilities and determine the proper settings--we first etched arrays of holes and trenches of varying sizes. Optical microscopes with through-the-lens light systems have convergence angles that are far too large to illuminate most of the sides, let alone the bottom of the holes, and a depth of field that is far too small. Scanning electron microscopes have an adequate depth of field, but still have illumination and angle-of-view problems.

Sawing through the etched wafer (and some of the holes) provided the needed side views. Chipping along the hole edges produced several-micron irregularities which did not seriously degrade the diameter measurements. They did, however, leave some uncertainties in our knowledge of the smoothness of the hole walls. The test structures shown in Fig. 7, where cylindrical pillars are centered in 290 micron deep holes and connected to the wall by thin webs, solved that problem, since some saw cuts completely missed the pillars, which can be seen to have smooth, vertical side walls. After etching, but before sawing, the structures shown were coated with a 2 micron thick layer of poly.

Fig. 8 (top) shows the top, and Fig 8 (middle) the bottom, of the right column of Fig. 7. Both have radii of 7.9 microns. The lip at the top protrudes an additional 0.44 microns, while the radius halfway down (not shown) is 1.2 microns less, due, we believe, to thinning of the underlying silicon. Fig. 8 (bottom) shows the bottom of a similar column without the poly. The

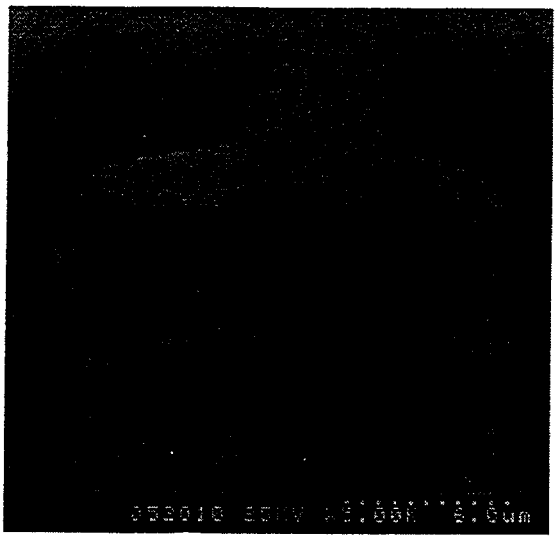

Fig. 8a

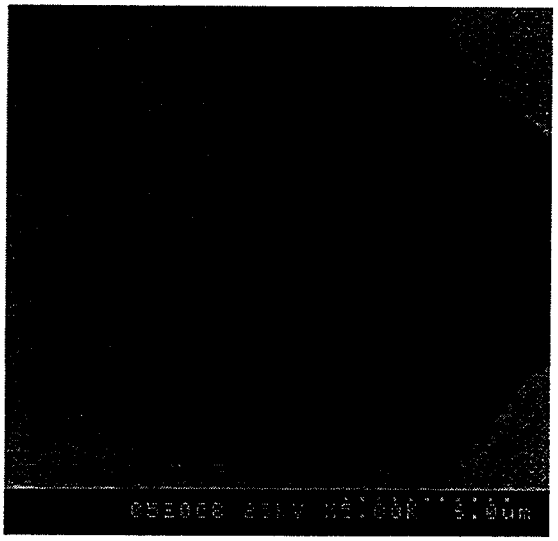

Fig. 8b

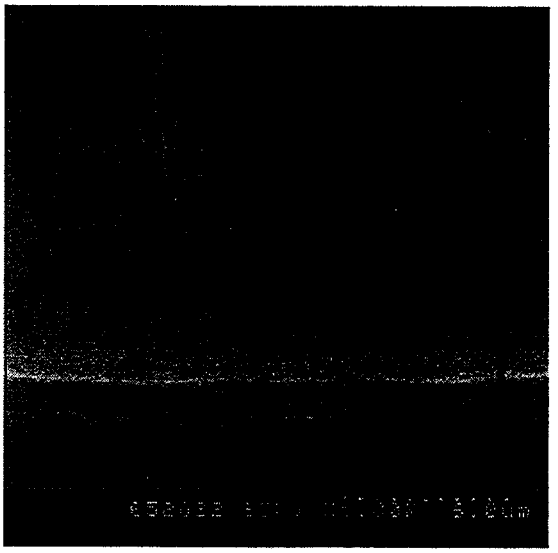

Fig. 8c

Fig. 8. High-magnification views of the (a) top, (b) bottom of the same column, and (c) of a similar column without the poly coating.

poly not only makes a highly conformal coating, but also a smoother one.

Fig. 9 shows saw cuts through typical holes. Fig. 10a, using data from those and many similar views, shows the depth reached as a function of etch time for four as-drawn (lithographic) diameters. Larger diameter holes etch more rapidly, as is particularly evident from Figs. 9a and 9c, since the reaction products must diffuse out of the holes. There is also an increase in diameter, shown in Fig. 10b, due to imperfect sidewall protection. This is the main reason the current depth-to-diameter ratio is limited to 11.5, as shown in Fig. 10c.

F. Initial tests--filling the holes

The holes are filled with poly to keep photoresist, which must be removed before high temperature steps, from being trapped there. That part of the fill for which the diffusion time out is shorter than the minority carrier lifetime, can also be sensitive to ionizing radiation. There are several ways to dope and fill the holes:

(a) They could be doped first and then filled using low-pressure chemical vapor deposition (LPCVD). Gaseous doping methods available at Stanford all form an oxide layer on the exposed silicon surface which could block charge collection from the electrodes. In addition, the poly deposition rate is reduced by the presence of mobile phosphorus atoms on the surface.

(b) They could be partially filled with poly, doped, filled with more poly, and annealed to drive in the dopant. Although there is evidence in the literature that dopants diffuse rapidly through polysilicon, the rate depends on the exact conditions of the poly deposition. With no oxide layer, signal charge could be collected from some or all of the poly electrode.

A series of test wafers was fabricated and sent to Solecon Laboratory for surface resistivity profile (SRP) analysis [13]. The SRP analyses, shown in Fig. 11a and 11b, demonstrate that LPCVD poly growth is not affected by the presence of an underlying glass, heavily doped with either boron or phosphorus. Rapid diffusion of both boron and phosphorus through poly and into the single-crystal bulk using our operating conditions has been confirmed by the SRP results shown in Fig. 11c and 11d.

G. The first fabrication run -- structures

The mask set being used in our first 3D fabrication run contains designs for 34 variations of 3D detectors and 6 sets of test structures. They include:

1. strip and pixel detectors with varying pitch, electrode diameter, guard-ring arrangement, and electrode pattern. Some pixel detectors have individual cells read out via wire-bond pads.

2. ATLAS pixels with bump-bond pads that fit the standard ATLAS cell dimensions, with 2 or 3 n-type electrodes per cell with spacings of 100 or 67 microns and the same number of p-type electrodes with the same pitch. These geometries should reduce the voltage required to fully

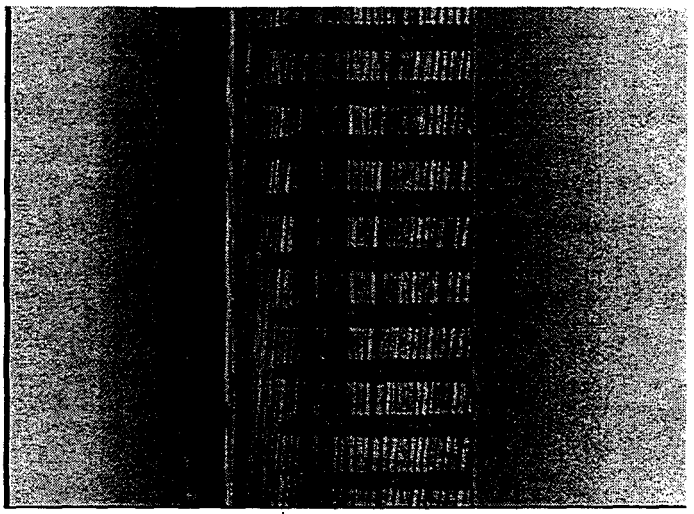

Fig. 9a

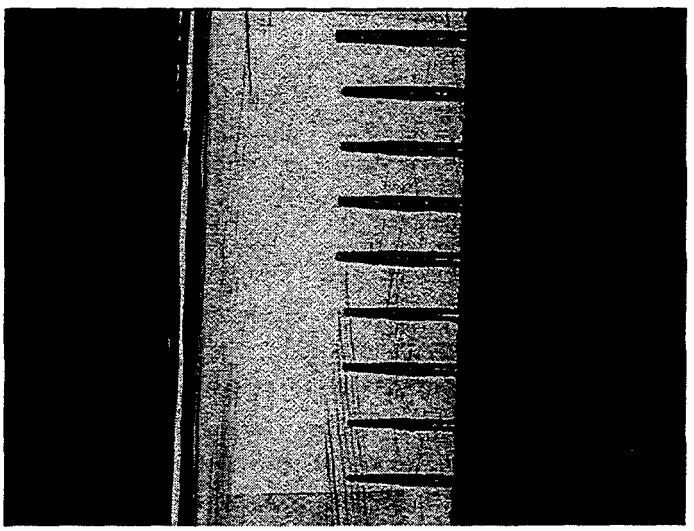

Fig. 9b

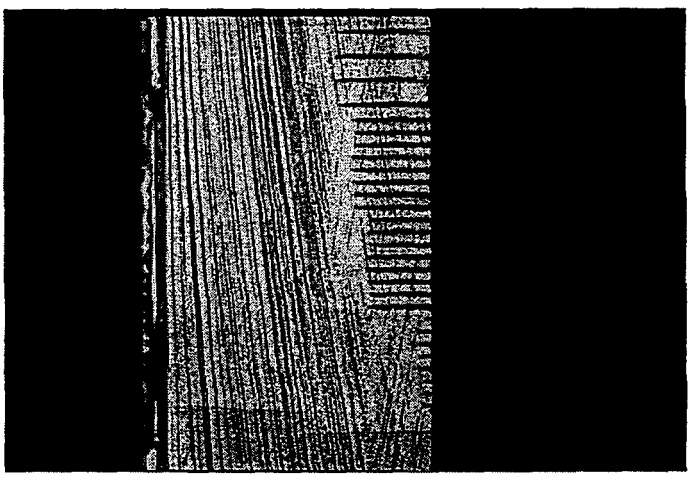

Fig. 9c

Fig. 9. A view of part of a set of etched holes, showing the increased depth reached by holes of larger diameters. The wafer was 540 microns thick and the etch time was 5 hours. The photo-mask hole diameters in Fig. 9a, from top to bottom are: 4 holes @ 30 microns, 4 @ 25 microns, and 1 @ 20 microns.

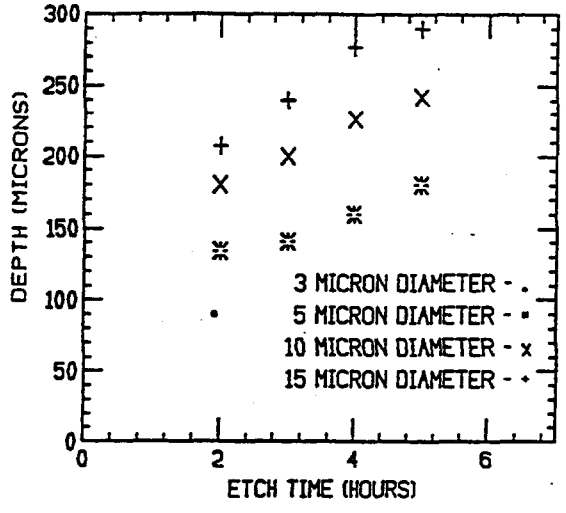


Fig. 10a

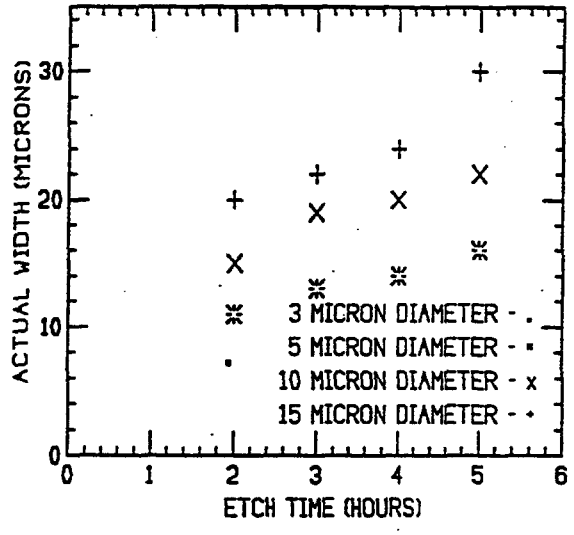


Fig. 10b

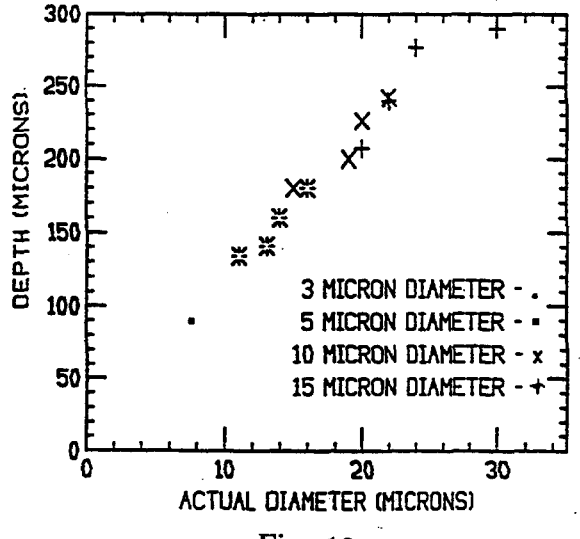


Fig. 10c

Fig. 10. Plots of (a) hole depths as a function of etching time, (b) actual hole diameters as a function of etching time, and (c) depth as a function of actual diameter for various hole diameters on the lithographic mask.

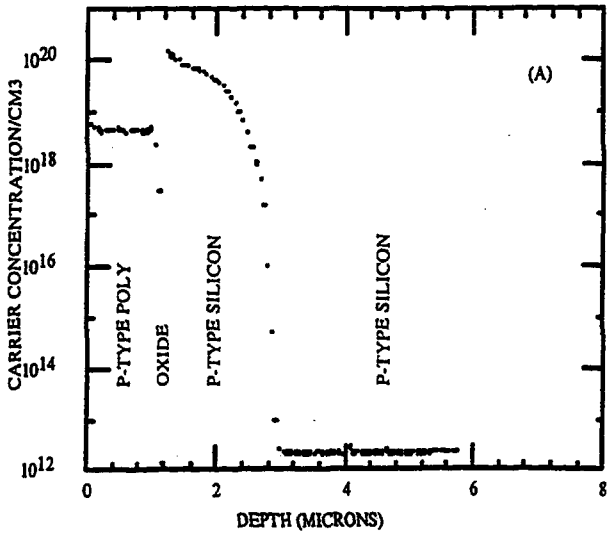


Fig. 11a

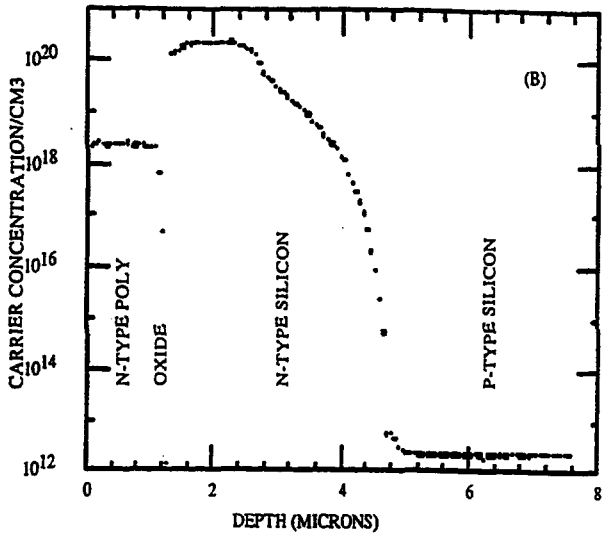


Fig. 11b

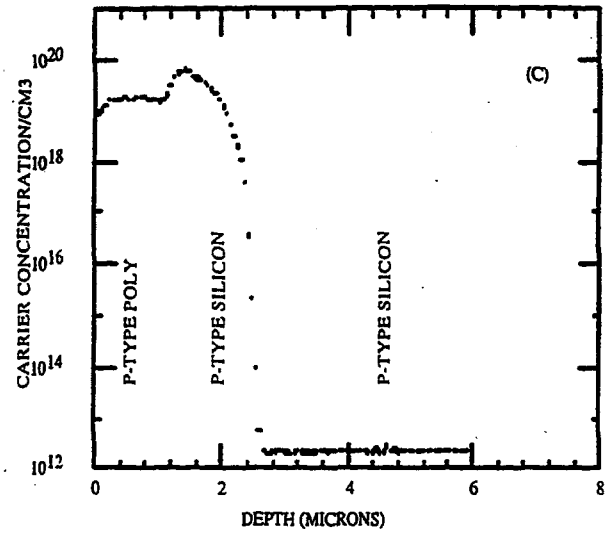


Fig. 11c

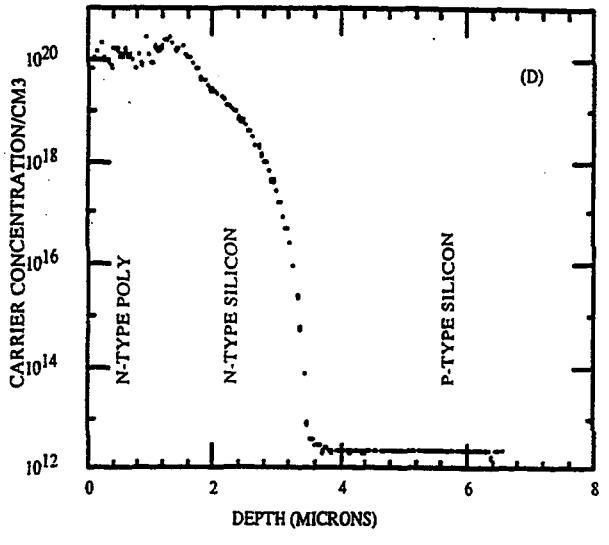


Fig. 11d

Fig. 11. Surface resistivity profiles showing the net dopant concentration versus depth for high-resistivity wafers which have: (a) boron doping, then 1.2 microns of poly deposited, (b) phosphorus doping, then 1.2 microns of poly deposited, (c) 1.2 microns of poly deposited, then doping with boron, (d) 1.2 microns of poly deposited, then doping with phosphorus. As a final step all wafers were given a thin capping oxide and annealed for 3 hours at 1000° C.

deplete the detectors after bulk radiation damage by factors of about 8 and 15.

3. centimeter-long strip detectors using the same geometry as an ATLAS sensor, but with the individual 3D pixel cells tied together to form strips which can be read out via standard silicon strip readout electronics.

4. a small pixel array, using the ATLAS sensor geometry, which has each cell connected to a bonding pad, allowing the detector to be tested using aluminum-wire bonding to standard front-end electronics.

5. detectors in which the drift time within a cell is measured.

6. sets of parallel trenches and concentric cylinders to measure capacitance and current versus voltage, providing information on the leakage currents, depletion voltages, device capacitances, and the effects of radiation damage.

7. detectors with all electrodes of each polarity tied together, providing similar information for specific detector types.

8. structures to determine the conductivity of the electrodes, the resistivity of the aluminum and diffusion layers and of the contacts between them.

H. Initial fabrication run -- process steps

An overview of the steps for the first group of wafers in fabrication was given in [4]. Fig. 12a shows a wafer, held up to a ceiling light, after the first set of deep holes had been etched. The different levels of brightness correspond to the density of holes. Fig. 12b shows a magnified view of a single structure.

The smaller than expected depth-to-diameter ratio found in the initial etching meant a thicker layer of poly fill was required, and a defect in the deposition tube flowmeter resulted in a 17 (rather than 12) micron thick layer. This poly also covers the entire wafer prior to its removal in step 4, and caused a number of wafers in the original batch to break, particularly in the transition from a 120° C to a 20° C solution, which does not normally cause breakage in uncoated wafers. A magnified view of such a broken surface in Fig. 13 shows the poly filling the hole.

While processing on this run continues, a second batch has also been started using the steps given in Table 1. In this run, the holes will be only partially filled, using a thinner layer of poly, and the second, n-doped set of holes will be etched from the other side of the wafer.

Ultimately, we expect that current work on improvements in the etching parameters and the planned use of thinner wafers will result in smaller diameter holes that can be etched and filled from the same side. There are also milling machines using a directed beam of ions which should etch holes with higher aspect ratios, but the Integrated Circuits Lab does not now have one.

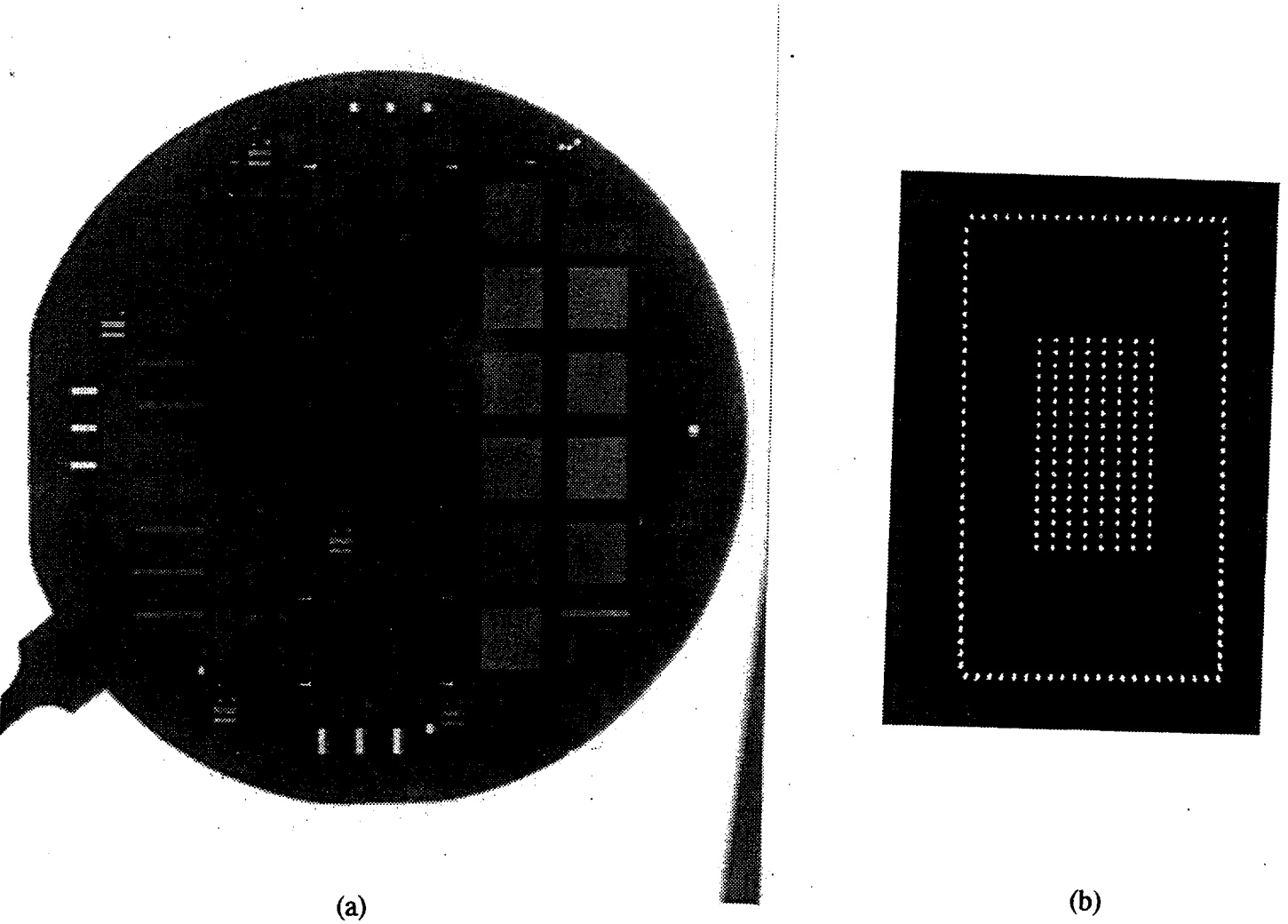

(a) (b)

Fig. 12. Photographs showing light passing through a wafer with the p-electrodes etched completely through: (a) a whole wafer and (b) part of a single structure. (The shadow at lower left is the tweezers holding the wafer; at lower right the edge of the ceiling light fixture.)

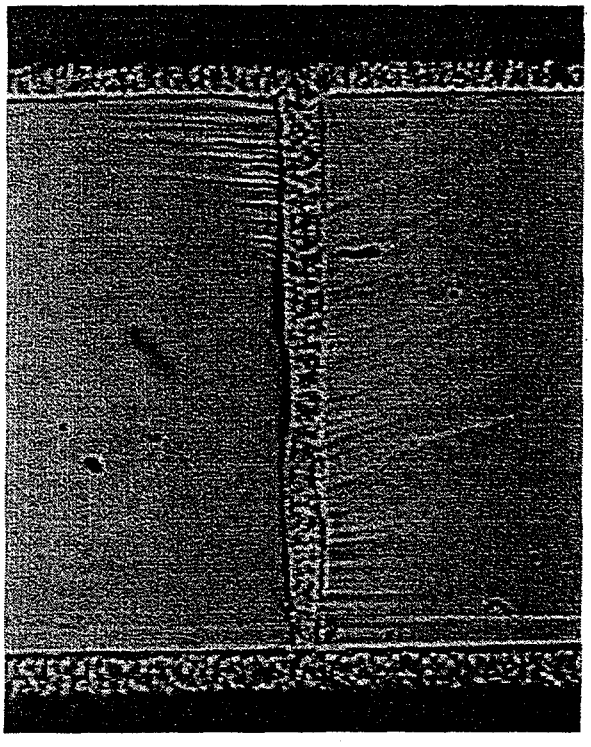

Fig. 13. Cross section of an electrode which has had 0.6 microns of poly deposited on its inner surface, had this surface heavily doped with boron, and then had the remaining hole filled with poly via LPCVD. The poly coat is visible on both the top and bottom surfaces as well as throughout the electrode. Some of the variation in the 23-micron-diameter electrode's profile is caused by the breakage plane not being parallel to the electrode's vertical axis.

**Table 1:**

| STEP | MASK | PURPOSE | PARAMETERS |
|---|---|---|---|
| 1 | MASK1 | MARKS TO ALIGN WAFERS WITH MASKS 2 THROUGH 6 | 1.2 MICRON THICK RESIST |
| 2 | | ETCH ALIGNMENT MARKS | SILICON PLASMA ETCH, $SF_6$ / $C_2ClF_5$ |
| 3 | | INITIAL CLEANING OXIDE | GROW 0.4 MICRON WET OXIDE |
| 4 | | ETCH TO REMOVE OXIDE | USE BUFFERED HYDROFLOURIC ACID |
| 5 | | FIELD OXIDATION TO PROTECT AND PASSIVATE SILICON AND AS ETCH STOP | GROW 1.0 MICRONS OF OXIDE IN STEAM AT 1000 C FOR 5 HOURS |
| 6 | MASK2 | N CONTACTS | PLASMA ETCH THROUGH OXIDE |
| 7 | MASK3 | N-ELECTRODES | 7.0 MICRON THICK RESIST |
| 8 | | DEEP ETCH | HIGH-ASPECT-RATIO ETCH USING STS |
| 9 | | DEPOSIT POLY GETTER LAYER | $SiH_4$ SOURCE AT 620 C, 0.46 Torr (2000A) |
| 10 | | PHOSPHORUS DOPING | $POCl_3$ SOURCE, 30 MINUTES AT 950 C |
| 11 | | DRIVE IN PHOSPORUS | 30 MINUTES AT 1000 C |
| 12 | | REMOVE POLYSILICON FROM TOP AND BOTTOM SURFACES | PLASMA ETCH |
| 13 | | CAPPING/MASKING OXIDE | GROW 0.2 MICRON WET OXIDE |
| 14 | MASK4 | P-ELECTRODES | 7.0 MICRON THICK RESIST (BACKSIDE) |
| 15 | | DEEP ETCH (BACKSIDE) | HIGH-ASPECT-RATIO ETCH USING STS |
| 16 | | DEPOSIT POLY GETTER LAYER | $SiH_4$ SOURCE AT 620 C, 0.46 Torr |
| 17 | | BORON DOPING | $BBr_3$ SOURCE, 30 MINUTES AT 955 C |
| 18 | | DRIVE IN BORON AND PHOSPORUS | 30 MINUTES AT 1000 C |
| 19 | | REMOVE POLYSILICON FROM TOP SURFACE | PLASMA ETCH |
| 20 | MASK5 | P CONTACTS | 7 MICRON RESIST, LONG LOW TEMPERATURE BAKE TO SPAN HOLES, FOLLOWED BY PLASMA ETCH OF OXIDE |
| 21 | | IMPLANT TO CONNECT P-ELECTRODE TO METAL | BORON, 20 KeV, 2E15/cm2 |
| 22 | | ETCH TO UNCOVER N CONTACTS | USE BUFFERED HYDROFLOURIC ACID TO REMOIVE STEP 13 OXIDE |
| 23 | MASK6 | METAL DEPOSITION | DEPOSIT AND ETCH ALUMINUM |

Table 1: Outline of 3D process steps.

We conclude with a few comments on some other possible applications of 3D technology.

I. Signal-to-noise ratio

The fast intrinsic pulse times, $\tau_{det}$, can, with the proper circuitry, produce high signal-to-noise ratios, as the signal current is proportional to the detector speed. To make use of this increased current, the frequency response of the filtering must be extended. This increases the noise also, but only as the square root of the frequency spread. For example, the number of traversals per second, n, of a Gaussian noise current $I_n$ with a positive slope past a threshold level $I_t$ is given by [14]:

$$n = \left[ \frac{\int_0^\infty \nu^2 \, p(\nu) \, d\nu}{\int_0^\infty p(\nu) \, d\nu} \right]^{1/2} \exp\left(- I_t^2 / 2 < I_n^2 > \right)$$

For a filter, $p(\nu)$, that is flat from $\nu_l$ to $\nu_h$, and with (typically) $\nu_h >> \nu_l$, we have:

$$n = \left[ (\nu_h^3 - \nu_l^3) / 3(\nu_h - \nu_l) \right]^{1/2} \exp\left(- I_t^2 / 2 < I_n^2 > \right) \approx ( \nu_h / \sqrt{3}) \exp\left(- I_t^2 / 2 < I_n^2 > \right)$$

$I_t$ can be set equal to a fraction $a_1$ of $< I_{det} >$.

$$I_t^2 = a_1^2 < I_{det} >^2 = a_1^2 < q/\tau_{det} >^2 = a_2 \, \nu_{det}^2$$

Here q is the total charge and the $a_i$ are constants that are independent, to first order, of $\nu$. White noise currents in electronics capable of matching detector speeds will have $\nu_h \approx \nu_{det}$ and

$$< I_n^2 > = a_3 \, \Delta\nu = a_3 (\nu_h - \nu_l) \approx a_3 \, \nu_h \approx a_4 \, \nu_{det}$$ (For a resistor, $a_3$ would equal 4KT/R.)

The threshold level squared can be increased in proportion to the detector speed squared, giving a near-exponential drop in noise counts that is proportional to the detector speed.

$$n = ( \nu_{det} / \sqrt{3}) \exp\left(- a_2 \, \nu_{det}^2 / 2 \, a_4 \, \nu_{det}\right) = ( \nu_{det} / \sqrt{3}) \exp\left(- a_5 \, \nu_{det}\right)$$

A simple integrator, of course, will not benefit from this speed. The circuit must respond only to rapid changes in voltage on an integrating capacitor, or to high instantaneous currents in a resistive circuit.

J. Other materials

There are a number of other materials where the short collection distances and potential speed of 3D technology may prove useful. Two examples are GaAs and diamond detectors.

The HERA report quoted in the introduction, after discussing radiation damage problems, goes on to say: "Recognizing the potential of diamond detectors, members of the VDS groups have joined the R&D efforts of the RD42 diamond tracker group."[3] Diamond detectors produce

about half as many electron-hole pairs per radiation length as silicon. They have continued to improve through the years, with a 1/e collection efficiency distance that started from zero in 1991, and now is somewhat larger than 200 microns [15].

Given the smaller amount of generated charge, high collection efficiency for all of the 250-300 micron thickness would be desirable -- that is a mean travel distance before capture of perhaps 700 microns using planar technology. 3D technology (using oxygen as well as $SF_6$ for etching) would already provide high collection efficiency with existing material. Given the very high mobility of electrons in diamond, it would also provide sub-nanosecond pulse rise times.

K. Active Edge Technology

Both pixel and silicon strip detectors made with planar technology must design in dead regions around the edges to allow for edge chipping made during the saw cuts. Also, the electrodes must be kept still further from the edges, so the bulging-out of the depletion region edges stays away from the saw cuts, since the latter are conductive due to their dangling bonds. In addition, the extensive array of guard rings needed to drop the voltage between top and bottom electrodes in a controlled fashion takes space, often more than the depletion region bulge below them. When bulk radiation damage requires high operating voltages, this array uses a significant amount of room.

For example, the current Atlas pixel detector units will loose 15% to 20% of their surface area to these causes [16]. Some proposed imaging systems use silicon strip detectors edge-on to form x-ray images in, for example, mammography [17]. Even in optimized designs ten to twenty percent of photons in the typical mammography spectrum are absorbed in this dead layer.

Cutting out individual detectors with the plasma etcher will eliminate the chip problem for any type of detector. 3D detectors operate at low voltages, and have the same voltage at corresponding points on top and bottom surfaces. Even if guard rings are needed on the surfaces around each electrode, they will not need much area, and the electrodes continuing below the surface will make the silicon volume below them sensitive. This may allow the fabrication of detectors that are fully active right to their edges.

Two types of edges will be studied: doped edges with a coat of doped poly, which can then be held at a definite voltage, and oxide-passivated ones in which the edge potential is set by a combination of fixed charges and by leakage currents.

L. Application of 3D technology to pixel detectors

While monolithic pixel detectors [18] have many advantages, they also have a number of disadvantages:

(a). only pmos electronics could be put in the pixel; nmos had to be along the edges,

(b). they are slow; with collection times in the 100 ns region being common along inter-pixel boundaries,

(c). radiation-hard technology, while compatible with pixel fabrication, has not actually been developed for it, and

(d). they employ new technology and so can not be assembled from commercial parts.

Combining 3D and monolithic pixel process steps will permit designs that will eliminate the first two disadvantages and in addition, provide the radiation hard bulk characteristic of 3D devices. The circuit would still have to be hardened, using generally known, but not yet developed steps.

* Current address: Heuristic Physics Laboratories, Inc., 1649 S. Main St. Milpitas, CA 95035

## References

[1] The first modern planar fabrication process was described in Kemmer, "Improvement of detector fabrication by the planar process", Nucl. Instr. and Meth. 226 (1984) 89-93. The first VLSI chip to be used for their readout was described in the same conference: J. Walker, S. Parker, B. Hyams, S. Shapiro, ``Development of high density readout for silicon strip detectors", Nucl. Instr. and Meth. 226 (1984) 200-203.

[2] Atlas inner detector technical design report, 1 (30 April 1997) 7; J. Matthews, et al., "Bulk radiation damage in silicon detectors and implications for ATLAS SCT", ATLAS note INDET-NO-118, 12 Dec. 1995; R. Wunstorf, ``Radiation hardness of silicon detectors: current status", IEEE Trans. on Nucl. Sci. 44 (1997) 806.

[3] http://pluto.mpi-hd.mpg.de/~ktkno/www.html#intr

[4] S. Parker, C. Kenney, J. Segal, "3D -- A proposed new architecture for solid-state radiation detectors", Nucl. Instr. and Meth. A 395 (1997) 328-343.

[5] R. Sonnenblick, et al., ``Electrostatic simulations for the design of silicon strip detectors and front-end electronics", Nucl. Instr. and Meth., A 310 (1991) 189.

[6] M. J. Little, R. D. Etchells, J. Grinberg, S. P. Laub, J. G. Nash, and M. W. Yung, "The 3-D Computer", Proceedings: International Conference on Wafer Scale Integration, San Francisco, Jan. 3-5, 1989, pp 55-64.

[7] T. R. Anthony and H. E. Cline, "Deep-diode arrays", J. Appl. Physics 47 (1976) 2550.

[8] G. E. Alcorn, K. A. Kost, and F. E. Marshall, "X-ray spectrometer by aluminum thermomigration", Int. Electron Devices Meeting, Technical Digest, 82 (1982) 312-315.

[9] T. R. Anthony, "Diodes formed by laser drilling and diffusion", Journal of Applied Physics 53 (1982) 9154-9164.

[10] H. Takato, et al., "High performance CMOS surrounding gate transistor (SGT) for ultra high density LSIs", IEDM (1988) 222; S. Watanabe, et al., "A novel circuit technology with surrounding gate transistors (SGT's) for ultra high density DRAM's", IEEE J. of Solid-State Circuits, 30 (1995) 960; S. Maeda, et al., "Impact of a vertical-shape transistor (V T) cell for 1 Gbit DRAM and beyond", IEEE Trans. on Electron Devices, 42 (1995) 2117.

[11] J. Bryzek, K. Petersen, W. McCulley, "Micromachines on the march", IEEE Spectrum, 31 (May 1994) 20.

[12] Surface Technology Systems Ltd., Imperial Park, Newport, NP1 9UJ, UK; ST Systems USA, Inc., Redwood City, CA.

[13] Solecon Labs, Inc., 2241 Paragon Drive, San Jose, CA, (www.solecon.com).

[14] S. O. Rice, "Mathematical analysis of random noise, Part III: Statistical properties of random noise currents", Bell Sys. Tech. J., 24 (1945) 55.

[15] W. Adam, et al., "Diamond particle detectors" submitted to Elsevier, 1 Oct. 1997; Harris Kagan, "Advances in diamond tracking detectors", (talk at 1997 Hiroshima@Melbourne Conference on Semi-Conductor Tracking Devices).

[16] M. Alam, et al., "Technical Specifications of the First Prototype Pixel Sensors for ATLAS," August, 1997.

[17] F. Arfelli, et al., "A high efficiency single photon counting silicon matrix for Position Sensitive X-ray Detection," proceedings of the 1997 IEEE Nuclear Science Symposium, Albuquerque, NM.

[18] C. J. Kenney, S. I. Parker, V. Z. Peterson, W. J. Snoeys, J. D. Plummer, C. H. Aw, "A Prototype Monolithic Pixel Detector," Nucl. Instr. Meth. A342 (1994) 59-77.

# Mechanics and Cooling of the ALICE Inner Tracking System

W. Klempt for the ALICE Collaboration

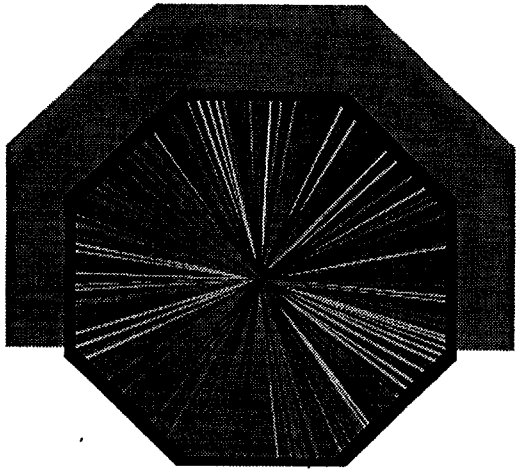

- Layout and Design of the ITS
- Silicon Pixel Detector
- Silicon Drift Detector
- Silicon Strip Detector
- Alignment
- Conclusion



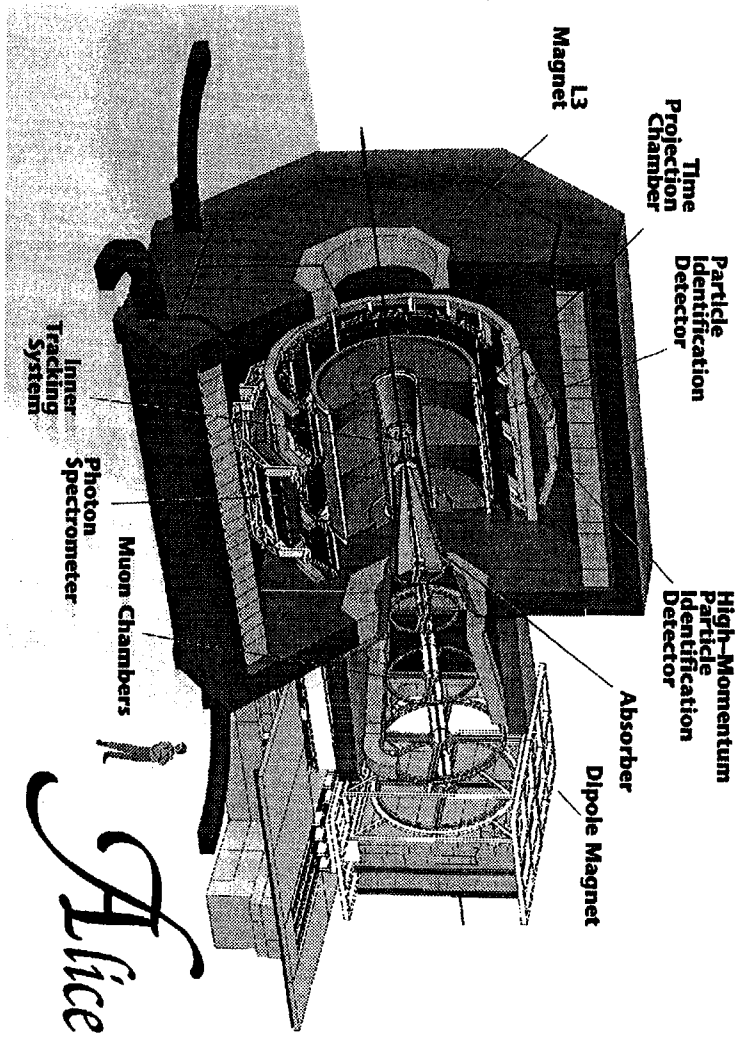

# ALICE schedule

- 1997 - 1998
  - R&D, design, prototypes
- July 1998 - June 1999
  - Technical design reports
- 1999 - 2003
  - Production
- 2002
  - L3 dismantling
- 2003
  - Pre-assembly & test in SXL hall
- 2004
  - Installation in P2 experimental area
- 2005
  - 6 month comissioning of detector
  - Ready for pp beam mid 2005

# ITS main Parameters

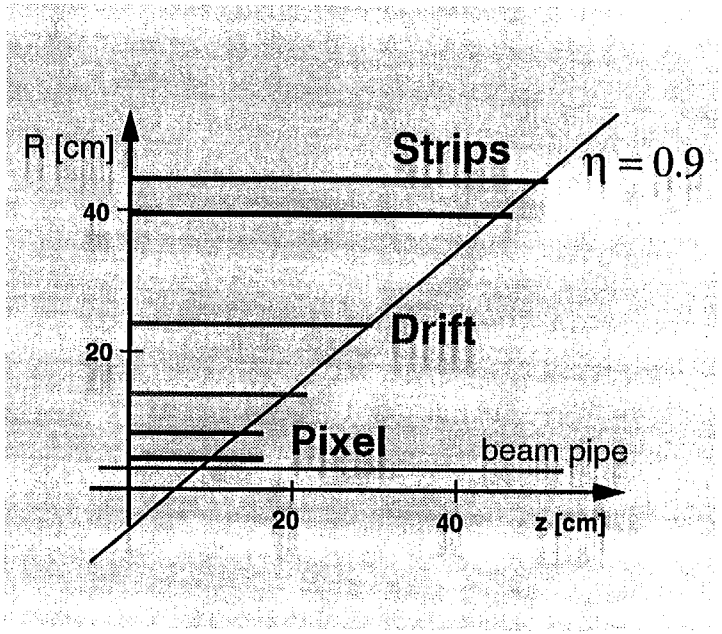


| | σrφ μm | σz μm | No. of Ch. k | Area m² | Power W | $X_0$ % |
|---|---|---|---|---|---|---|
| Pixel | 15 | 90 | 15727 | 0.26 | 500 (100) | 1.26 |
| Drift | 20 | 30 | 192 | 1.26 | 2000 1000 | (1.13) |
| Strips | 30 | 860 | 2620 | 5.12 | 1800 1000 | 1.74 |

## ITS Responsabilities

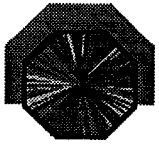

- **Pixels**

  **Bari, Catania, CERN, Padua, Rome, Salerno**

- **Drift**

  **Catania, Jyväskylä, Ohio, Rez, Turin, Trieste**

- **Strips**

  **Kharkov, Kiev, Nantes, Strasbourg, Turin, Utrecht-NIKHEF**

- **Mechanics, Cooling and Alignment**

  **Jyväskylä, Nantes, Padua, St. Petersburg, Turin, Utrecht-NIKHEF**

## General Design Concepts

- Material:
  - minimize radiation length
    high Young modulus
    => use unidirectional carbon fibre
  - Optimize thermal and mech. properties
    =>cyanate resin
  - maximise fibre/resin ratio

- Geometry:
  - minimize material for required stiffness
  - reasonable modularity for maintenance

- Operation at Room Temperature:
  - Minimize power consumption in barrel
    => div. of FEE in barrel and end-cap part
  - "leakless" water cooling for Pixel & Strips
  - evaporative $C_5F_{12}$ cooling for Drift

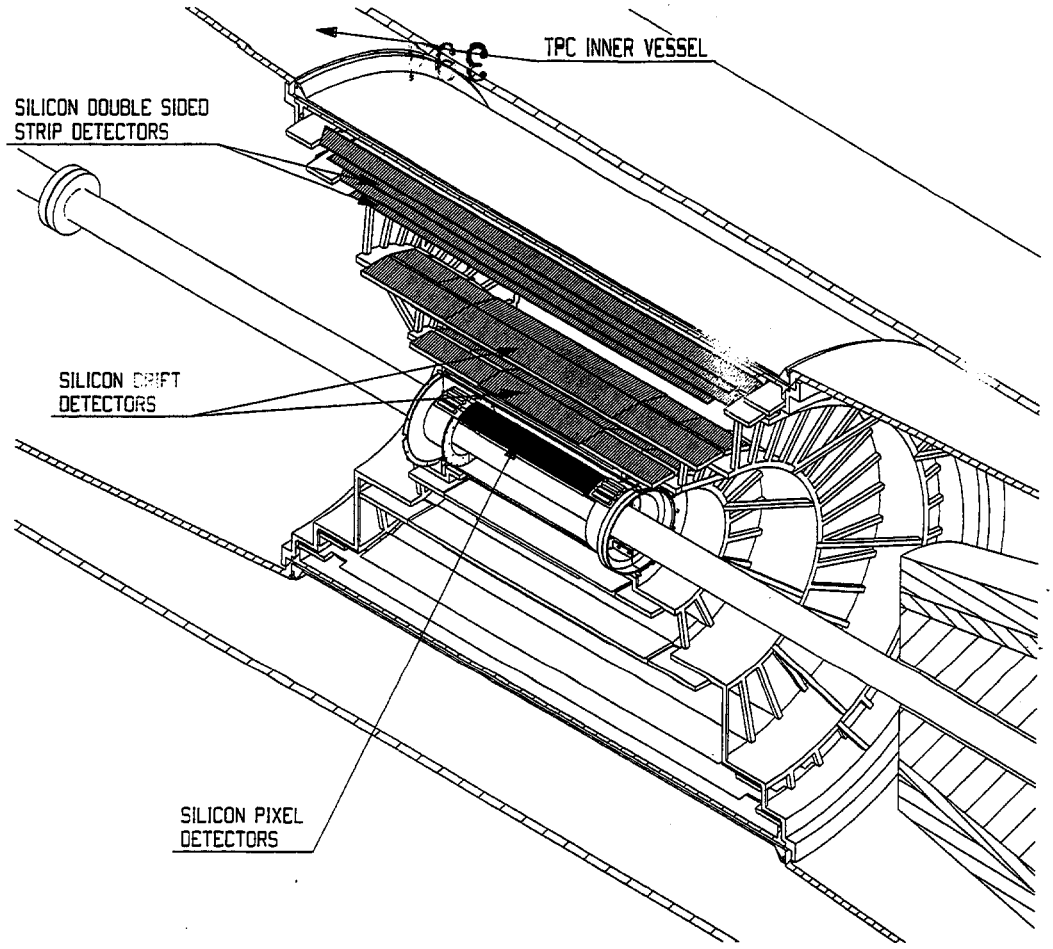


# ITS Mechanics

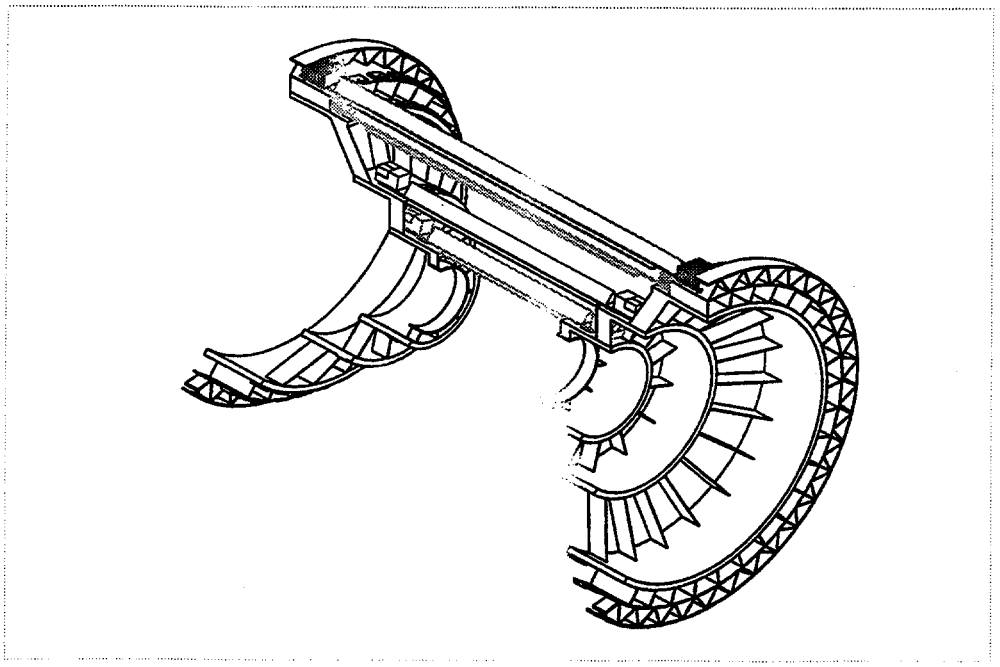

# ITS End Flange

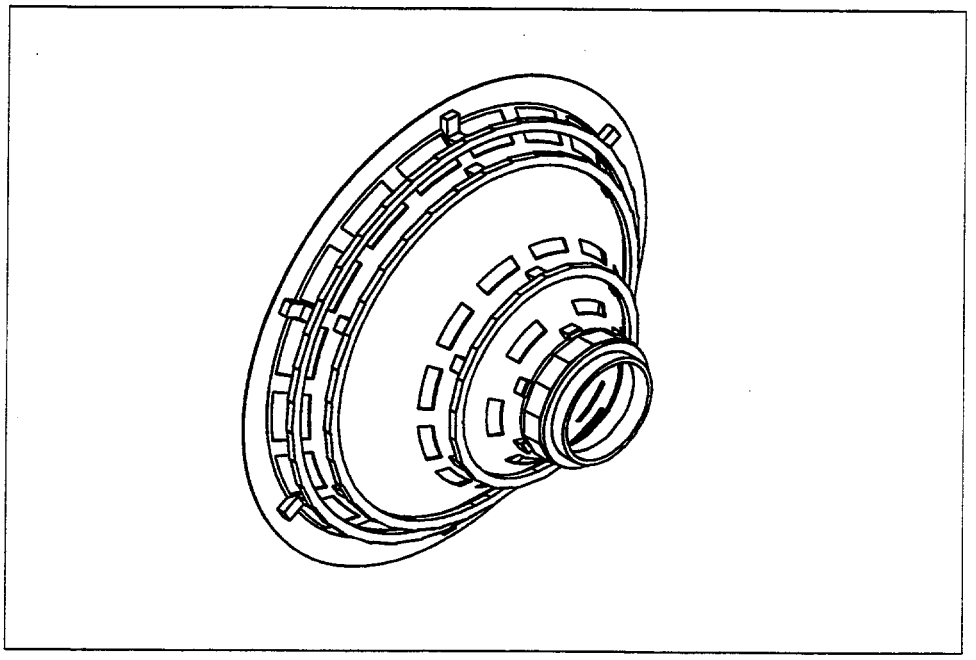

PROPOSITION DE REPARTITION
DES SERVICES (COOLING ELEC)
5 * 72 °

STRIP : -39 DETECTEURS : 4/5 X 8 C = 32
1/5 X 7 C = 7
TOTAL = 39

-35 DETECTEURS : 5/5 X 7 C = 35

DRIFT : -22 DETECTEURS : 3/5 X 4 C = 12
2/5 X 5 C = 10
TOTAL = 22

-14 DETECTEURS : 4/5 X 3 C = 12
1/5 X 2 C = 2
TOTAL = 14

PIXEL : -10 DETECTEURS : 5/5 X 2 = 10
TOTAL = 10

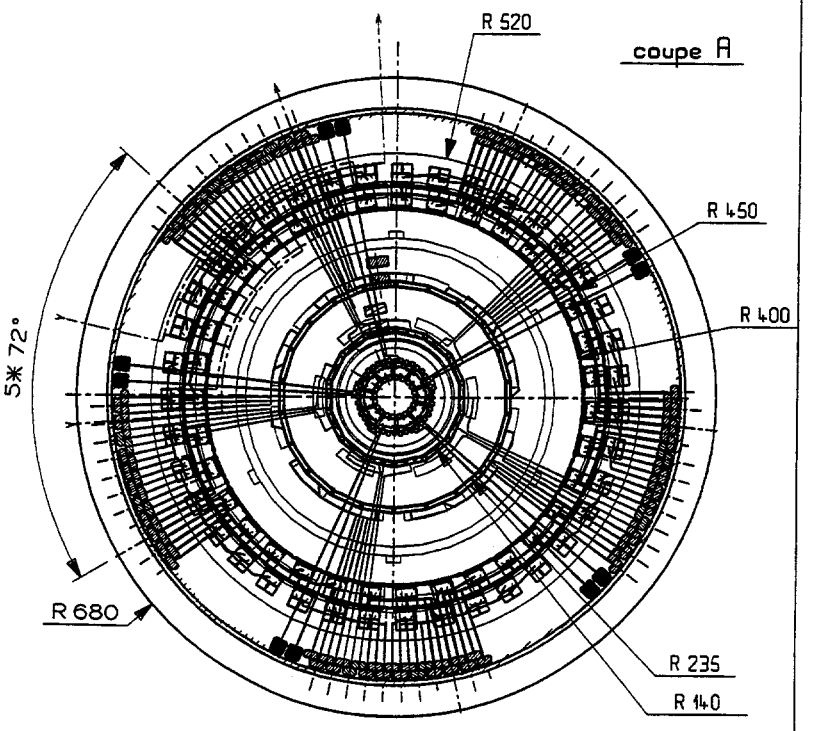

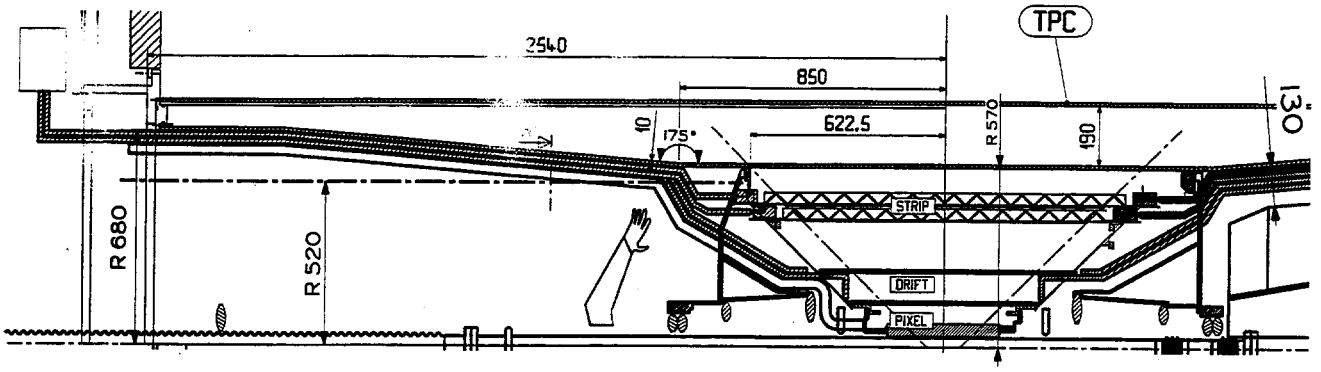


# Pixel Mechanics

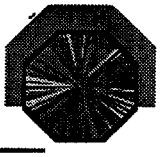

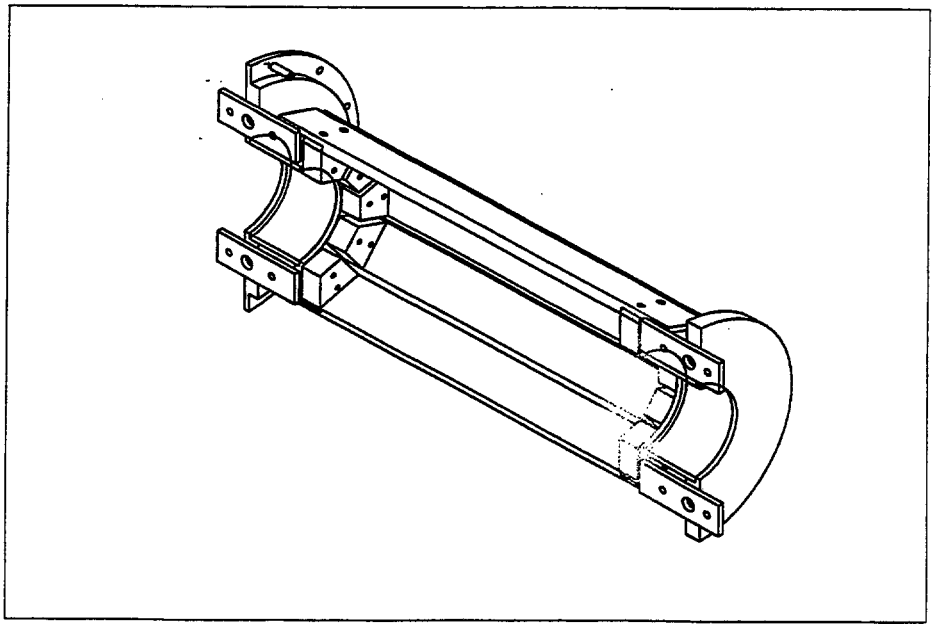

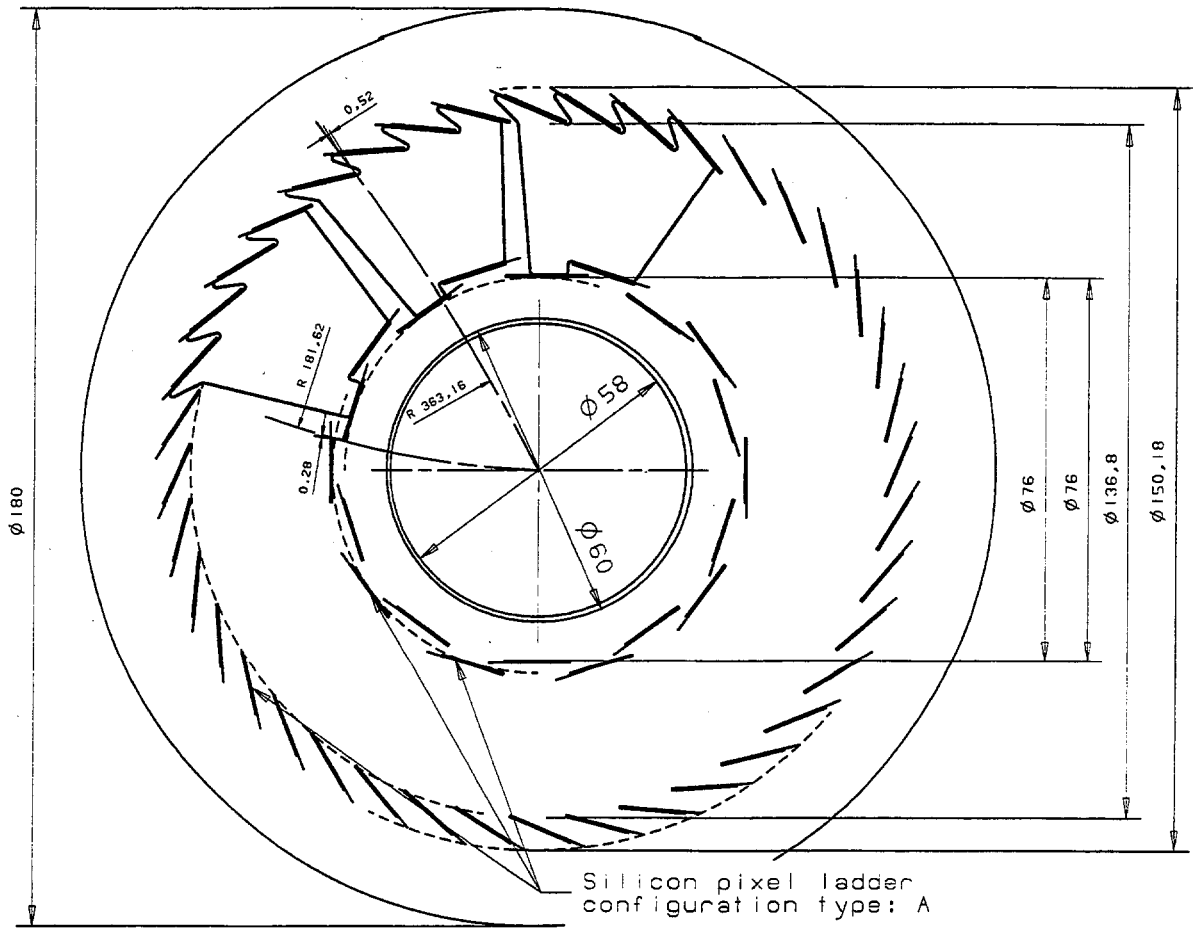
0,52
R 181,62
R 363,16
0,28
Ø58
Ø60
Ø180
Ø76
Ø76
Ø136,8
Ø150,18
Silicon pixel ladder
configuration type: A

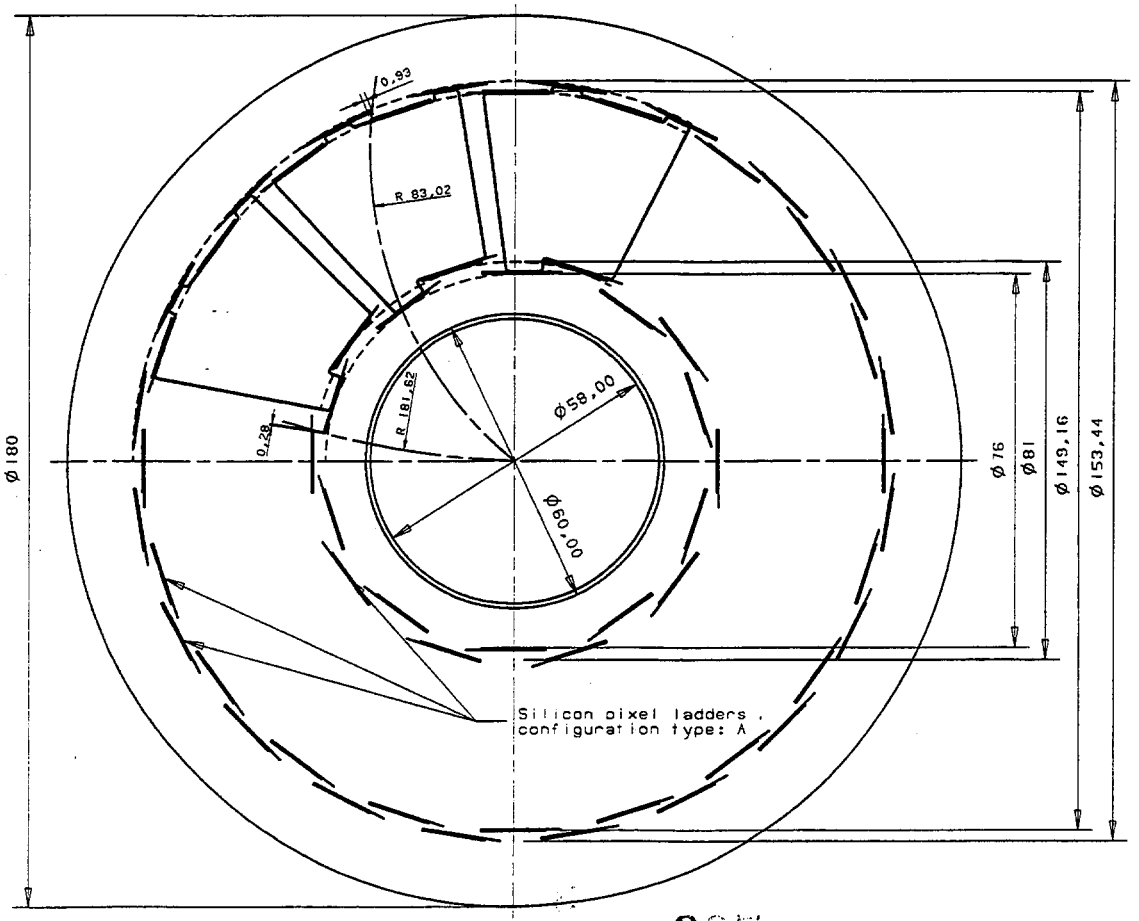
0,93
R 83,02
R 181,82
0,28
Ø58,00
Ø60,00
Ø180
Ø76
Ø81
Ø149,16
Ø153,44
Silicon pixel ladders
configuration type: A

# Pixel Ladder Prototype

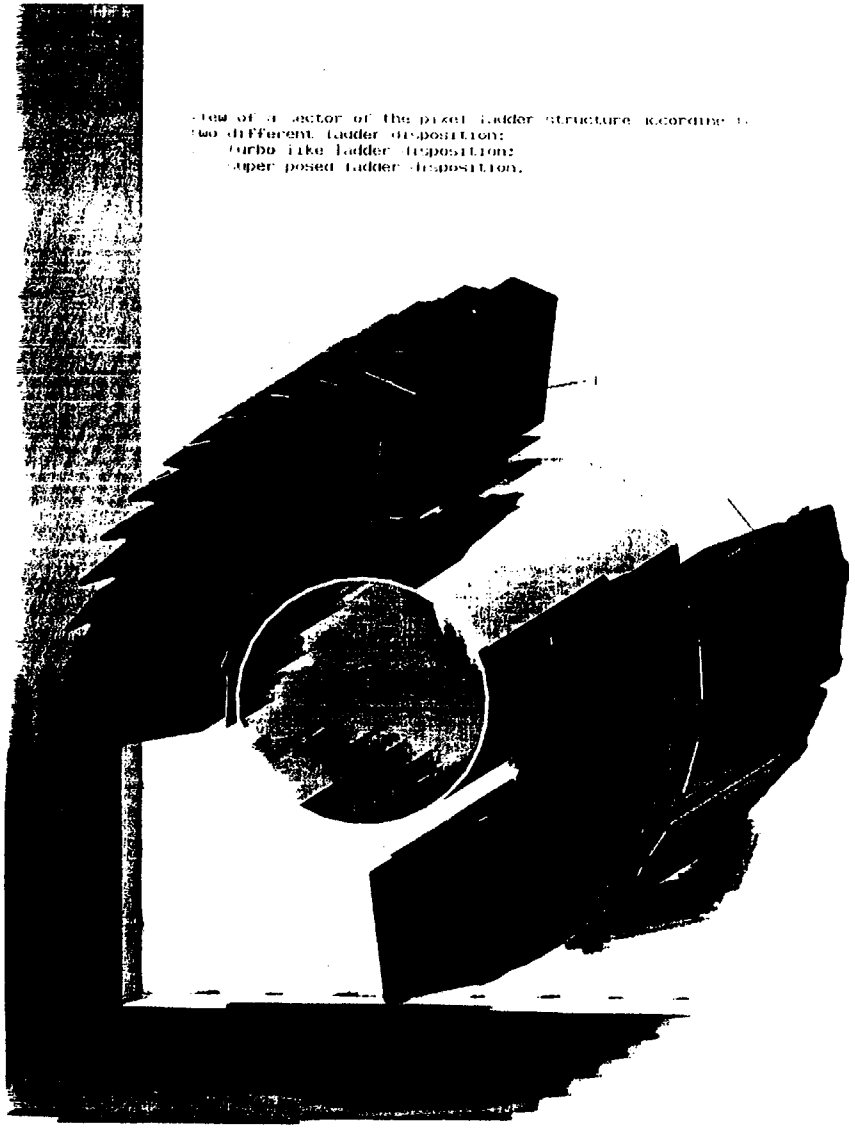


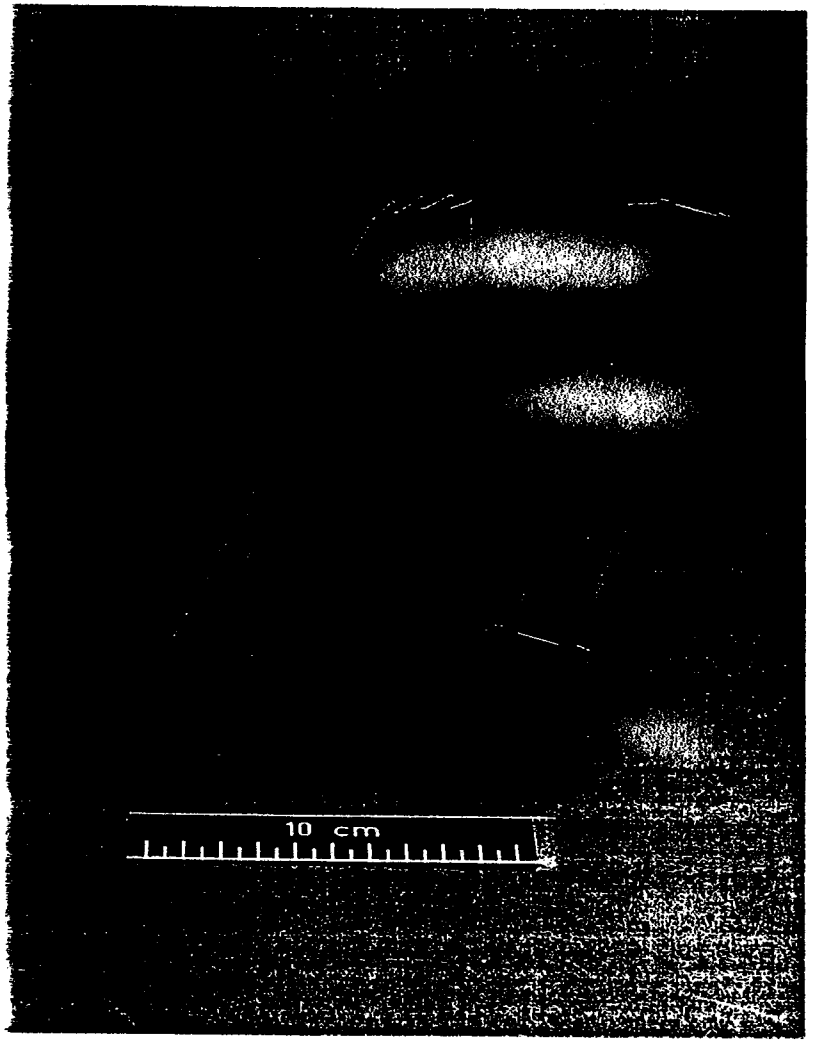

# Pixel Material Distribution

Average material seen by a particle traversing both layers = 1.26%$X_0$

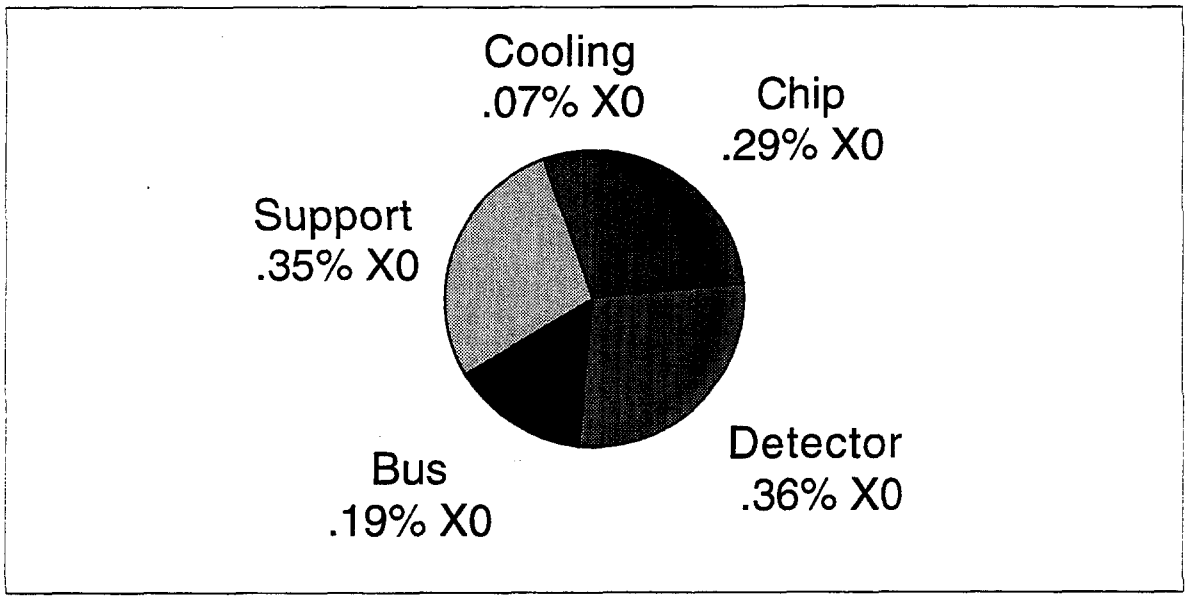


## Drift Ladder Design

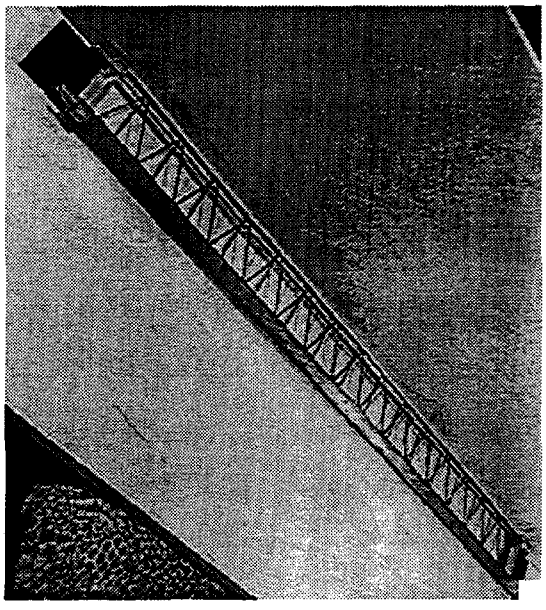

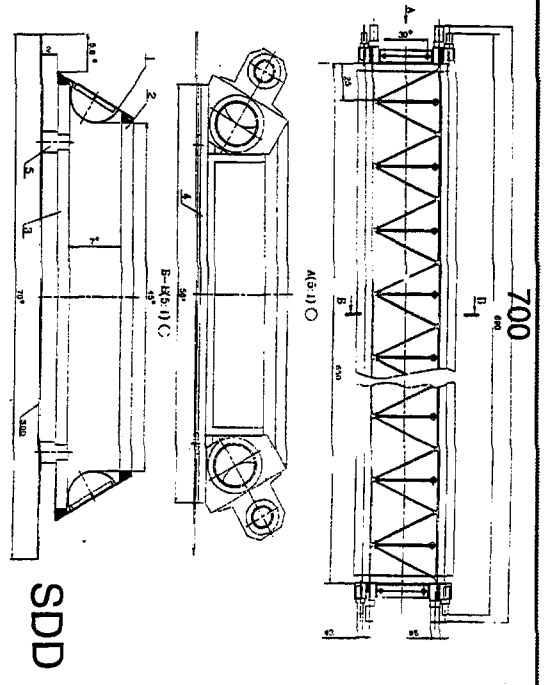

# Silicon Dr[illegible] Detector

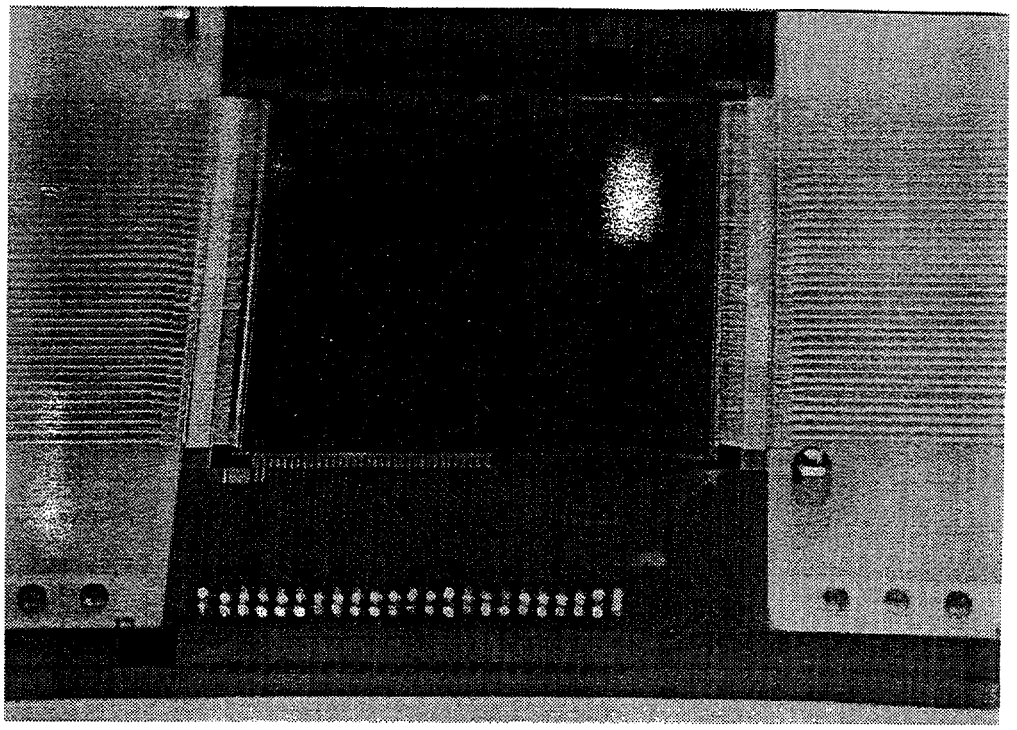

# $C_5F_{12}$ Vapour Pressure

**Saturated vapor pressure for FC5050 (C5F12) vs. temperature**

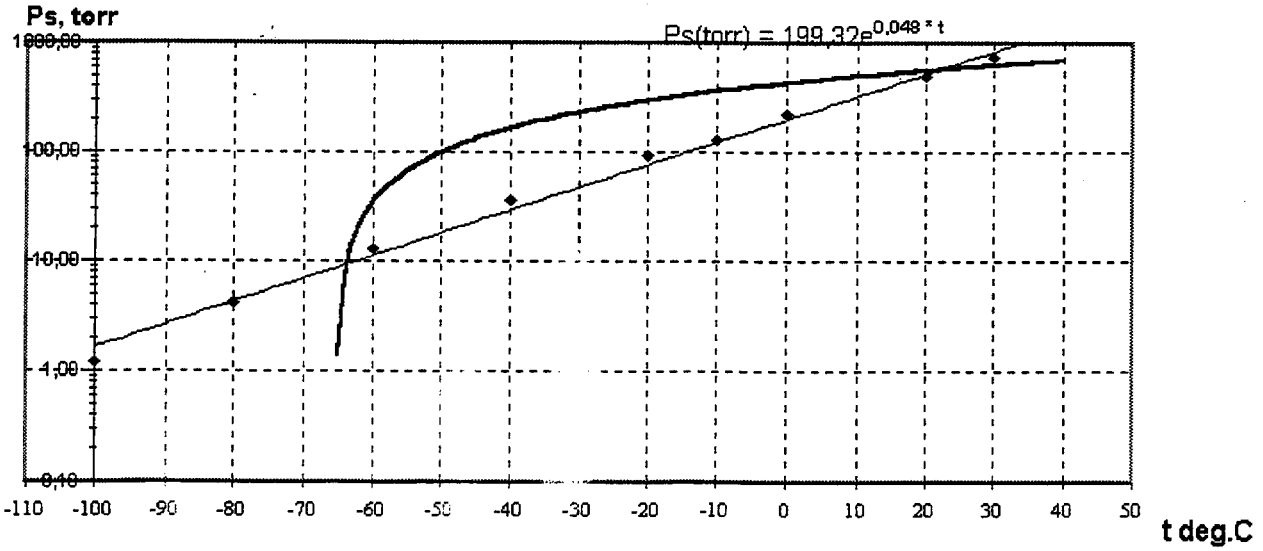

# Cooling Test Plant

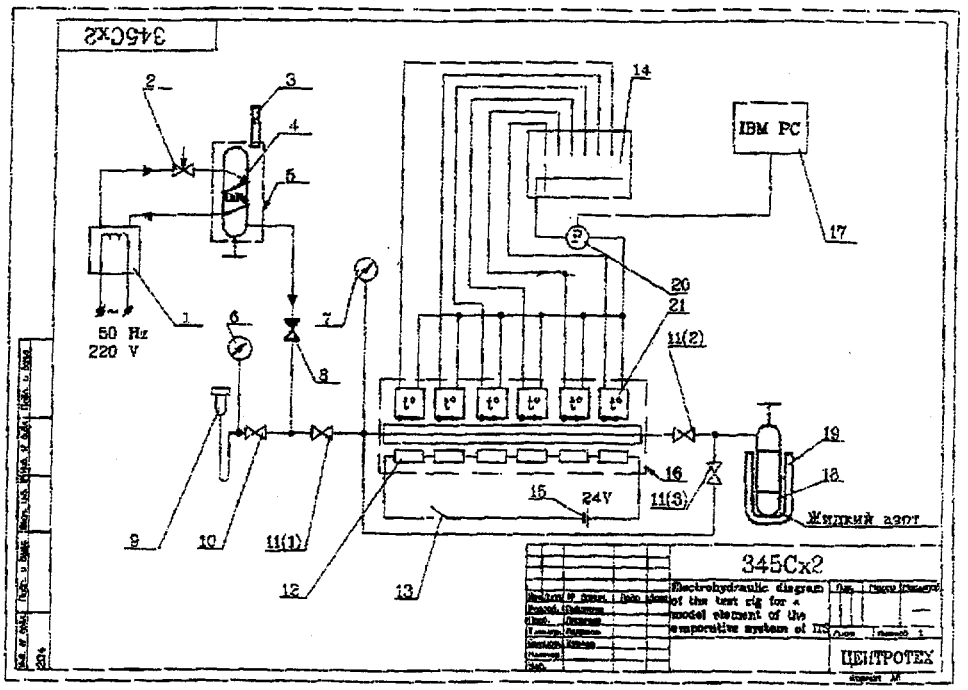


# Evaporative Cooling Test Setup

**Model of the evaporative cooling artery (ESQ)**

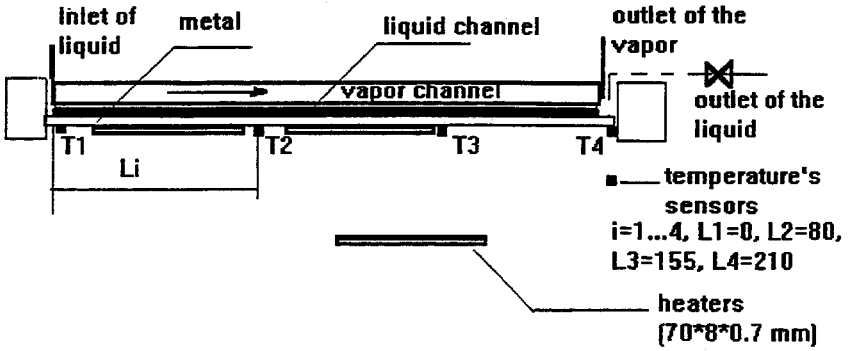

# Cooling Test Results

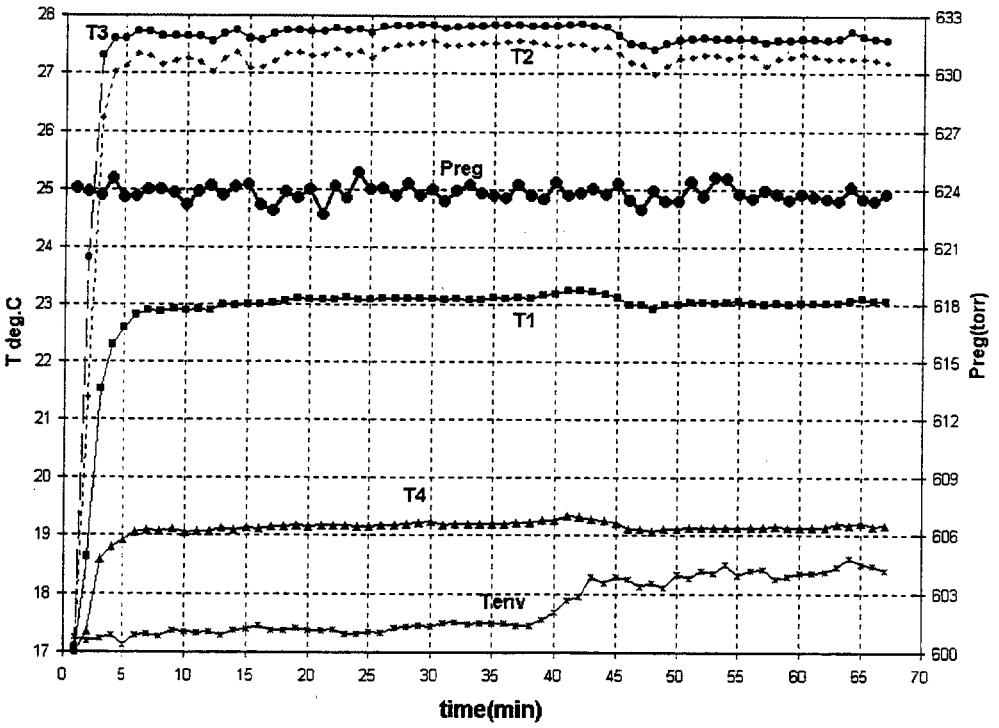


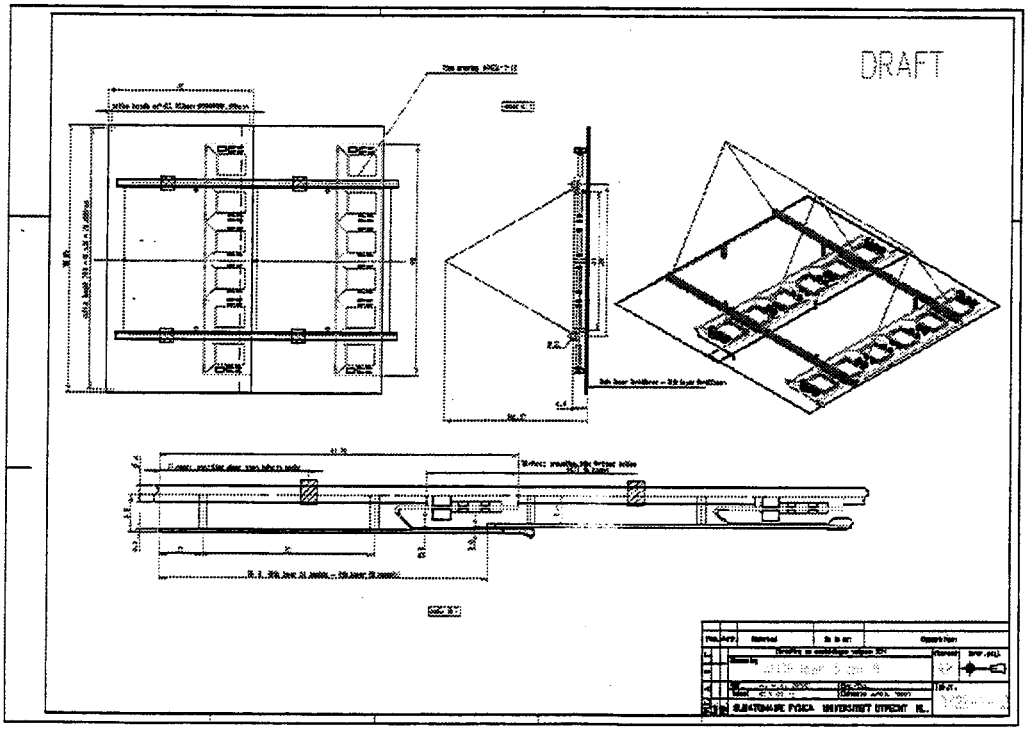

# Strip Detector

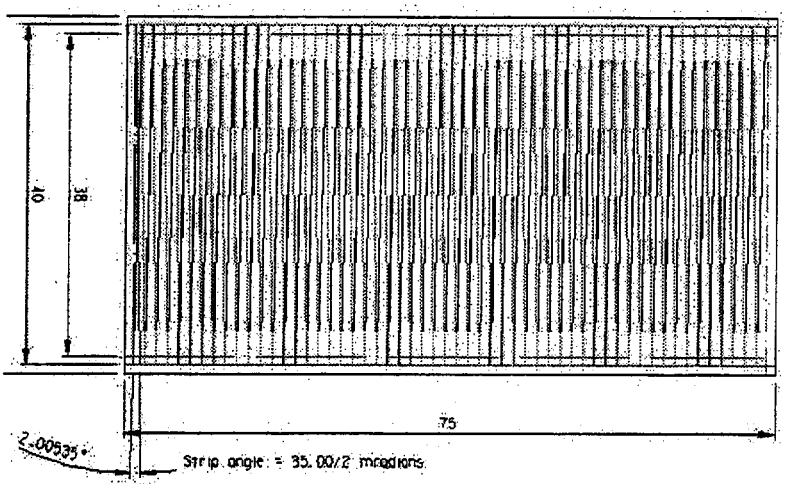


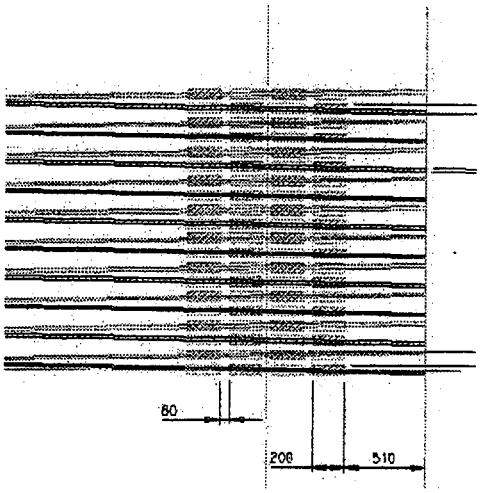


# Ladder Prototypes

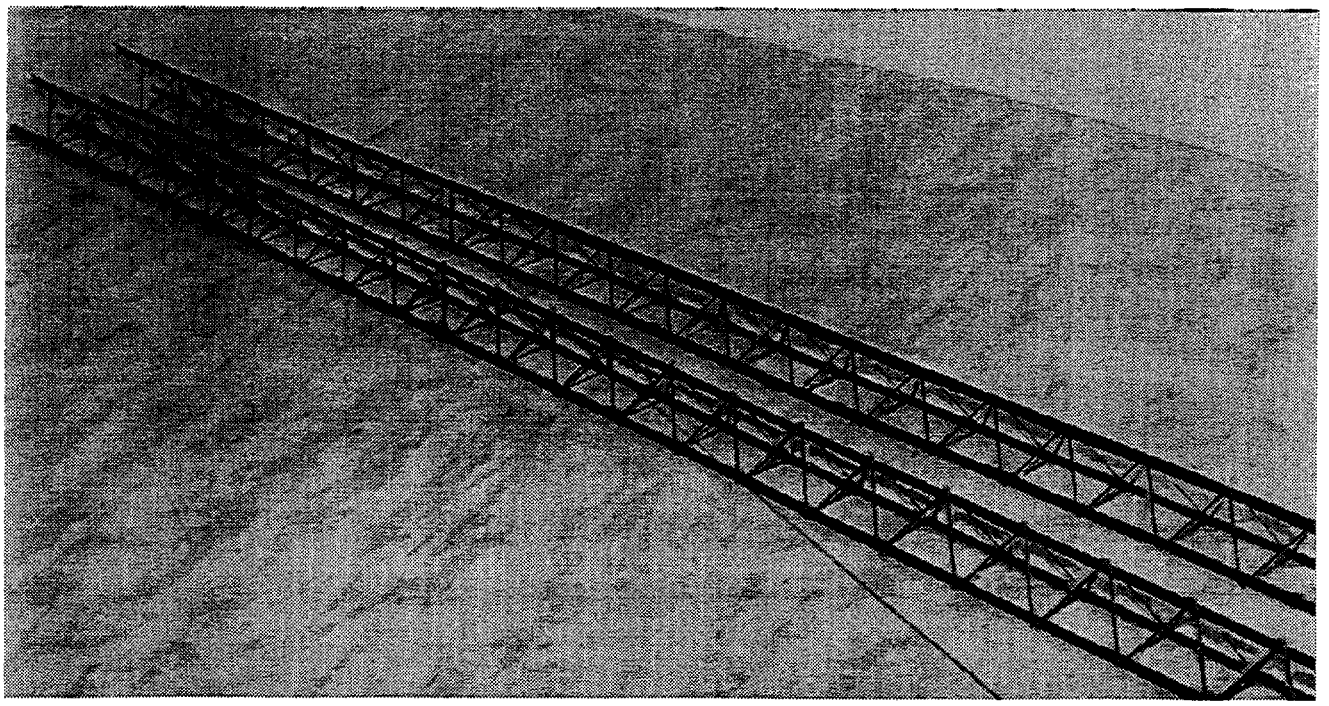

# Strip Detector Cooling Test

Use of high thermal conductive carbon fibre

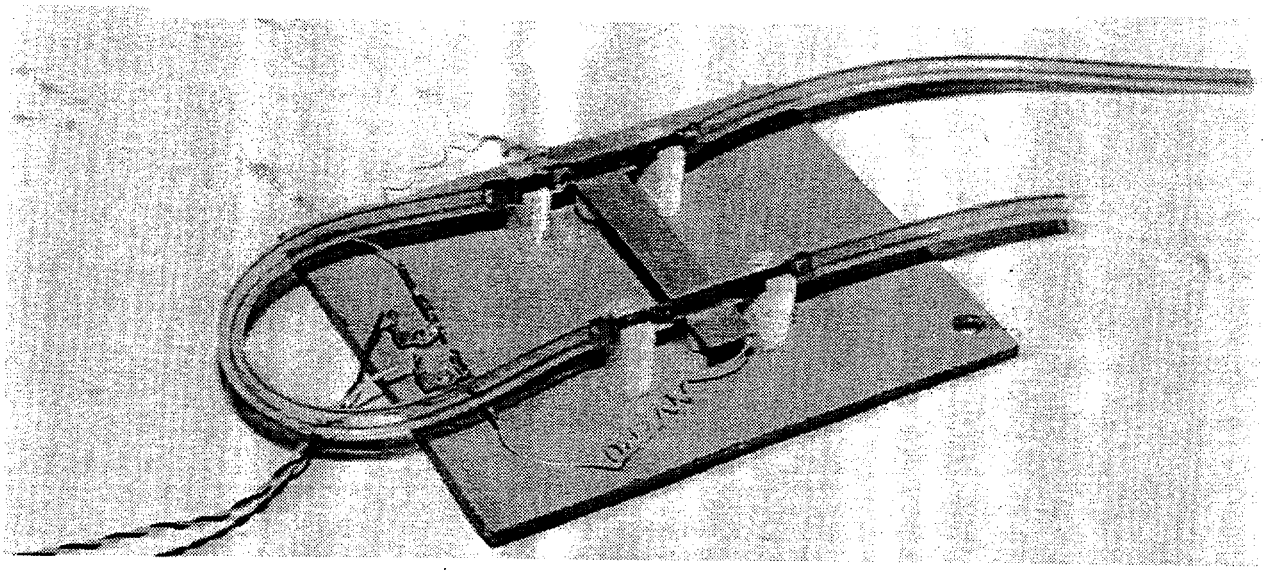

# Heat Bridge Test Setup

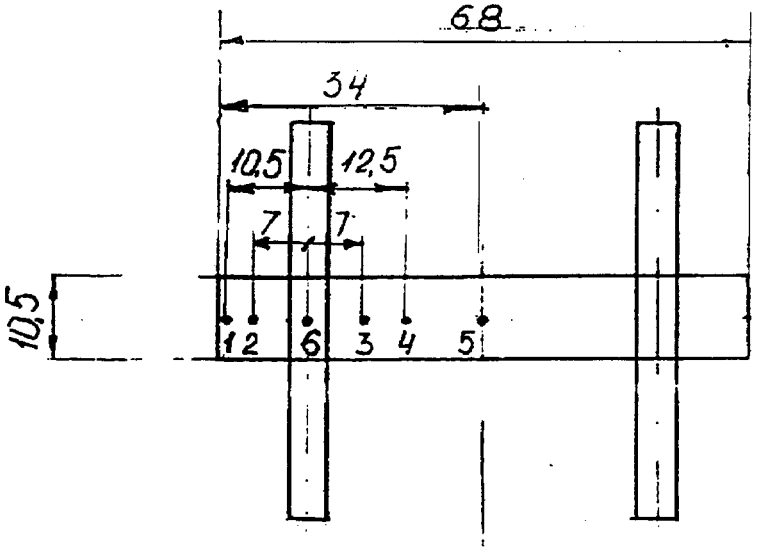

# Heat Bridge Cooling Test

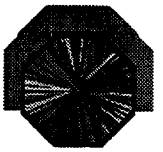

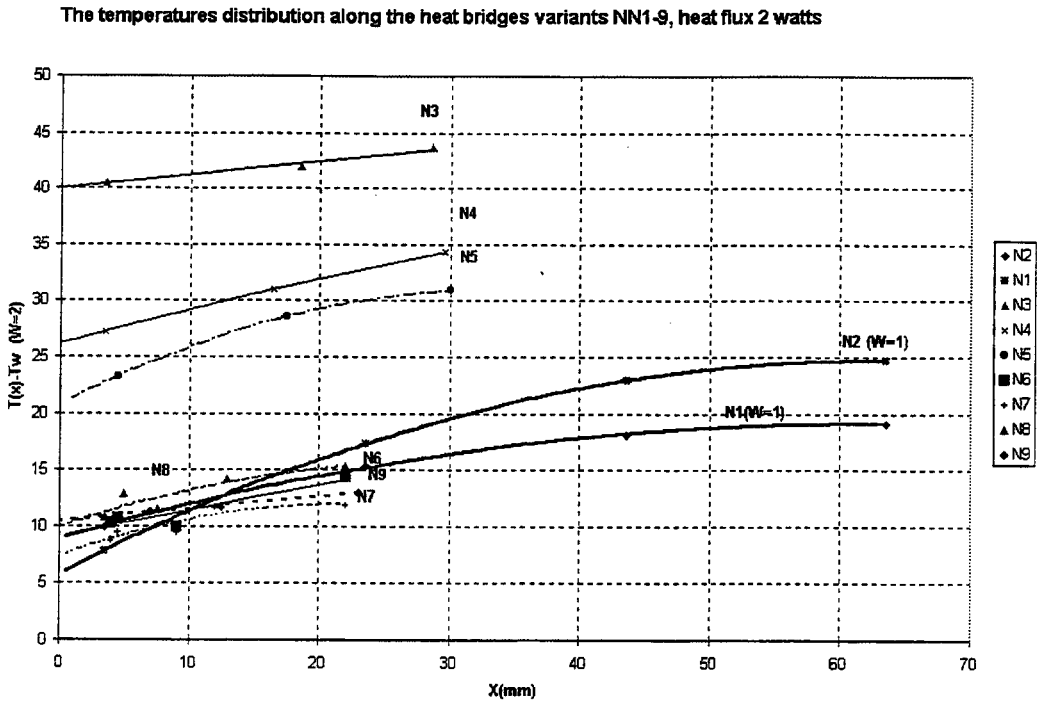


# Strip Material Distribution

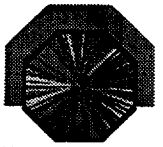

Average material seen by a particle traversing both layers = 1.74%$X_0$

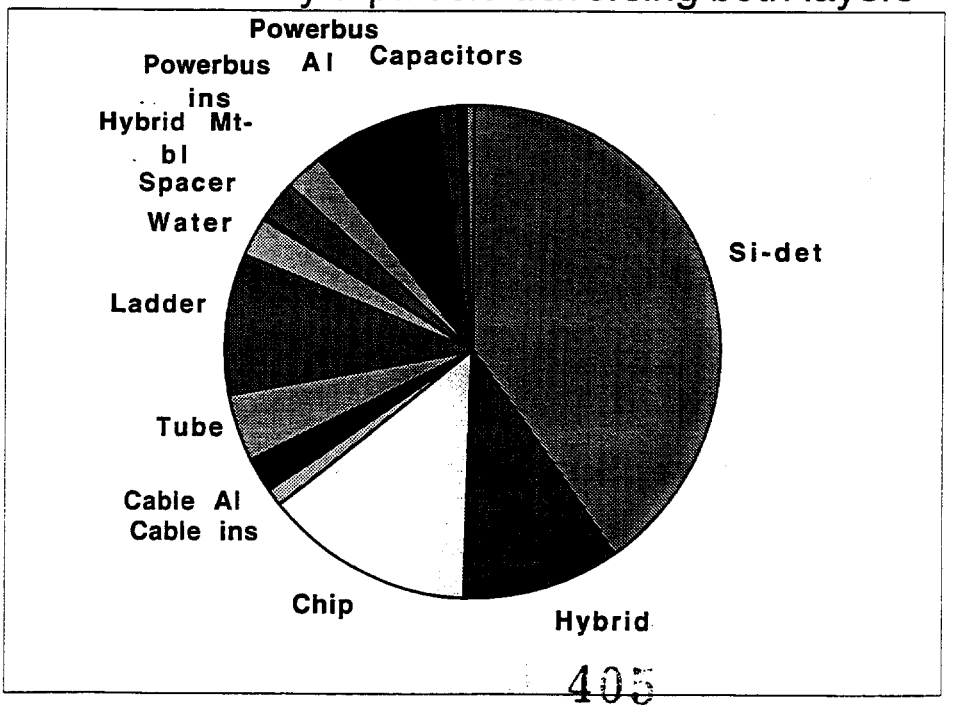

# Strip Ladder Assembly

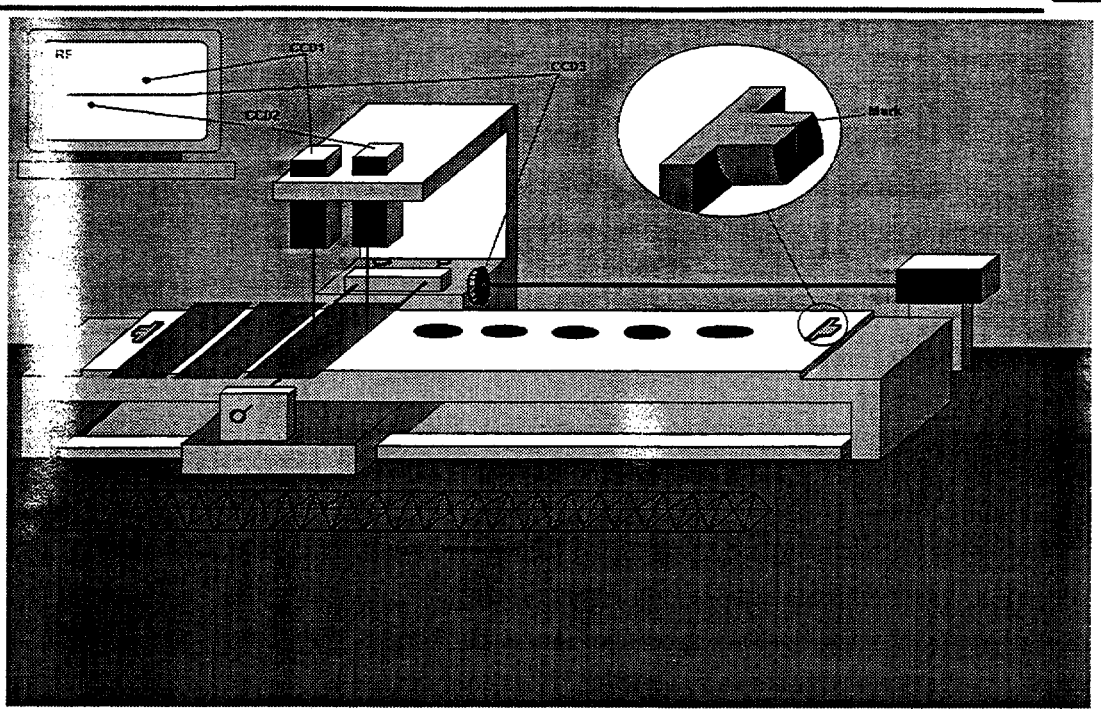


# ITS Assembly

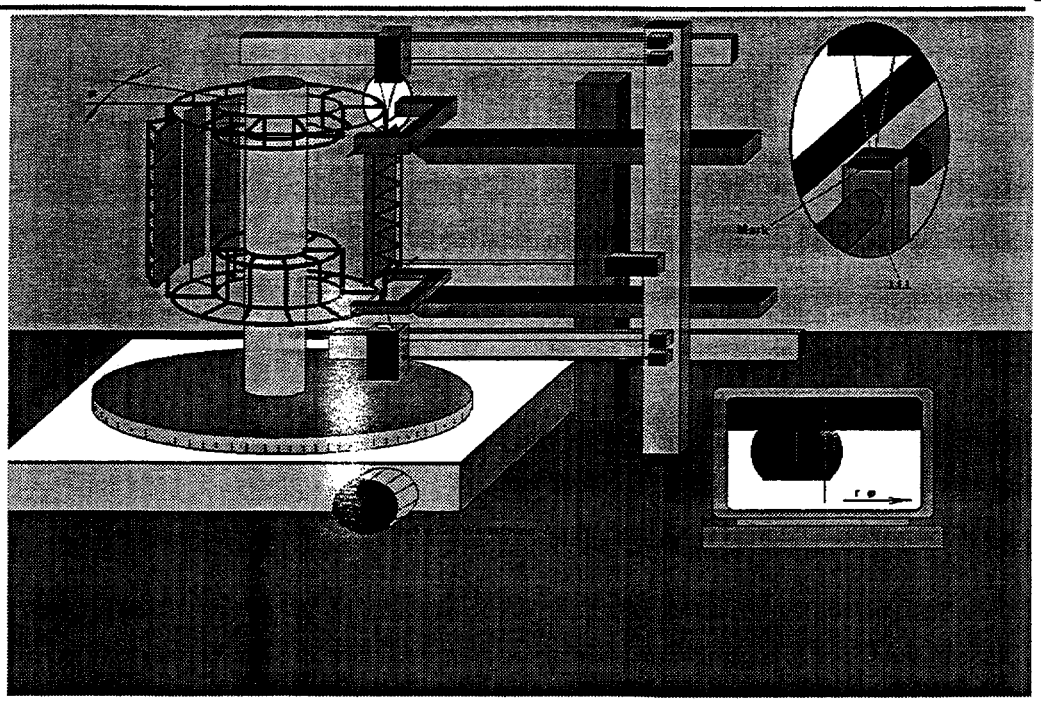

# Ladder Alingment

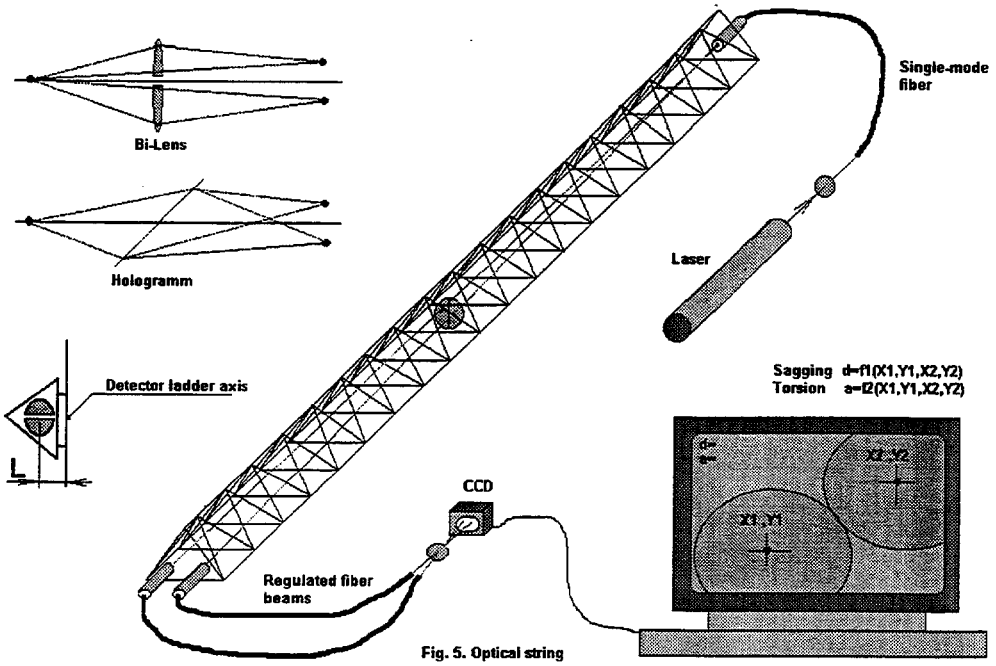


Fig. 5. Optical string

# Measurement of Ladder Sagging

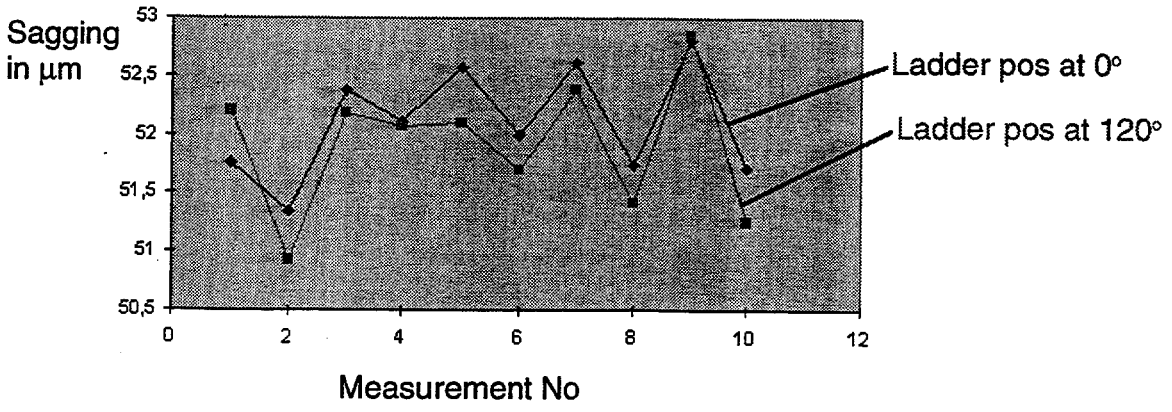

# ITS Strip Alignment

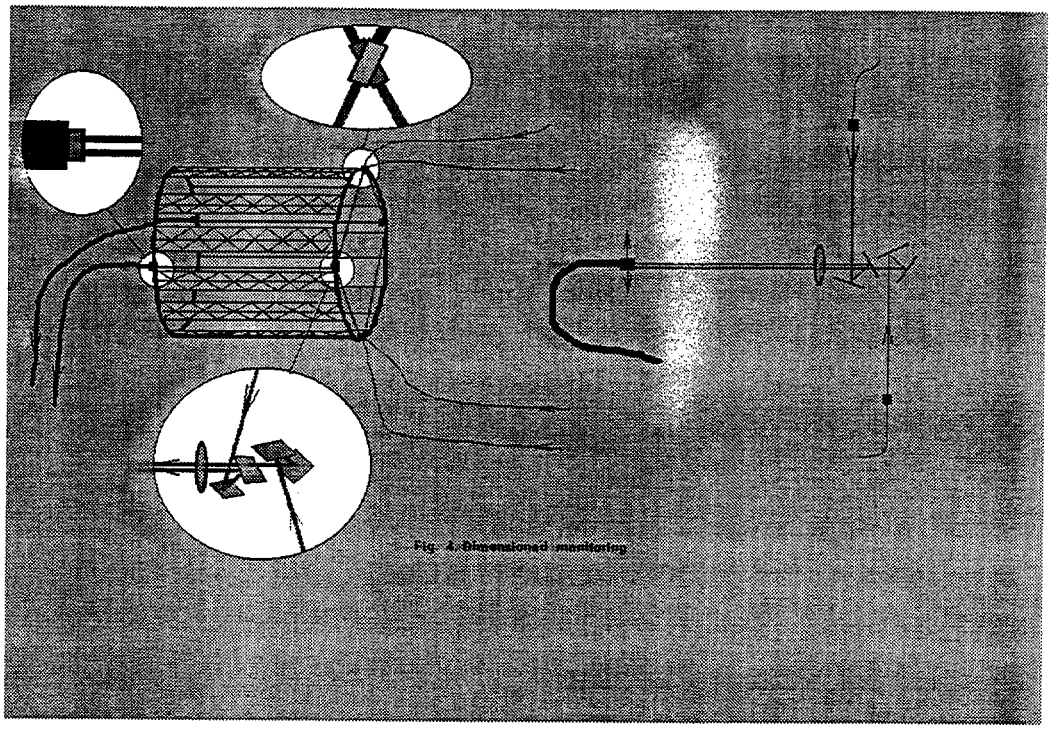

# General ITS Alignment

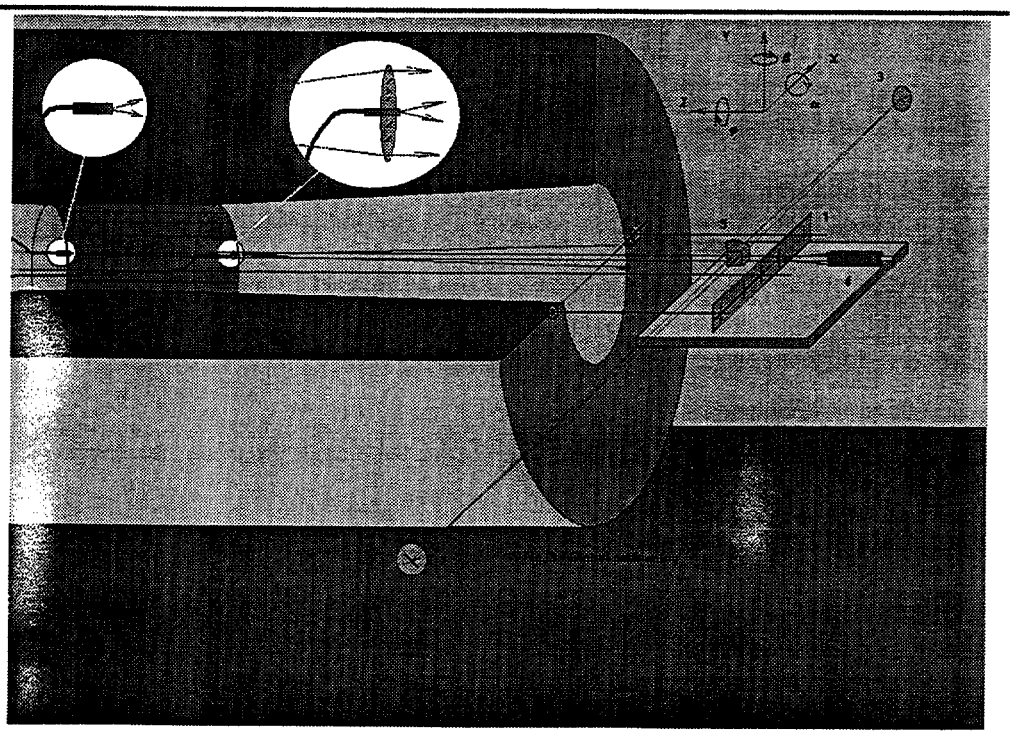

## ATLAS PIXEL DETECTOR COOLING REQUIREMENT

- 2228 PIXEL MODULES, EACH DISSIPATING ~ 5.5 WATTS
  ⇒ TOTAL ~ 13 KW
  (NOT INCLUDING ~2KW DISSIPATION IN CABLING WITHIN INNER DETECTOR VOLUME)

- MODULES ARRANGED ON 116 BARREL STAVES + 120 DISK SECTORS
  - ~33 W DISSIP.
  - L ~ 80cm, ~72W DISSIP.

- HEAT DISSIPATION OVER WHOLE OF DETECTOR AREA
  (NOT JUST AT END RINGS, AS IN MOST PRESENT GENERATION VXD's OPERATING Si STRIPS AT LOW ACCUMULATED DOSES)

- PIXEL SUBSTRATE TEMPERATURE REQUIRED TO BE LOWER THAN $-6^{\circ}C$ : $(-6^{\circ}C\ ^{+0^{\circ}C}_{-5^{\circ}C_{MAX}})$

  AIM FOR 10 YR OPERATIONAL LIFE FOR BARREL LAYERS AT 10.1 cm AND 13.2 cm RADIUS, + DISKS

  3LAYER (r ~ 4.3cm) REMOVAL NECESSARY ~ EVERY YEAR @ $10^{34}\ cm^{-2}\ s^{-1}$

- REQUIREMENT OF LOW $X_0$ AT LOW RADIUS PUSHES US TO REDUCE DETECTOR + ELECTRONICS THICKNESS + SUPPORTS AND SERVICES

# LOW MASS COOLING OF SILICON PIXEL AND STRIP DETECTORS BY FLUOROCARBON EVAPORATION.


G. HALLEWELL, CPPM.

R. BUDINSKY[+], G. HALLEWELL[*], G. LENZEN[#], J. THADOME[#], V. VACEK

* CPP MARSEILLE
\+ CZECH TECHNICAL UNIVERSITY, PRAGUE
\# WUPPERTAL UNIVERSITY.

## WHAT ARE THEY?

SATURATED (ie $C_nF_{(2n+2)}$) FLUOROCARBONS, MADE BY CHEMICAL SUBSTITUTION OF H BY F IN ANALAGOUS HYDROCARBONS

EXAMPLE: $C_4F_{10}$ – PERFLUOROBUTANE

- CONSIDERABLE BODY OF HV AND MATERIALS COMPATIBILITY EXPERIENCE IN H.E.P. COMMUNITY FROM LARGE RICH/CRID PROGRAMS AT CERN & SLAC
  - → $C_6F_{14}$, $C_5F_{12}$, $C_4F_{10}$, $C_2F_6$

## WHY COOL WITH THESE FLUIDS?

(i) NON - CONDUCTIVE

(ii) NON - TOXIC

(iii) NON - FLAMMABLE ($C_4F_{10}$ A HALON REPLACEMENT...)

(iv) NON - OZONE DEPLETING

(v) VERY LOW SOLVENT ACTIVITY
(3M MARKETS UNDER 'FLUORINERT' TM)

(vi) LOW - VISCOSITY (LIQUID PHASE WRT $H_2O$)

(vii) HIGH EXPECTED RADIATION RESISTANCE (NEEDS STUDIES)

HOWEVER: LIQUID PHASE Cp ONLY ONE QUARTER OF $H_2O$ → EVAP!!

ATLAS COOLING REVIEW RECOMMENDATION 10/97
TO REPLACE AQUEOUS COOLANTS WITH NON-CONDUCTIVE COOLANTS DUE TO RISK OF LEAK DAMAGE TO DETECTORS ↔ INNER DETECTOR – $70M.

# CPPM BiPhase Liquid (FC) - Gas($N_2$) Cooling System

## Fluorocarbon Candidates (1995 3-M data)

| Fluorocarbon | PF5030 * | PF5040 * | PF5050 * | PF5060 * | PF5070 * | PF5080 * |
|---|---|---|---|---|---|---|
| Chem. Formula | $C_3F_8$ | $C_4F_{10}$ | $C_5F_{12}$ | $C_6F_{14}$ | $C_7F_{16}$ | $C_8F_{18}$ |
| Mean Mol. Wt | 188 | 238 | 288 | 338 | 388 | 438 |
| Bp (1 atm) | -37°C | -2°C | 30°C | 56°C | 80°C | 101°C |
| Dens. ($gcm^{-3}$) | 1.35 (20°C) | 1.52 (20°C) | 1.63 (25°C) | 1.68 (25°C) | 1.73 (25°C) | 1.77 (25°C) |
| Liquid Viscos (cp) | 0.3 (0°C) | 0.46 (20°C) | 0.45 (25°C) | 0.67 (25°C) | 0.95 (25°C) | 1.4 (25°C) |
| Surface Tens. ($dy.cm^{-1}$) | 4.3 (0°C) | 7.4 (20°C) | 9.5 (25°C) | 12.0 (25°C) | 13.0 (25°C) | 15 (25°C) |
| Vapor Press. (@ -10°C: Torr) | 2200 | 550 | 130 | 58 | 12 | ~ 8 |
| LatHt Vap ($J\ mole^{-1}$) | 15717 | 22881 | 25281 | 29670 | 30815 | 40278 |
| Liq Vol Flow (90 W Load) ($cm^3s^{-1}$) | ~ 0,8 | ~ 0,6 | ~ 0,6 | ~ 0,6 | ~ 0,6 | ~ 0,5 |
| Gas Vol Flow (90 W Load) ($cm^3s^{-1}$) | ~ 50 | ~ 120 | ~450 | ~ 900 | ~ 3600 | ~ 4400 |
| Liquid-Gas Expansion Fact @ -10°C | ~60 | ~210 | ~ 720 | ~ 1500 | ~ 6000 | ~ 8800 |
| $\Delta p$ max for $\Delta T = 0.5°C$ (Torr) | ~ 38 | ~ 11 | ~ 3,2 | ~ 1,4 | ~ 0,4 | ~ 0,2 |

Refs: * 3M Speciality Fluids Newsletter Vol1 No. 1, April 1995
3M Speciality Chemicals Div, 3M Center, Building 223-6S-04 St Paul MN 55133-3223
Tel (612) 737-4019 Fax (612) 736-7542

- USE LATENT HEAT OF VAPORISATION (15-25 KJ/mole);
  WHICH IS MUCH HIGHER THAN LIQUID $C_p$.

  VERY LOW LIQUID FLOW RATES → THIN TUBES → LOW X/X0
  ($C_g$ ~ 0.7 $cm^{-3}s^{-1}$ FOR AN ATLAS PIXEL STAVE)

- SILICON OPERATING TEMPERATURE DEPENDS ON
  BOILING PRESSURE IN COOLING TUBES
  CONTROLLED BY PUMPING SPEED

- EXHAUST FLUID IN FORM OF VAPOR → LOW COOLANT X/X0

- USE OF TUBES ALLOWS WIDER CHOICE OF COOLING
  FLUIDS WITH BOILING PRESSURES DIFFERENT FROM
  DETECTOR VOLUME AMBIENT VACUUM ENVIRONMENT.

- VERY HIGH HEAT TRANSFER COEFFICIENT SHOULD
  EASE THE PROBLEM OF THERMAL IMPEDANCE
  BETWEEN SILICON AND COOLING TUBE.

FIGURE 11

Typical Heat Transfer Coefficients vs Heat Transfer Modes and Fluids

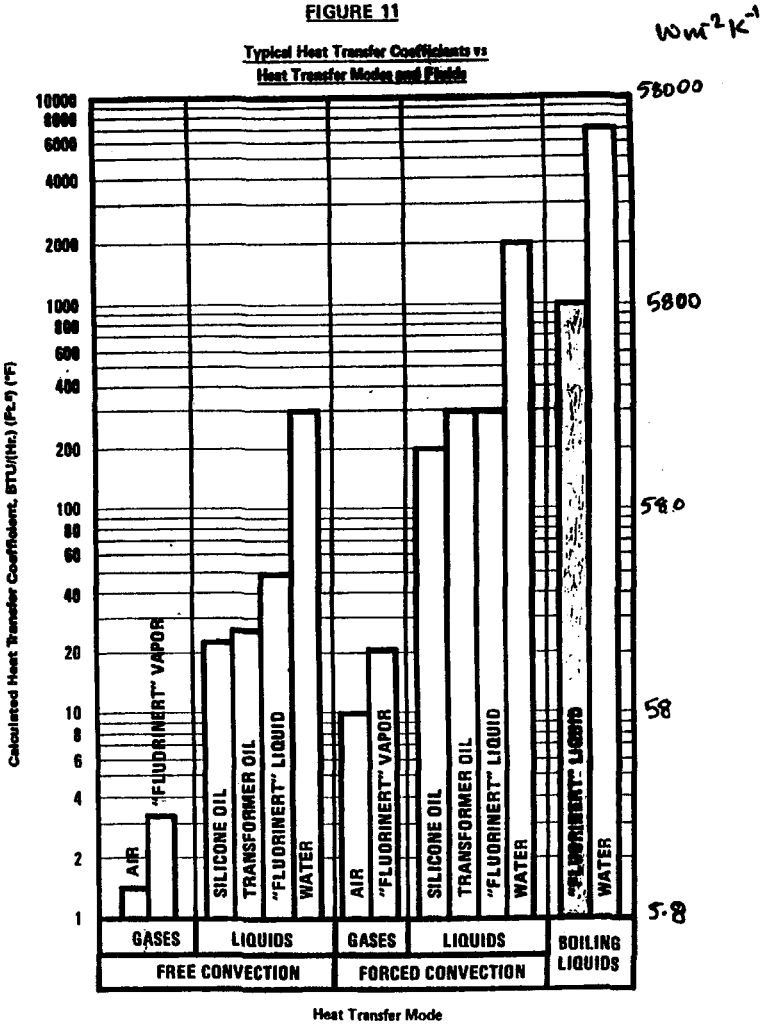

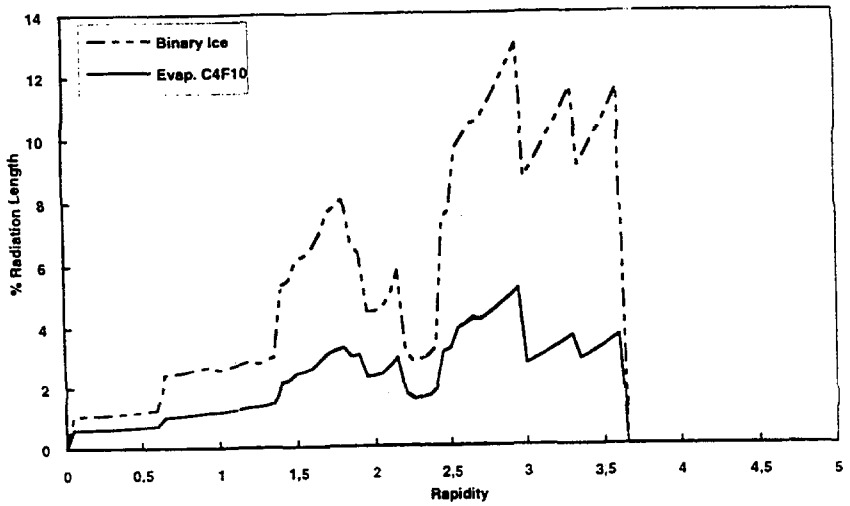


**Figure 10-88** Comparison of binary ice and fluorinert cooling assuming the service routings used in Tables 10-15-10-18.(B-layer services routed as listed in Table 10-15, to facilitate layer replacement).

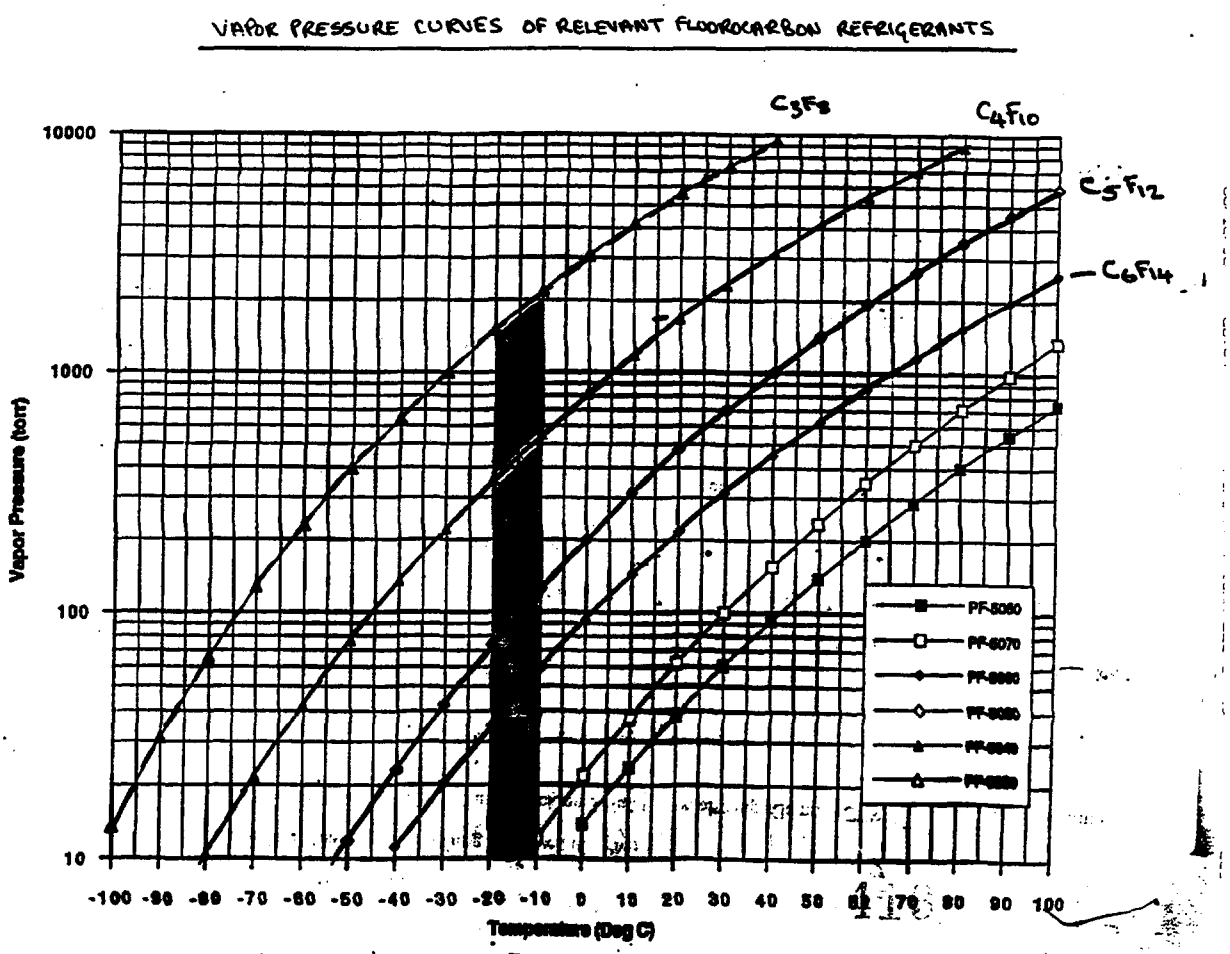


Figure 3-8. Vapor Pressure vs. Temperature for PF-5030 through PF-5080

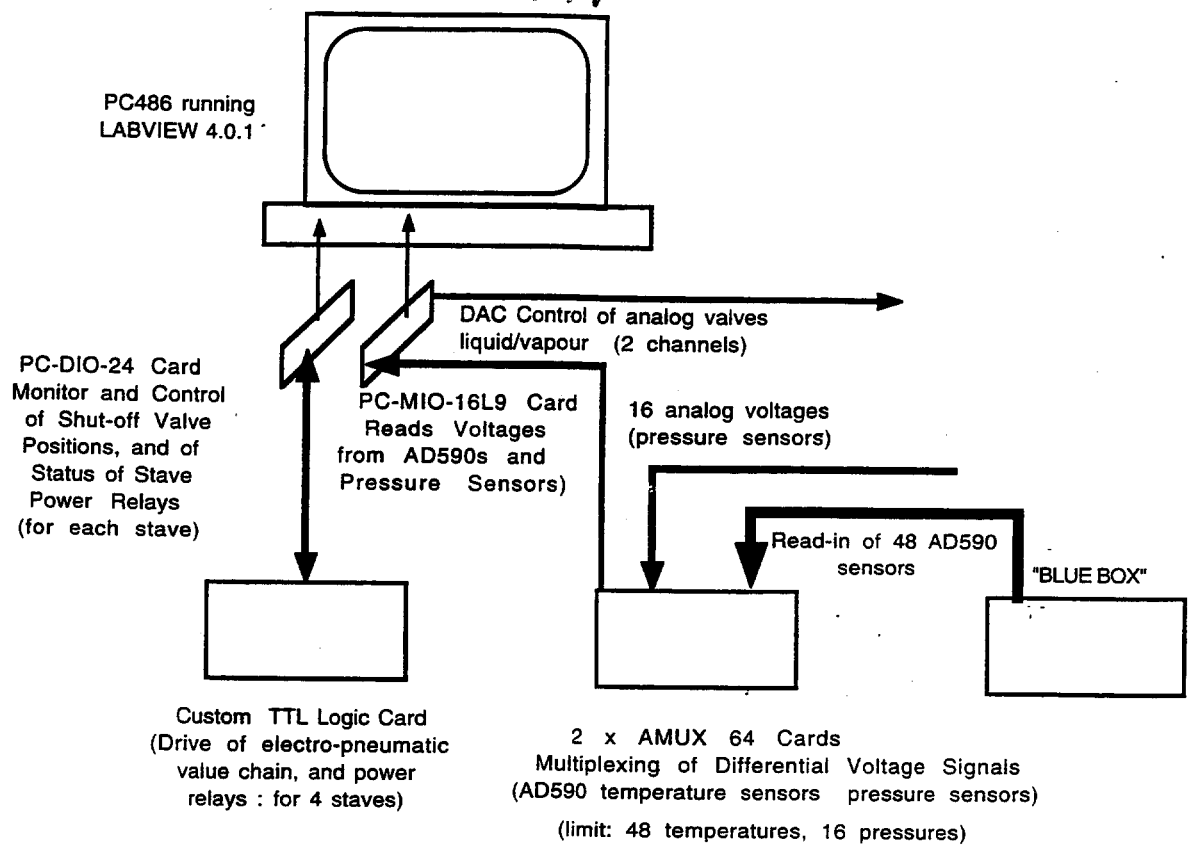


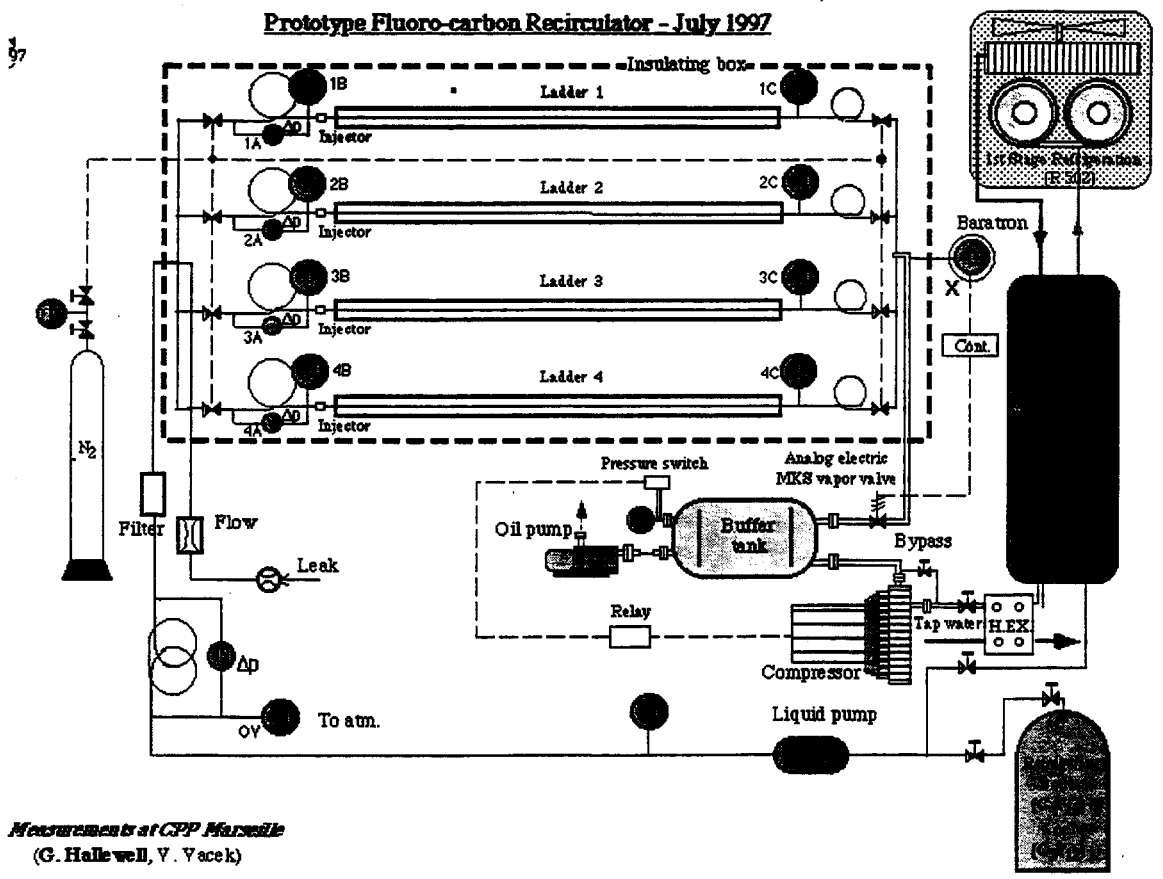


*Measurements at CPP Marseille*
(G. Hallewell, V. Vacek)

# Primary Pumps

## Varian 600DS Dry Scroll Pump

NEW

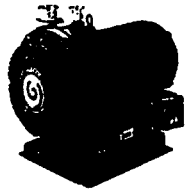

Outline Drawing inches [m

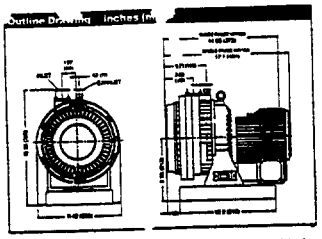

Varian's New 600DS Dry Scroll Pump incorporates a technology that produces clean, cost effective, and reliable vacuum pumping performance. Unlike many other types of dry pumps, the 600DS has both a low ultimate pressure and high pumping speed. With a base pressure in the $10^{-3}$ Torr range and superior pumping efficiency, it is suitable for applications where oil-sealed mechanical pumps have typically been used.

In the oil-free scroll pump, crescent-shaped pockets are formed and bounded by the meshed scrolls. As the orbiting scroll moves within the fixed scroll, these pockets progressively decrease in volume as they move the pumped gases in the spiral path from inlet to discharge. Sealing is accomplished with PTFE seals against anodized aluminum walls eliminating the need for oil sealing.

Because the scroll pump is intrinsically clean, there is no risk of contaminating your vacuum system. Conventional oil-sealed mechanical pumps require costly accessories (traps and baffles) to achieve only marginal levels of cleanliness. Since no oils are required, the costs of purchasing and disposal of them are eliminated. Few moving parts and carefully chosen materials of construction minimize pump failures, with typical maintenance intervals of twelve to eighteen months. All these factors contribute to low cost of ownership and maximum uptime.

Varian's 600DS Dry Scroll pump is the preferred choice for your clean, high-vacuum requirements.

| Features | Benefits |
|---|---|
| • Scroll Design | • Low ultimate pressure<br>• High speed<br>• Compact size<br>• Quiet, low vibration operation<br>• Two moving parts<br>Long service life |
| • Oil-Free | • No risk of oil contamination<br>• No expensive traps or filters<br>• No costs of buying and disposing of oil |
| • Carefully chosen construction materials | • Long life operation<br>• Low maintenance<br>• Low cost of ownership |

**Common Applications**

- Turbo-, Ion-, or Cryo-Pumped Systems
- Load Lock Chambers
- Leak Detection Systems
- Optics
- Research
- Any application where the presence of hydrocarbons is detrimental to your process





**Speed Curve**

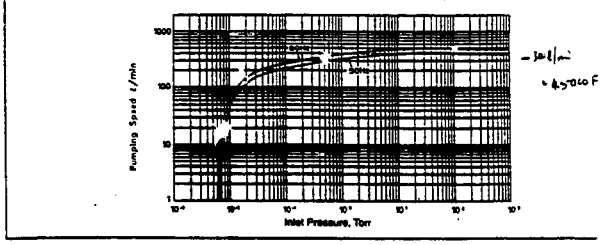


**Technical Specifications**

| | |
|---|---|
| **Free Air Displacement** | **Motor Rating** |
| 60 Hz 600 l/m (21 cfm) | 0.8 hp (0.6 kW) |
| 50 Hz 500 l/m (17.5 cfm) | **Electrical Suppl.** |
| **Pumping Speed** | 1 Phase, 50/60 Hz, 100/115/200/230 V |
| 60 Hz 600 l/m (17.5 cfm) | 3 Phase, 50/60 Hz, 200/208/230/380/415 V |
| 50 Hz 420 l/m (15 cfm) | **Noise Level at 1 meter** |
| **Ultimate Total Pressure** | 60 dBA |
| < $10^{-2}$ Torr (mbar) | **Operating Range** |
| **Inlet Connection** | 40°F to 105°F (5°C to 40°C) |
| NW40 | **Weight** |
| **Outlet Connection** | 90 lb (40.0 kg) w/3 phase motor |
| NW25 | 100 lb (45.0 kg) w/1 phase motor |

**Ordering Information**

| Description | Part Number | S Wei |
|---|---|---|
| Model 600DS with base, hour meter, and direct drive motor / (1 phase universal) | 600DS-1UNIV | 1 |
| Model 600DS with base, hour meter, and direct drive motor (3 phase universal) | 600DS-3UNIV | |
| Minor Maintenance Kit | 600DS-KMI | |
| Factory Rebuild Service | 600DS-KMA | |



## Pumping speed of Edwards ESDP30A (C4F10)

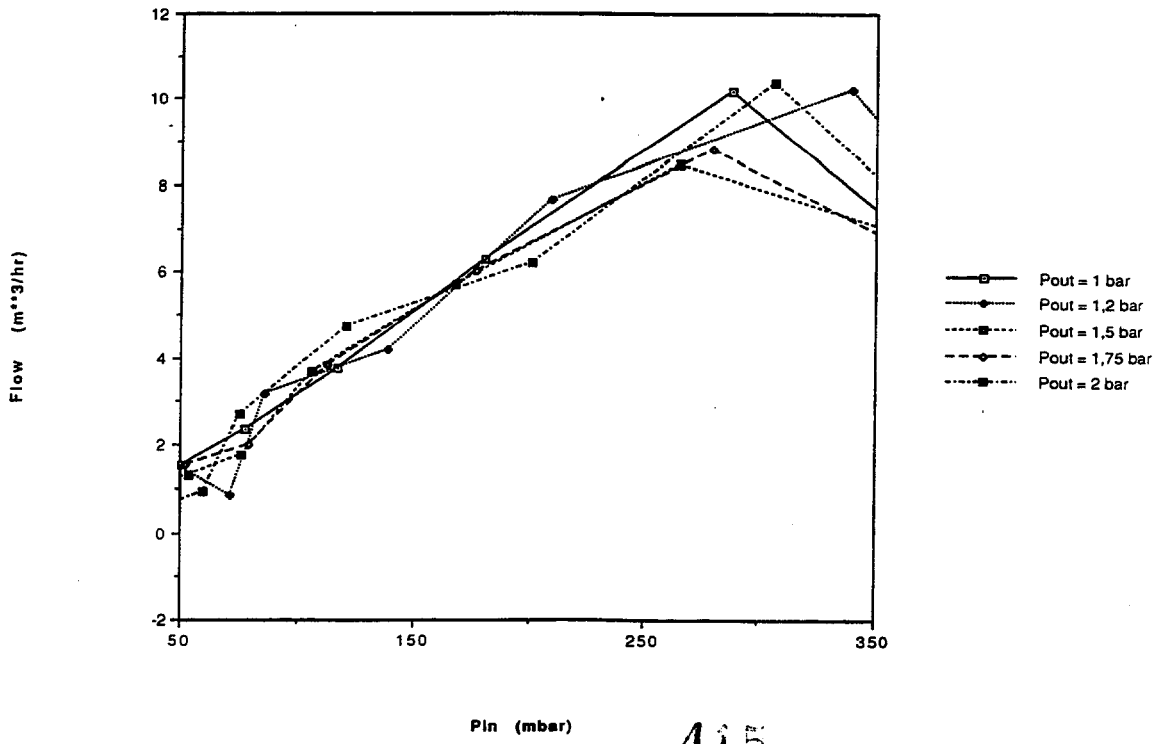

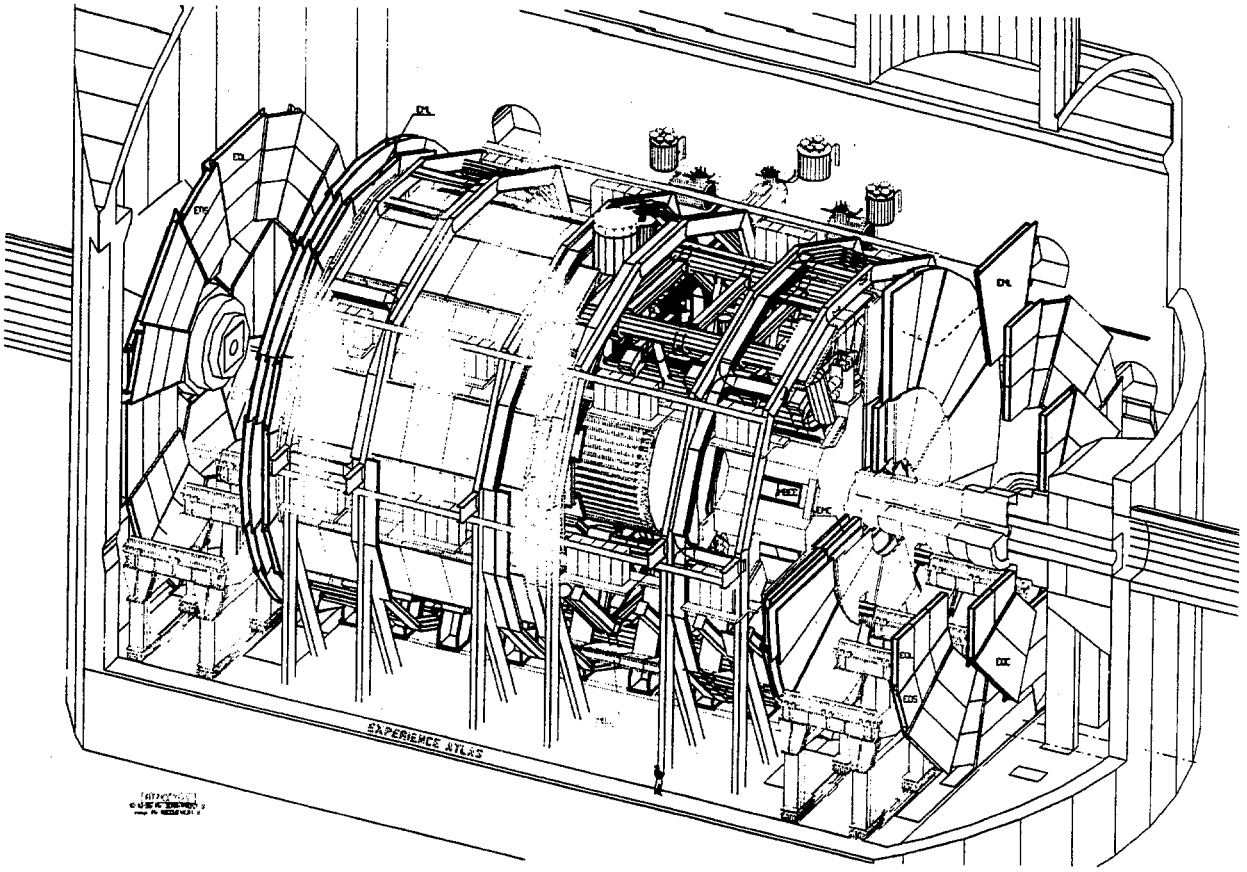
EXPERIENCE ATLAS

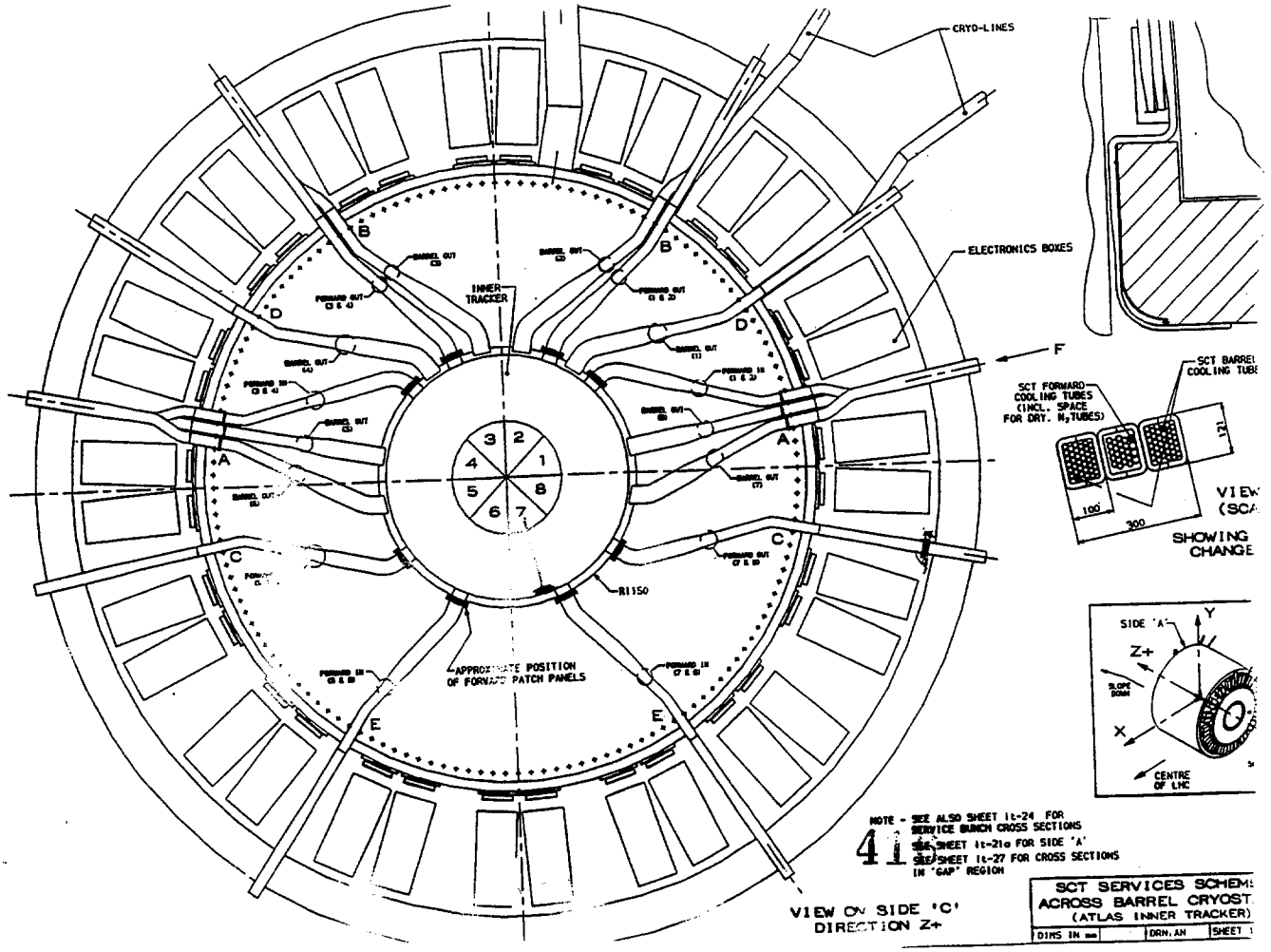
CRYO-LINES
ELECTRONICS BOXES
INNER TRACKER
F
SCT FORWARD COOLING TUBES (INCL. SPACE FOR DRY. N2 TUBES)
SCT BARREL COOLING TUBE
100
300
SHOWING CHANGE
SIDE 'A'
Y
Z+
X
CENTRE OF LHC
R1150
APPROXIMATE POSITION OF FORWARD PATCH PANELS
VIEW ON SIDE 'C'
DIRECTION Z+
NOTE - SEE ALSO SHEET It-24 FOR SERVICE BUNCH CROSS SECTIONS
SEE SHEET It-21a FOR SIDE 'A'
SEE SHEET It-27 FOR CROSS SECTIONS IN 'GAP' REGION
SCT SERVICES SCHEM
ACROSS BARREL CRYOST
(ATLAS INNER TRACKER)
DIMS IN mm
DRN. AN
SHEET

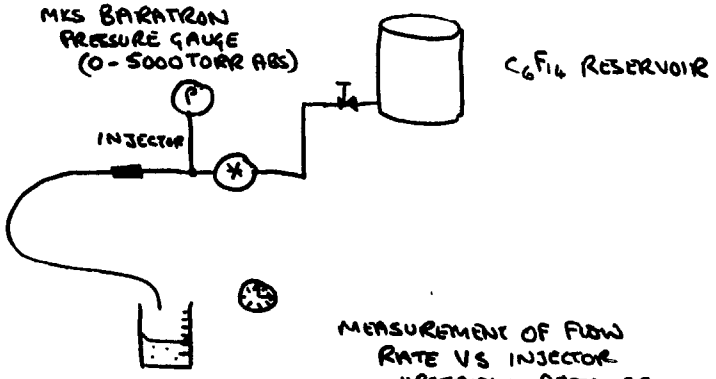


| INJECTOR TYPE | | FLOW RATE EQUATION | FLOW FOR 2 BAR ABS |
|---|---|---|---|
| "BIG" | #1 | $f = -3.2211 + 1.1197 \log P$ | 0.475 cm³/sec |
| "BIG" | #2 | $-3.2474 + 1.1212 \log P$ | 0.475 |
| "BIG" | #3 | $-3.1929 + 1.1006 \log P$ | 0.467 |
| "MID" | #1 | $-2.5555 + 0.9002 \log P$ | 0.416 |
| "MID" | #2 | $-3.0069 + 1.0415 \log P$ | 0.431 |
| "MID" | #3 | $-2.5486 + 0.8964 \log P$ | 0.410 |
| "SMALL" | #1 | $-2.0761 + 0.7321 \log P$ | 0.3406 |
| | #2 | $-2.1388 + 0.7486 \log P$ | 0.3323 |
| | #3 | $-1.9766 + 0.7053 \log P$ | 0.3450 |

OLD INJECTORS (BY WAY OF COMPARISON)

| | | | |
|---|---|---|---|
| LADDER 1 | (INCLUDES NEEDLE VALVE) | $-4.4167 + 1.5135 \log P$ | 0.8495 |
| LADDER 2 | (INCLUDES NEEDLE VALVE) | $-4.3056 + 1.4862 \log P$ | 0.6664 |
| LADDER 3 | | $-3.3644 + 1.1541 \log P$ | 0.4579 |

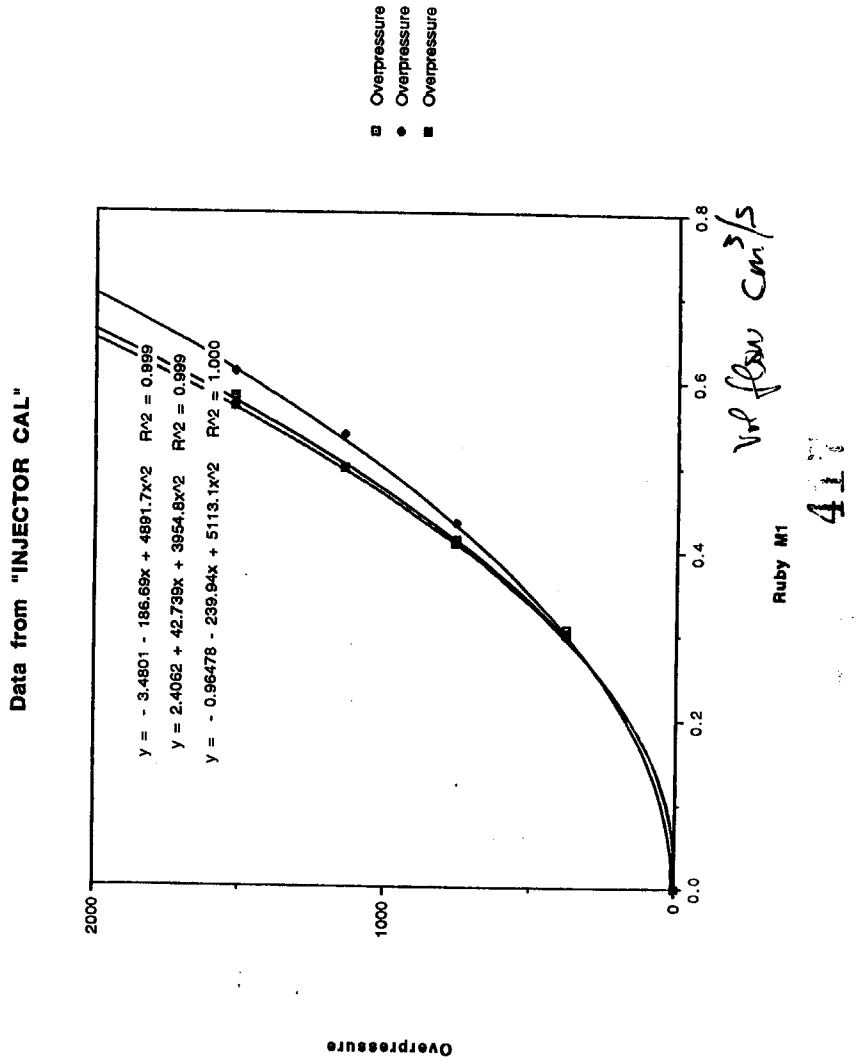

DATE
19/01/[illegible]
G123[illegible]

## Experimental Setup at the CPP Marseille

### Temperature Distribution Measurements

★ AD590 on the surface plate ▬ AD590 on the tube

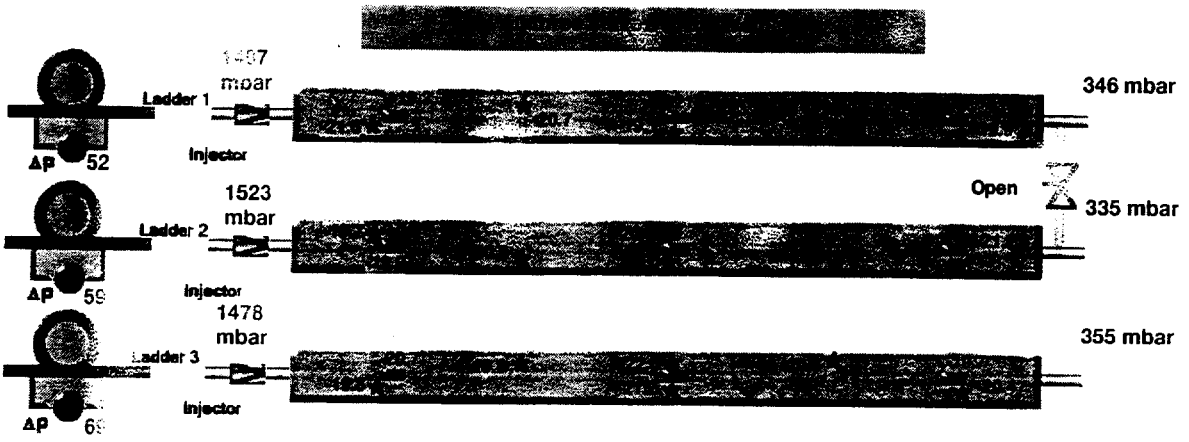


$p_{EXHM}$ = 36 torr
$p_{PUMP}$ = 1.8 $bar_{abs}$
$T_{PUMP}$ = -4.0 °C
Amb. = 0.9 °C

$p_{in}$ = 1692 mbar
( 26 mbar total flow)

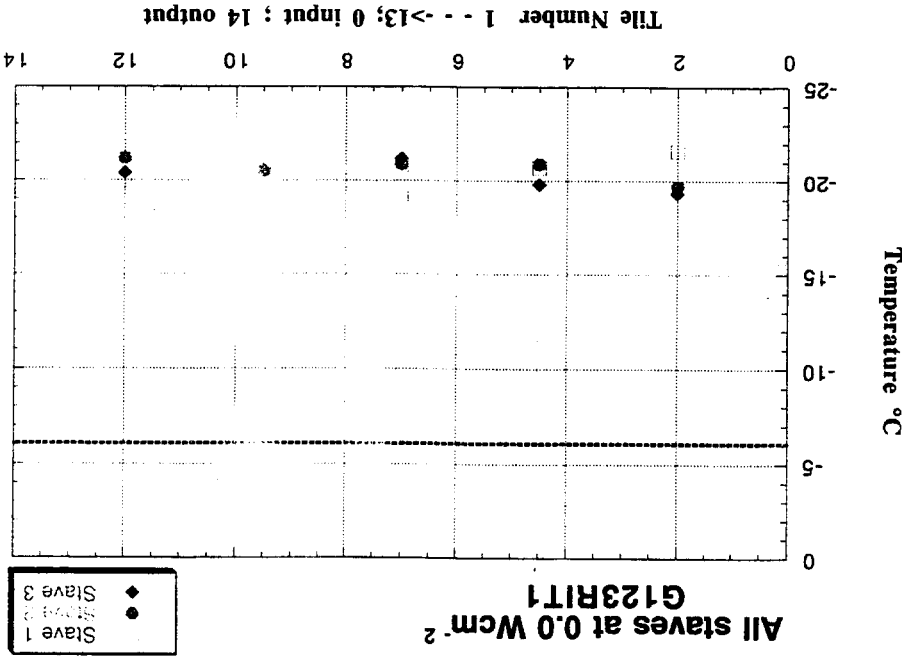

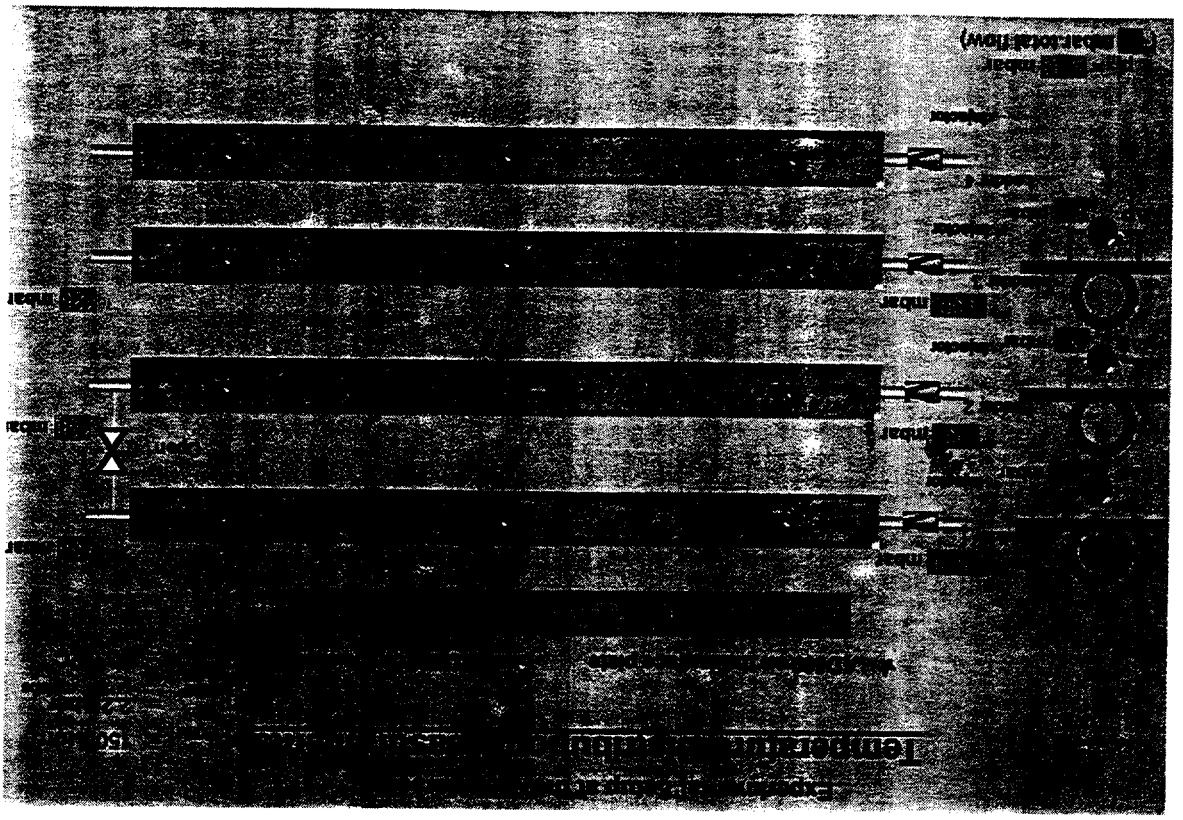

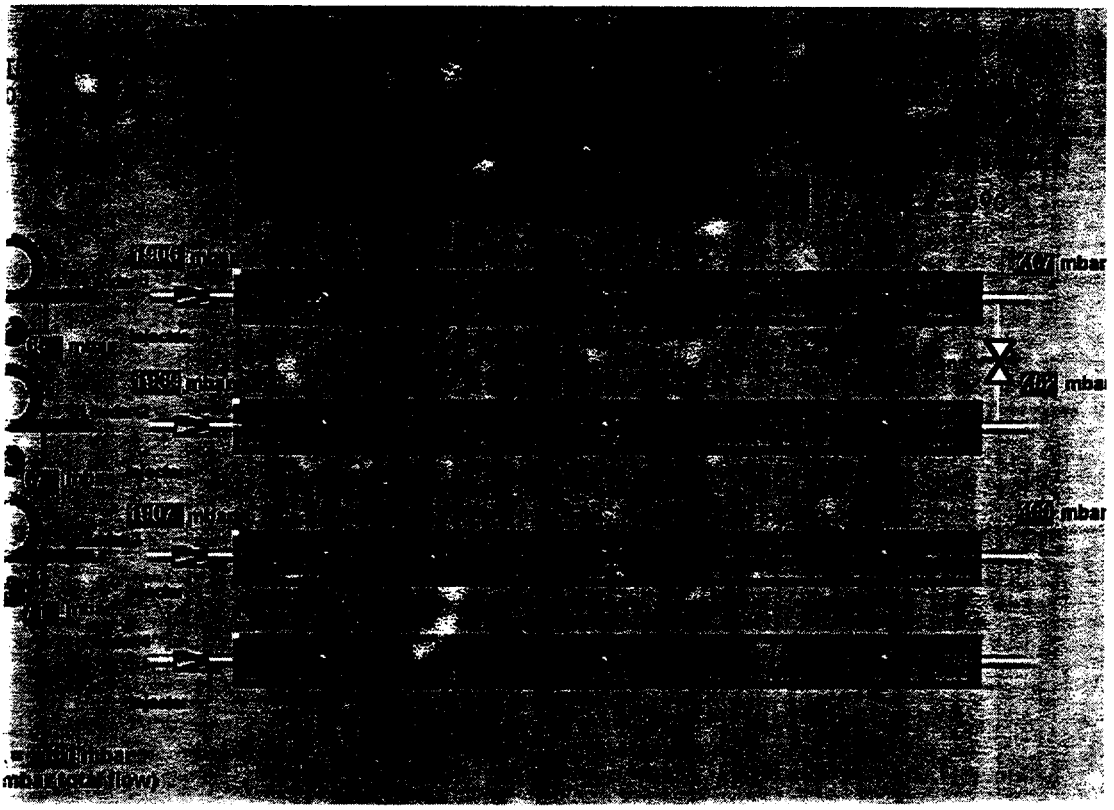

CPPM - WUPPERTAL SLIDING AL TUBE STAVE

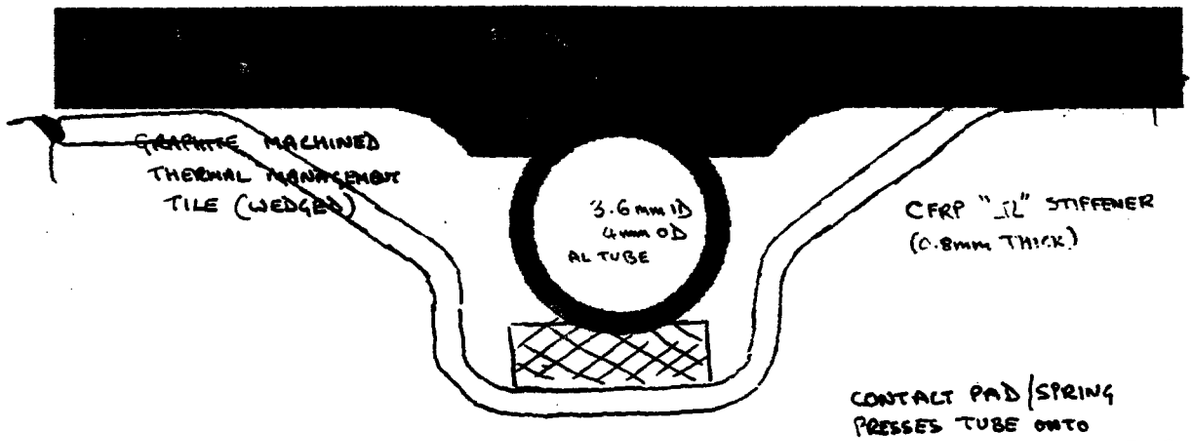


FOR T.D.R.

- FEA DISTORTION STUDIES NECESSARY
- THERMAL STUDIES
- DISTORTION MEASUREMENTS IN ESPI

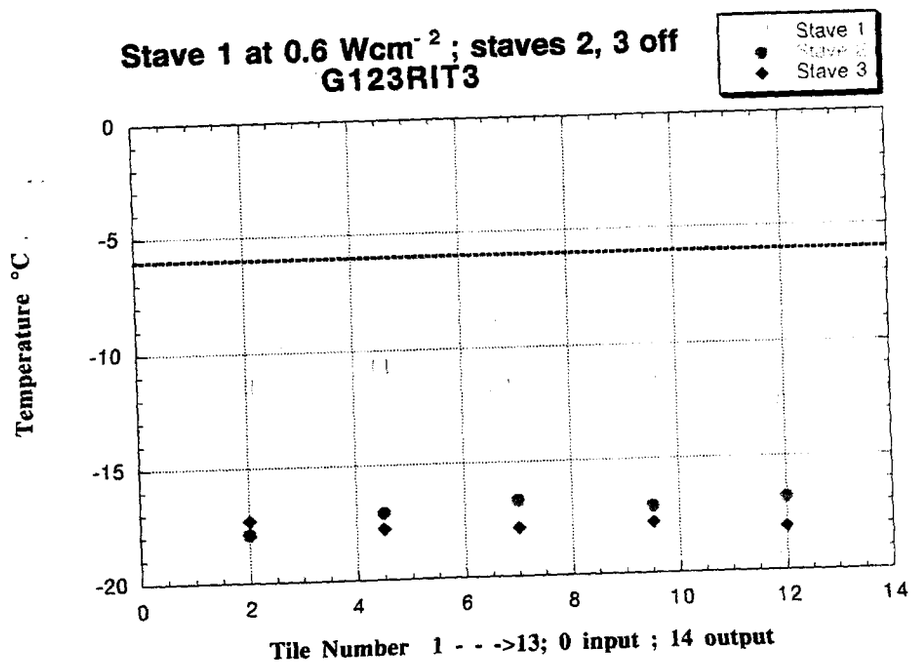

Experimental Setup at the CPP Marseille

Temperature Distribution Measurements

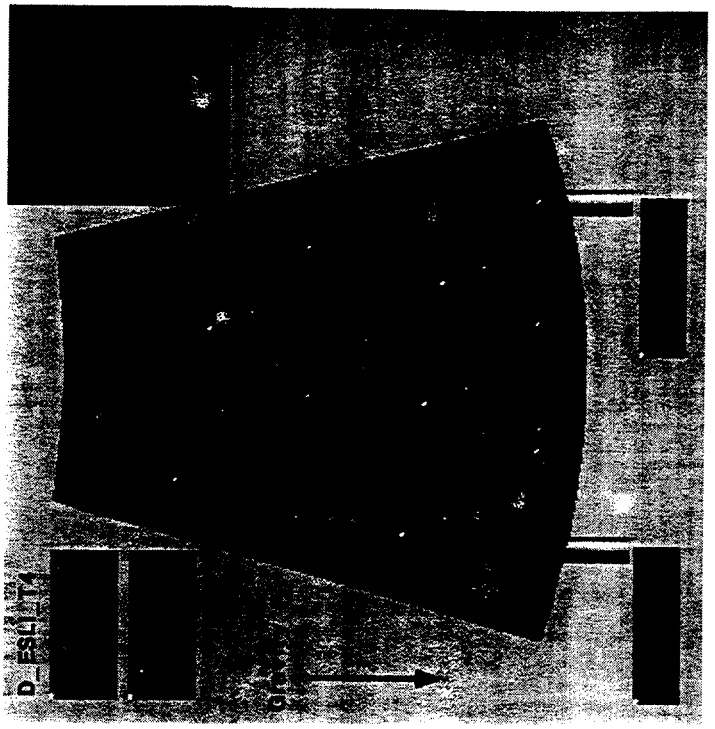


## IEW STAVE DESIGN (CPPM+WUPPERTAL) WITH SILICON TILES

emperature distribution measurements at CPPM

HANNEL NUMBER

*TILE NUMBER*

ate : 21/02/98 --> 23/02/98

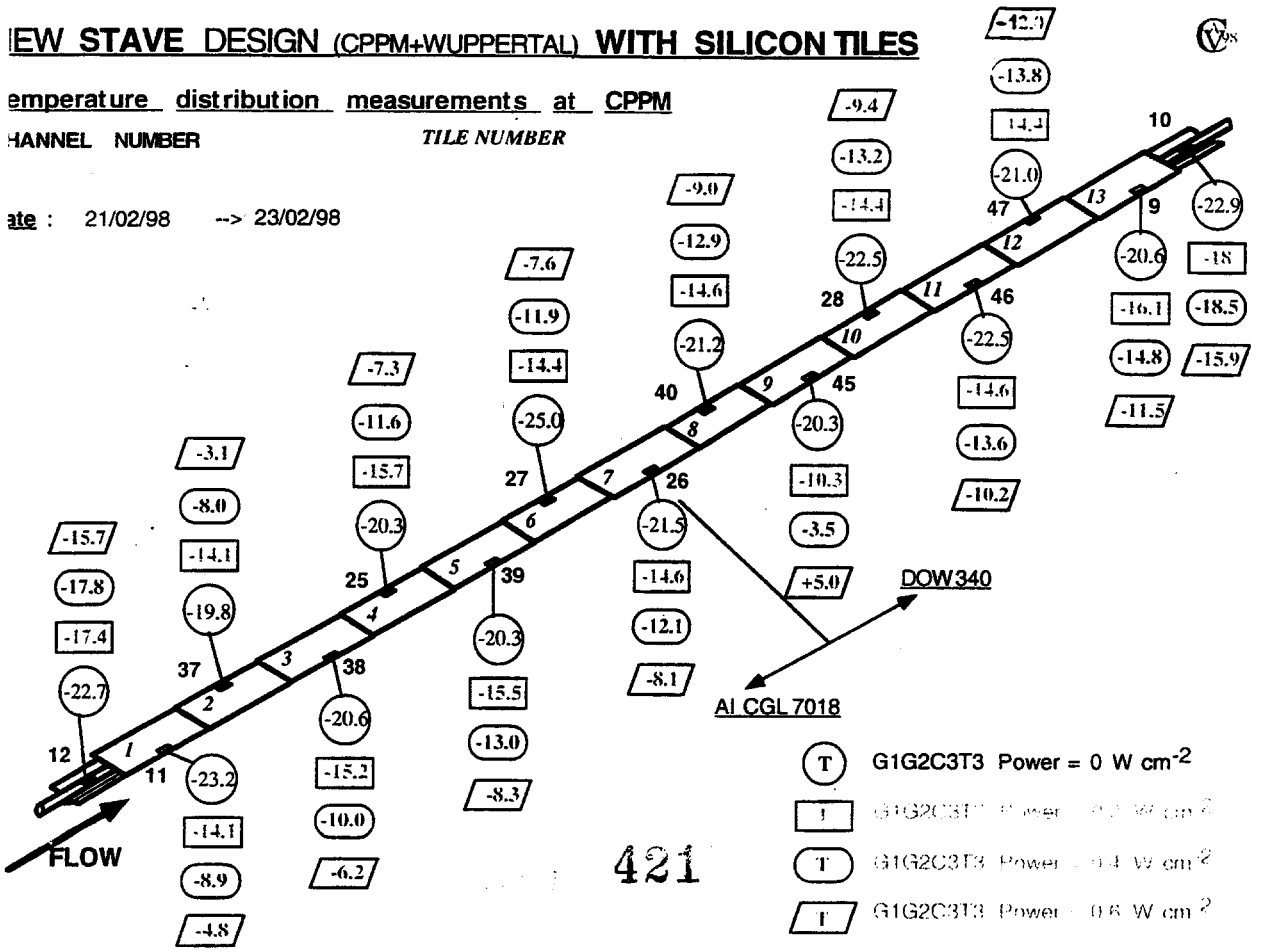

**Experimental Setup at the CPP Marseille**

Temperature Distribution Measurements

DATE : 19 / 02 / 98




**Experimental Setup at the CPP Marseille**

Temperature Distribution Measurements

DATE : 19 / 02 / 98

Experimental Setup at the CPP Marseille

## Temperature Distribution Measurements

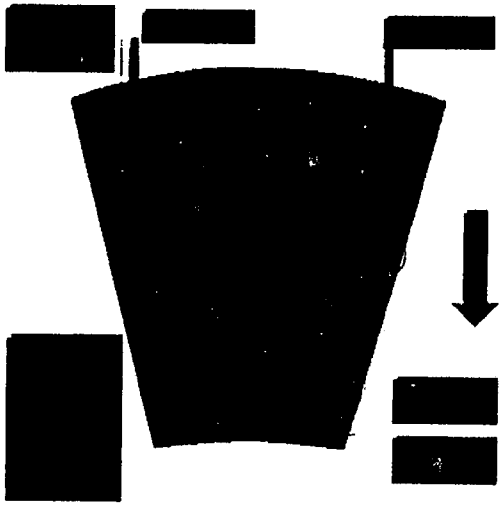



Experimental Setup at the CPP Marseille

Temperature Distribution Measurements

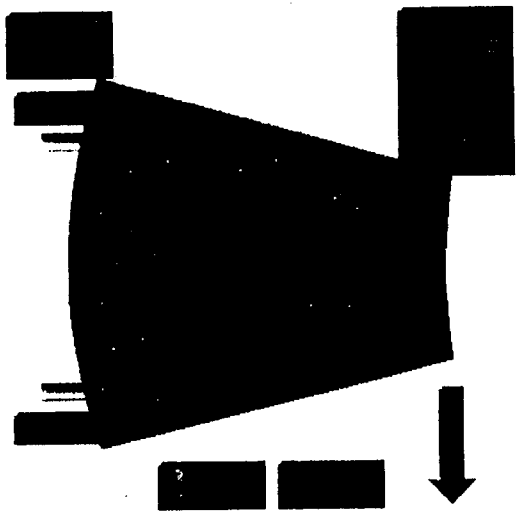

| POS. | NBRE | CODE IDENTIFICATION | MARKING DENOMINATION-CARACTERISTIQUES | | | |
|---|---|---|---|---|---|---|
| ATLAS | | | DESSINE | T.CARRIER | 12-2-97 | ECHELLE |
| | | | MOD 1 | | | |
| | | | MOD 2 | | | |
| APPARATUS OVAL TUBE COOLING EFFIENCY MEASUREMENTS | | | | | | |
| | | | | | | 152588P4 |

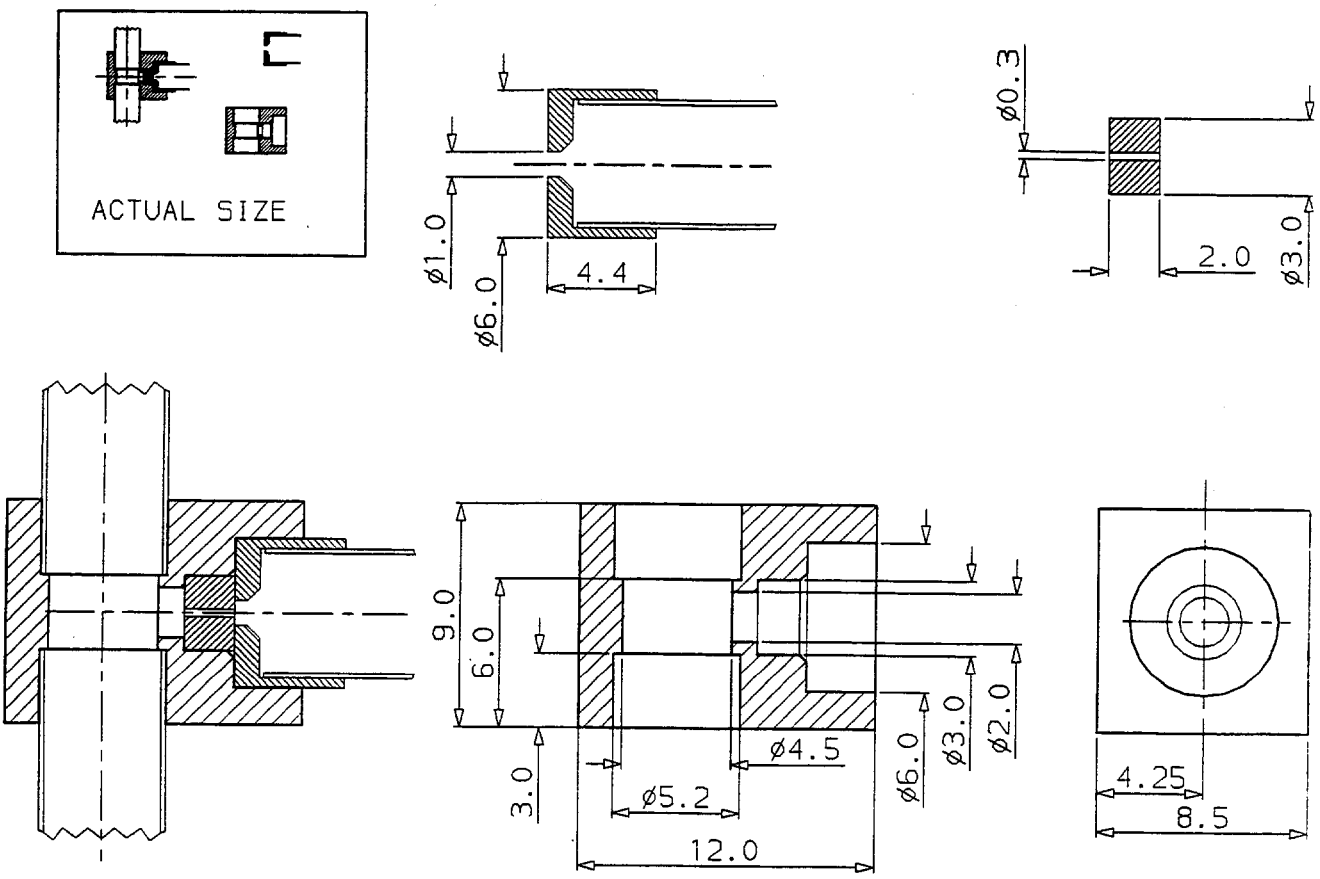


SCALE 5:1

CTUAL SIZE

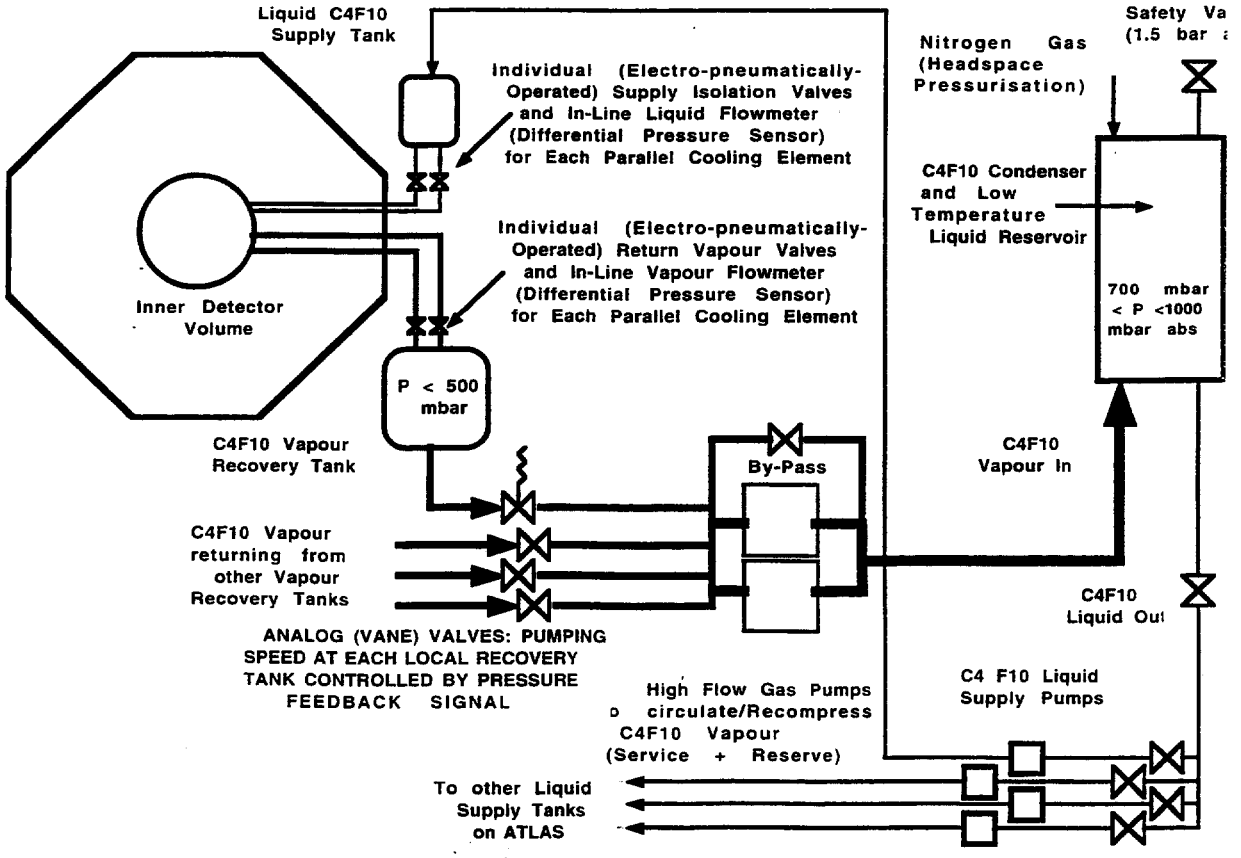

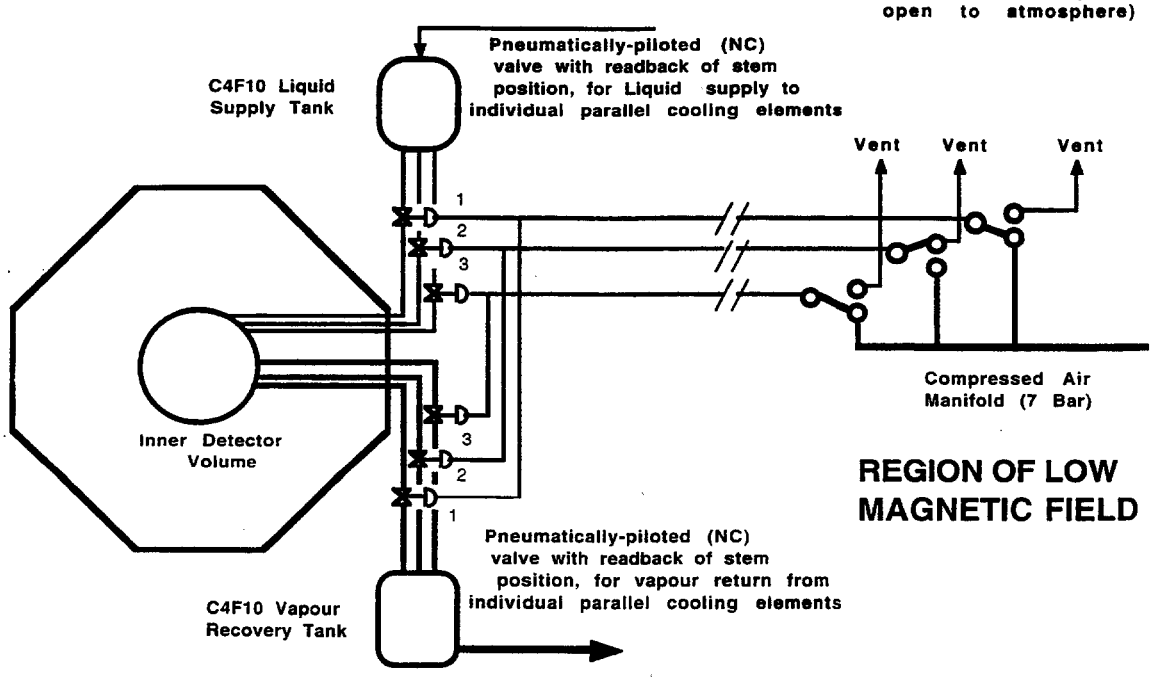
REGION OF HIGH MAGNETIC FIELD
Individual Miniature solenoid valves mount
compressed air manifold control coolant
through each parallel cooling element.
Valves represented as 3 way selectors for c
Flow to cooling elements 1 and 3 is enat
while element 2 is closed (actuator cyli
open to atmosphere)
Pneumatically-piloted (NC) valve with readback of stem position, for Liquid supply to individual parallel cooling elements
C4F10 Liquid Supply Tank
Vent
Vent
Vent
1
2
3
Compressed Air Manifold (7 Bar)
Inner Detector Volume
REGION OF LOW MAGNETIC FIELD
3
2
1
Pneumatically-piloted (NC) valve with readback of stem position, for vapour return from individual parallel cooling elements
C4F10 Vapour Recovery Tank

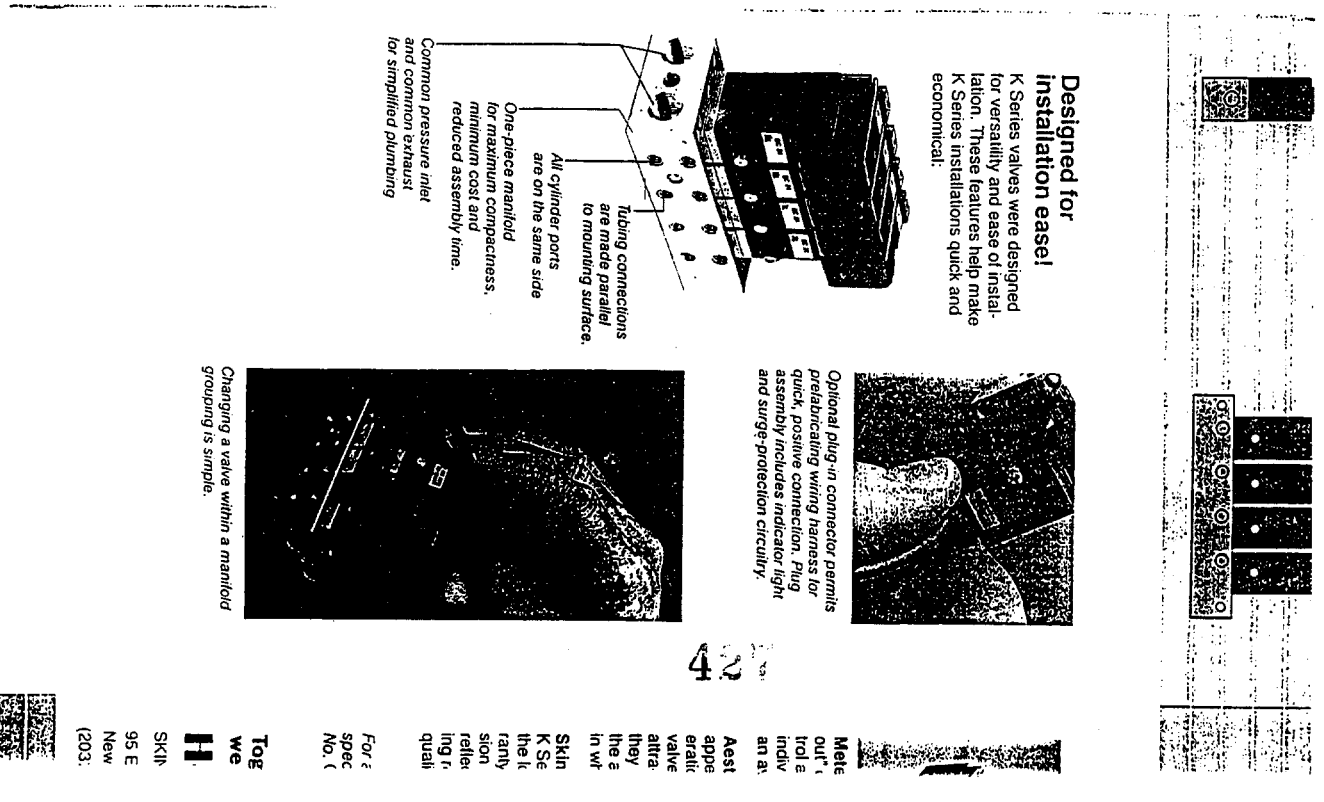
Designed for installation ease!
K Series valves were designed for versatility and ease of installation. These features help make K Series installations quick and economical:
Common pressure inlet and common exhaust for simplified plumbing
One-piece manifold for maximum compactness, minimum cost and reduced assembly time.
All cylinder ports are on the same side
Tubing connections are made parallel to mounting surface.
Optional plug-in connector permits prelabricating wiring harness for quick, positive connection. Plug assembly includes indicator light and surge-protection circuitry.
Changing a valve within a manifold grouping is simple.

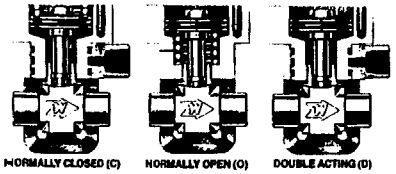

NORMALLY CLOSED (C) NORMALLY OPEN (O) DOUBLE ACTING (D)

- Valve and actuator are joined in a single compact unit
- Standard actuator material is aluminum; valve material same as Toggle Valve
- Operates on standard shop air or fluids compatible with the actuator materials
- Gageable SWAGELOK® Tube Fitting, male and female NPT end connections
- Positive stem retraction prevents accidental cycling due to vibration or shock
- O-Ring stem seal standard — no packing adjustment required
- Moveable turret allows easy installation into any system
- 100% factory tested

## TECHNICAL DATA

Valve/actuator assemblies are standard with Viton A O-Rings, TFE stem tip, and silicone base lubricant.

To order pneumatically actuated toggle valves with optional O-Ring materials, refer to the OPTIONS/ACCESSORIES, O-RING SEALS, FACTORY-ASSEMBLED IN VALVE section on page 2.

| ORIFICE | | | VALVE PRESSURE RATING@ MAXIMUM TEMPERATURE | | | |
|---|---|---|---|---|---|---|
| | | | Normally Open & Double Acting | Normally Closed | High Pressure Normally Closed | |
| In. | mm | $C_V$ | | | | Temperature Rating |
| 0.080 | 2.0 | 0.11 | 450 PSIG (3100 kPa) | 300 PSIG (2000 kPa) | 450 PSIG (3100 kPa) | -20°F to 200°F (-29°C to 93°C) |
| 0.125 | 3.2 | 0.20 | | | | |

| | MATERIAL | SPECIFICATION |
|---|---|---|
| Cap | Aluminum | ASTM B211 |
| Cylinder | Aluminum | ASTM B211 |
| Piston | Aluminum | ASTM B211 |
| Turret | Aluminum | ASTM B211 |
| O-Ring | Fluorocarbon FPM | Dupont Viton A |
| Mounting Bracket | 18-8SS | Commercial |
| N.O. Spring | 302SS | ASTM A313 |
| N.C. Spring | 17-7PH SS | ASTM A313 |

Lubrication: Silicone base lubricant

For valve materials, see Page 2.

## MINIMUM ACTUATING PRESSURES

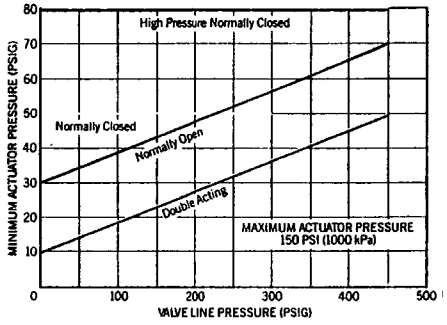


## TABLE OF DIMENSIONS

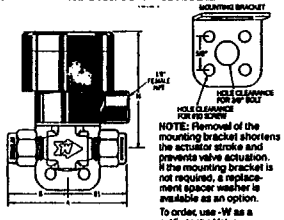


| BASIC ORDERING NUMBER | ORIFICE | | CONNECTION SIZE | | DIMENSIONS | | | | | |
|---|---|---|---|---|---|---|---|---|---|---|
| | In. | mm | INLET | OUTLET | A | B | B1 | H 92-C | H 92-O | H 92-D |
| -92M2* | 0.080 | 2.0 | 1/8 Male NPT | 1/8 Male NPT | 1.50 | .75 | .75 | 2.22 | 2.22 | 2.22 |
| -92M2-S2 | | | 1/8 Male NPT | 1/8 SWAGELOK | 1.72 | | .97 | | | |
| -92S2 | | | 1/8 SWAGELOK | 1/8 SWAGELOK | 1.94 | .97 | | | | |
| -92F2 | 0.125 | 3.2 | 1/8 Female NPT | 1/8 Female NPT | 1.62 | .81 | .81 | 2.16 | 2.16 | 2.16 |
| -92M4 | | | 1/4 Male NPT | 1/4 Male NPT | 2.00 | 1.00 | 1.00 | | | |
| -92M4-S4 | | | 1/4 Male NPT | 1/4 SWAGELOK | 2.13 | | 1.13 | | | |
| -92S6MM | | | 6mm SWAGELOK | 6mm SWAGELOK | 2.26 | 1.13 | 1.13 | | | |
| -92S4 | | | 1/4 SWAGELOK | 1/4 SWAGELOK | 2.26 | 1.13 | 1.13 | | | |
| -92S8MM | | | 8mm SWAGELOK | 8mm SWAGELOK | 2.20 | 1.10 | 1.10 | | | |

*Orifice at the seat is 0.125" (3.2mm). 0.080" (2.0mm) port orifice sets the maximum flow.

Dimensions shown with SWAGELOK nuts finger-tight, where applicable. All dimensions are in inches — for reference only, subject to change.

## ORDERING INFORMATION

**Materials/Actuator Type:** To specify *valve* material, use SS for stainless steel or B for brass as a prefix to the Basic Ordering number. To specify *actuator* type, use the designator of the desired actuator, below, as a suffix to the Valve Ordering Number.

Example: SS-92M4-S4-D

-C Normally Closed
-O Normally Open
-D Double Acting
-HPC High Pressure Normally Closed

**Patterns:** To order angle pattern valves, insert -A before the actuator designator in the Ordering Number. Example: SS-92M2-A-O. Some of the above valves are available in a cross pattern. Cross pattern valves offer uninterrupted flow between side ports at all times; on-off flow through bottom port. Contact your Authorized Sales & Service Representative for more information.

CREDITS SWAGELOK — TM Crawford Fitting Company
Viton Karez — TM DuPont/17-7PH — TM Armco Steel

### Special Applications

WHITEY Pneumatically Actuated Toggle Valves are available for use in low temperature, high temperature, and fluorocarbon-free applications (see SPECIAL APPLICATION OPTIONS section on Page 3). To order, use the designator of the desired application, below, as a suffix to the Valve Ordering Number. Example: SS-92F2-C-LT

| APPLICATION | DESIGNATOR |
|---|---|
| High Temperature | -HT |
| Low Temperature | -LT |
| Fluorocarbon Free | -NF |

Your Local Authorized Sales & Service Representative:

the SWAGELOK companies

Printed in U.S.A.
SWG-1164-C
09-92-5P
MS-01-54

3 of 14

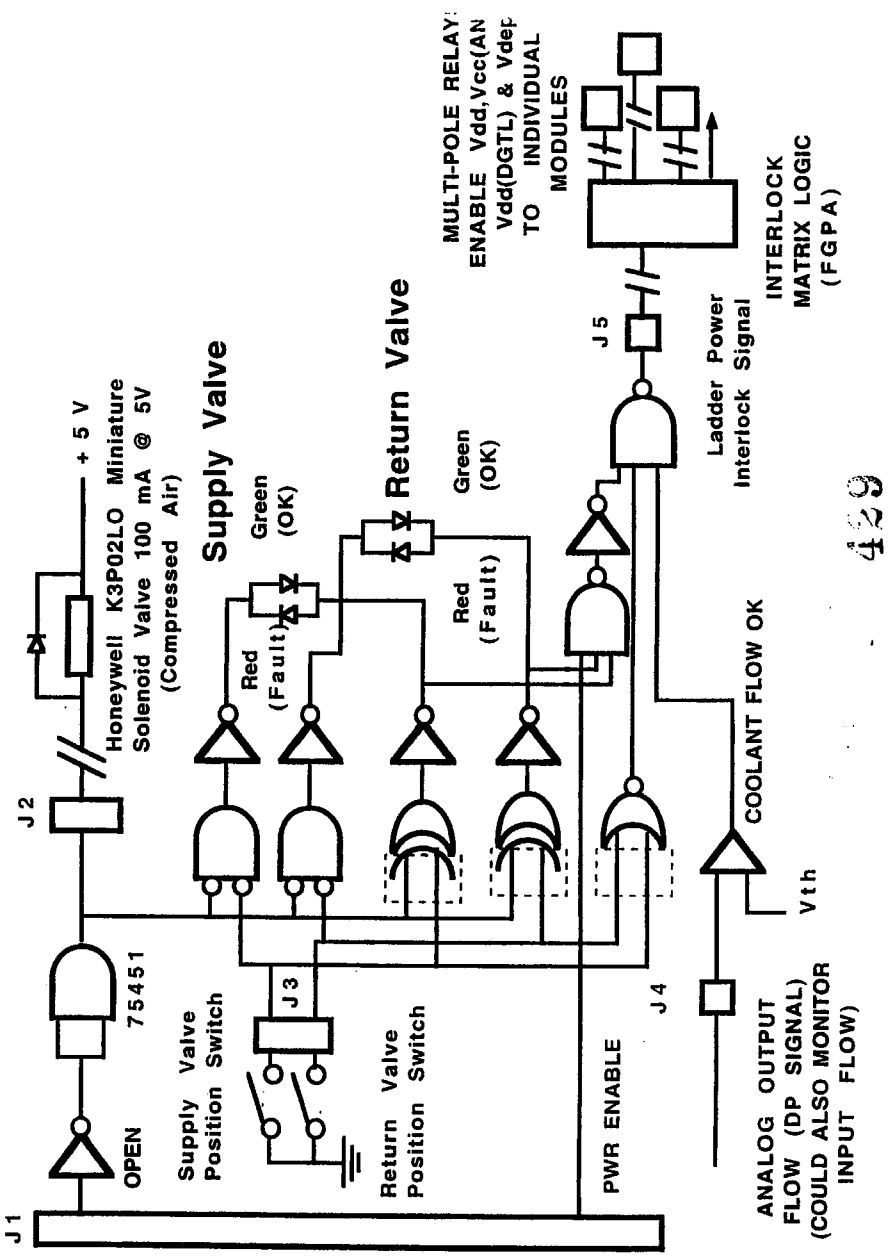


429